



**Queen Mary**  
**University of London**

**Fabrication and Characterization of  
Electrospun Alumina Nanofibre Reinforced  
Polycarbonate Composites**

A thesis submitted to Queen Mary, University of London

for the degree of Doctor of Philosophy

August 2017

By

**Wenjun Sun**

School of Engineering and Materials Science

Queen Mary University of London

Mile End Road, London, E1 4NS

# **Declaration**

I declare that the work performed is entirely by myself during the course of my PhD studies at the Queen Mary, University of London and has not been submitted for a degree at this or any other University.

Wenjun Sun

# Abstract

Fibres with ultra-high tensile strength have attracted unprecedented attention due to the rapidly increasing demand for strong fibre reinforced composites in various fields. However, despite a theoretical strength as high as around 46 GPa, current commercial alumina fibres only reach strength value of around 3.3 GPa because of the defects between the grains. Electrospinning provides a method to produce ceramic nanofibres with diameters reduced to nano-scale with effectively enhanced strength. Different calcination procedures were applied to study the morphology and crystal structure growth of alumina. Tested with a custom-built AFM-SEM system, the tensile strength of single crystal  $\alpha$ -alumina nanofibres were found to have little dependence on diameter variations, with an average value of  $11.4 \pm 1.1$  GPa. While the strength of polycrystalline  $\gamma$ -alumina nanofibres were controlled by defects, showing a diameter dependent mechanism. Apart from the intrinsic properties of the fibre and matrix, the interface between them also plays an important role in determining composite mechanical properties. Collected by a rotating drum during electrospinning, aligned fibres were used to reinforce polycarbonate matrix for fabricating composite. The composite mechanical properties were successfully improved after surface modification with silane coupling agent. With a fibre volume fraction of around 7.5%, the composite strength doubled and the Young's modulus increased by a factor of 4 when compared with the pure polycarbonate. Apart from surface modification, the fibre/matrix interface can also be affected by transcrystallinity.

Transcrystalline layers were formed in the alumina reinforced polycarbonate composites after annealing. Significant enhancement of the Young's modulus of the crystallized polycarbonate by a factor of 3 compared to the amorphous phase was measured directly using AFM based nanoindentation. Optimization of the Young's modulus is suggested as a balance between extending the annealing time to grow the transcrystalline layer and reducing the processing time to suppress void development in the PC matrix.

# Acknowledgement

Special thanks to my supervisor Prof. Asa H. Barber for all his guidance, encouragement and support, especially after his leaving for Portsmouth. I truly learned a lot from him through all these four years. I would always be inspired by the way that he always tries to keep a clear goal, how he uses basic examples to help people to understand complex problems, and how he always communicates actively during conferences in my future work. I truly feel lucky to have such a great supervisor. I would also like to thank Dr. Haixue Yan for all the discussions and support for my study. I couldn't be in London for study without his help, and thanks to him also for take care of me as my second supervisor after Asa left. Thanks to Dr. Nadja Tarakina for all the help with TEM work as well as treating me as a close friend despite of the different culture background. Thanks to Mr. Russell Bailey for being so kind and patient to all my disturbing with all the experiment problems.

Thanks a lot to all the group members, I would always remember how you treat me kindly when I first arrive at London. Thanks to Dr. Fengfeng Zhang, for all the happiness we share together and all the supporting during hard times as well. Thanks to Dr. Urszula Stachewicz and Dr. Yiran An for helping with all the experiment. Thanks to Neelam Siyab, Dr. Congwei Wang, Dr. Alexander Kao, Dr. Filipe Almeida and Hao Zhang. Though we didn't have spent that much time together, but the time that we shared would always be remembered and cherished. I wish you all a successful future.

Many thanks to all my friends that I met during study and living in London, including: Xingchen Zhang, Fan Wang, Yejiao Shi, Dr Chuying Yu, Dr Yang Zeng, Dexu Kong, Fan Wu, Jingyuan Zhu, Servann Hérou, Pei Tang, Da Huang, Xi Zhang, Dr Dong Luo, et al. Without you to share the interesting life stories and all the happiness, life would be much more plain and boring. Special thanks to my landlord auntie Shirley, for all the moments we shared together and all the stories during the last days in London.

Thanks very much for Queen Mary, University of London and Chinese Scholarship Council for providing the funding for supporting my study and life expenses in UK. I appreciate this opportunity very much and truly learned a lot during four years staying here.

Special acknowledgement to my family and my husband Yuhao, to whom this work is dedicated. I cannot achieve anything without all your support and love.

## Publications and presentations

1. **Wenjun Sun**, Nadezda V. Tarakina, Haixue Yan, Asa H. Barber. *Growth mechanism controlled ultra-high strength electrospun alumina nanofibers*. (In preparation)
2. **Wenjun Sun**, Asa H. Barber. *The effect of transcrystallization on mechanical properties of polycarbonate composite reinforced with electrospun alumina nanofibers*. (In preparation)
3. **Wenjun Sun**, Nadezda V. Tarakina, Haixue Yan, Asa H. Barber. *Fabrication and characterization of alumina nanofibers with ultra-high strength*. 40th International Conference and Expo on Advanced Ceramics and Composites, Florida, USA. (Oral presentation)
4. **Wenjun Sun**, Asa H. Barber. *Transcrystallization of polycarbonate induced by electrospun alumina nanofibers*. 5th International Conference on Multifunctional, Hybrid and Nanomaterials, Lisbon, Portugal. (Poster presentation)

# Table of Contents

Declaration .....	II
Abstract .....	III
Acknowledgement.....	I
Publications and presentations .....	I
Table of Contents .....	I
List of Tables.....	I
List of Figures .....	II
List of symbols.....	X
1 Introduction.....	1
1.1 Background .....	1
1.2 Project aims .....	5
2 Literature review.....	7
2.1 Introduction to fibre-reinforced composite .....	7
2.1.1 Theory of fibre-reinforced composites.....	7
2.1.2 Components of composites .....	13
2.1.3 Ceramic nanofibres .....	16
2.1.4 Polycarbonate .....	18
2.2 Fundamentals of alumina .....	19
2.2.1 Fabrication of alumina nanofibres with electrospinning.....	20
2.2.2 Crystal structures of alumina .....	22
2.2.3 Growth mechanism and mechanical properties of $\alpha$ -alumina whiskers ...	29
2.2.4 Application of alumina fibres in composite.....	30
2.3 Electrospinning.....	31
2.3.1 Electrospinning setup and procedures.....	31



2.3.2	Parameters affecting electrospinning .....	32
2.3.3	Aligned nanofibres fabricated with electrospinning .....	35
2.4	Measurement of the mechanical properties of individual nanofibres .....	38
2.4.1	Nano tensile testing .....	38
2.4.2	Three-point bending test .....	40
2.4.3	Nanoindentation .....	42
2.4.4	Oscillation methods.....	43
2.5	Interface improvement between ceramic and polymers.....	44
2.5.1	Coupling agents.....	45
2.5.2	Plasma treatment .....	50
2.6	Transcrystallization in fibre reinforced thermoplastic composites .....	51
2.6.1	Growth mechanism of transcrystallinity .....	52
2.6.2	Effects of transcrystallization on composite properties .....	53
2.6.3	Crystallization of polycarbonate .....	55
2.7	Summary .....	58
3	Methodology.....	60
3.1	Fabrication of alumina nanofibres and polycarbonate composites reinforced with alumina nanofibres .....	60
3.1.1	Materials.....	60
3.1.2	Fabrication of alumina nanofibres .....	61
3.1.3	Fabrication of polycarbonate composite reinforced with alumina nanofibres with solution casting method .....	62
3.2	Imaging methods .....	64
3.2.1	Scanning electron microscopy imaging .....	64
3.2.2	Transmission electron microscopy imaging .....	66
3.2.3	Atomic force microscopy imaging.....	68
3.3	Structural analysis .....	70
3.3.1	Differential scanning calorimetry .....	70
3.3.2	Fourier transform infrared spectroscopy.....	71
3.3.3	X-ray and electron diffraction.....	73
3.4	Mechanical testing.....	78
3.4.1	Combined AFM-SEM system for nanotensile testing of individual alumina nanofibres.....	78
3.4.2	AFM Nanoindentation .....	81
3.4.3	Micro-tensile testing.....	83

3.5	Other methods .....	84
3.5.1	Specific surface area .....	84
3.5.2	Porosity .....	85
3.6	Summary .....	87
4	Alumina nanofibre fabrication and fibre growth mechanism.....	88
4.1	Introduction .....	88
4.2	Materials and methods.....	89
4.2.1	Sample preparation.....	89
4.2.2	Characterization of morphology of alumina nanofibres .....	90
4.3	Results and Discussion .....	91
4.3.1	Effect of concentrations of PAN and AP on fibre morphologies.....	91
4.3.2	Effect of heating procedure .....	95
4.3.3	Fibre diameter change during calcination .....	99
4.3.4	Crystal structures of $\alpha$ -alumina nanofibres changing with calcination time 101	
4.4	Conclusions .....	105
5	Tensile testing of individual nanofibres.....	107
5.1	Introduction .....	107
5.2	Methods .....	109
5.2.1	Electrospun sparsely distributed nanofibres.....	109
5.2.2	Tensile testing of individual nanofibres .....	110
5.2.3	Transmission electron microscopy and electron diffraction .....	115
5.3	Results and discussion.....	115
5.4	Conclusions .....	118
6	Fabrication and characterization of polycarbonate composite reinforced with alumina nanofibres.....	120
6.1	Introduction .....	120
6.2	Materials and Methods .....	123
6.2.1	Materials.....	123
6.2.2	Fabrication of uniaxially aligned nanofibres with electrospinning.....	123
6.2.3	Surface modification .....	124
6.2.4	Composite fabrication with solution impregnation.....	125
6.2.5	Characterization of surface modified alumina nanofibres and polycarbonate composites reinforced with alumina nanofibres .....	126
6.3	Results and discussion.....	127

6.3.1	Electrospinning of aligned alumina nanofibres.....	127
6.3.2	Surface modification of alumina nanofibres .....	128
6.3.3	Mechanical properties improvement of composite reinforced with surface modified alumina nanofibres .....	130
6.3.4	Theoretical Young's modulus calculation .....	133
6.4	Conclusions .....	138
7	Transcrystallization of polycarbonate induced by alumina nanofibres .....	140
7.1	Introduction .....	140
7.2	Materials and methods.....	143
7.2.1	AF/PC composite fabrication.....	143
7.2.2	Thermal characterization.....	144
7.2.3	Imaging methods .....	144
7.2.4	Mechanical testing .....	145
7.3	Results and discussion.....	147
7.3.1	Thermal behaviour of polycarbonate reinforced with alumina nanofibres after annealing.....	147
7.3.2	Morphology of crystallized polycarbonate .....	150
7.3.3	Mechanical properties .....	153
7.4	Conclusions .....	156
8	Conclusions and future work .....	158
8.1	Conclusions .....	158
8.2	Future work .....	160
	Reference.....	163

## List of Tables

Table 2.1. Materials used to produce alumina nanofibres by electrospinning.....	21
Table 2.2. Several common polymorphs of alumina. ....	23
Table 2.3. Summary of some coupling agents used in polymer/ceramic system .....	49
Table 5.1. Diameter and tensile strength of strong ceramic fibres used both in industry and in this work.....	118
Table 6.1. Parameters for calculation of theoretical composite Young's modulus. ....	137

# List of Figures

Figure 1.1. Schematic illustration of composite reinforced with (a) continuous fibres, (b) short fibres, (c) particles and (d) laminate. ....	2
Figure 2.1. Schematic illustration of (a) composite containing aligned, continuous fibres, and (b) the composite simplified as a model of two parallel slabs under load along fibre direction.....	8
Figure 2.2. Schematic illustration of composite containing aligned, continuous fibres simplified as a model of two parallel slabs under load along transverse fibre direction. .	9
Figure 2.3. Longitudinal tensile loading of a unidirectional discontinuous fibre lamina. ....	10
Figure 2.4. Idealized (a) longitudinal stress and (b) shear stress on an individual fibre under load.....	12
Figure 2.5. Schematic illustration of critical fibre length on the longitudinal stresses of a discontinuous fibre.....	13
Figure 2.6. Common materials used as matrices.....	14
Figure 2.7. Diameter dependence of effective Young's modulus in [0001] oriented ZnO nanowires from bending: (red dot) experimental results, (solid line) fitted results by the core-shell composite NW model , (dashed line) modulus for bulk ZnO (E3). ....	17
Figure 2.8. Schematic illustration of synthesis of bisphenol-A polycarbonate.....	18

Figure 2.9. Schematic illustration of alumina crystal structure transformation sequences from different start materials.....	23
Figure 2.10. Conventional unit cell of $\gamma$ -alumina .....	24
Figure 2.11. Conventional unit cell crystal structure of $\delta$ -alumina with both tetragonal and orthorhombic crystal systems.....	25
Figure 2.12. Conventional unit cell of $\theta$ -alumina .....	25
Figure 2.13. Schematic illustration of crystal structure of $\alpha$ -alumina.....	26
Figure 2.14. Unit cells of (a) uncalcined AlO(OH) (orthorhombic) and calcined Al <sub>2</sub> O <sub>3</sub> : (b) $\gamma$ -Al <sub>2</sub> O <sub>3</sub> (cubic), (c) $\delta$ -Al <sub>2</sub> O <sub>3</sub> (orthorhombic) and (d) $\theta$ -Al <sub>2</sub> O <sub>3</sub> (monoclinic). .....	28
Figure 2.15. Schematic illustration of typical electrospinning setup. ....	31
Figure 2.16. Schematic illustration of rotating drum for collecting aligned fibres.....	36
Figure 2.17. (A) Schematic illustration of the setup for collecting nanofibres with two strips of silicon wafers. (B) Schematic illustration of the electrostatic force working on nanofibres. (C–H) SEM images of aligned nanofibres made of (C) carbon, (D) anatase TiO <sub>2</sub> , (E) NiFe <sub>2</sub> O <sub>4</sub> , (F) TiO <sub>2</sub> /PVP, (G) Sb-doped SnO <sub>2</sub> , and (H) BaTiO <sub>3</sub> . ....	36
Figure 2.18. (a) (b) Digital camera images of prepared nanofibre meshes using epoxy and ferrite as the collectors, respectively; (c) (d) Optical micrographs of (a) and (b).....	37
Figure 2.19. Schematic showing electrospun fibres on a plastic frame used for nano tensile tester (a) before and (b) after cutting the frame.....	39
Figure 2.20. Scanning electron microscope images of individual MWCNT mounted between two opposing AFM probes. ....	40
Figure 2.21. Schematic showing of a nanofibre bending test using an AFM probe.....	41
Figure 2.22. Method of obtaining contact stiffness from the load–displacement curve. ....	43
Figure 2.23. (a) Schematic image and (b) SEM image showing nanofibres attached to two similar AFM cantilever probes. ....	44
Figure 2.24. Several commonly used silanes. ....	46

Figure 2.25. Functional mechanism of silane coupling agent on inorganic substrate. ...	46
Figure 2.26. Optical image of transcrySTALLINE interfaces of polypropylene surrounding the carbon nanotube fibres isothermally crystallized at 125 °C. <sup>[186]</sup> .....	52
Figure 2.27. Heating traces of polycarbonate crystallized at 185 °C for times ranging from 54 to 680 h (heating rate = 10 °C·min <sup>-1</sup> ). Inset shows the corresponding development of the total heat of fusion.....	56
Figure 2.28. (a) The first heating DSC (lower direction is endothermic) curves at the heating rate of 10 °C/min; (b) WAXD traces for annealed PC/VGCF <sup>TM</sup> (95:5 wt. ratio) composite at 160, 180, 200, 220 and 240 °C for 2h, respectively.....	57
Figure 3.1. Process of solution casting to fabricate polymer matrix composite. ....	63
Figure 3.2. Schematic representation of a typical scanning electron microscope setup. ....	65
Figure 3.3. Schematic of a typical TEM setup.....	67
Figure 3.4. Schematic illustration of the atomic force microscope setup. ....	68
Figure 3.5. Schematic illustration of a typical DSC setup. ....	71
Figure 3.6. Schematic illustration of a typical FTIR setup. ....	72
Figure 3.7. Schematic illustration of Bragg's law. ....	74
Figure 3.8. Schematic illustration of a typical XRD setup. ....	76
Figure 3.9. Schematic illustration of the in situ configuration of tensile testing of a nanofibrous sample with a combination of AFM–SEM. ....	79
Figure 3.10. SEM image showing a typical tensile testing procedure of electrospun nanofibres with AFM/SEM system: (a) AFM contacts one end of the fibre with glue on the probe; (b) AFM probe moves away with the fibre fixed to the probe apex; (c) AFM probe moves towards a glue drop and allow the other end of the fibre contacts the glue; (d) Curing of the glue and translation of the AFM probe/probe away from the glue drop provides tensile deformation until failure. ....	80

Figure 3.11. Schematic illustration of AFM nanoindentation. X axis is the piezoelectric actuator displacement, while y axis is the voltage output.....	82
Figure 3.12. Illustration of a conventional tensile testing setup. ....	83
Figure 3.13. Schematic illustration of gas pycnometer.....	86
Figure 4.1. Scanning electron microscopy images of electrospun PAN/AP nanofibres with different concentrations of PAN in PAN/DMF solution: (a) 6 wt%, (b) 7 wt%, (c) 8 wt%, (d) 9 wt% and (e) 10 wt%. For all these solutions, the ratio between PAN weight percentage and AP weight percentage is fixed at 3.....	92
Figure 4.2. (a) (b) (c) (d) (e) Frequency distributions of diameter of PAN/AP fibres electrospun from different concentration of PAN and AP The weight ratio of PAN and AP was fixed at 3 and the changing of PAN and AP were represented by the variation of PAN in PAN/DMF solution; (f) The dependence of PAN/AP fibre diameters on the PAN/AP weight percentage in PAN/AP/DMF solution. ....	94
Figure 4.3. (a) (b) (c) (d) Frequency distribution of diameter of PAN/AP fibres electrospun from different concentration of PAN and AP; (e) The dependence of PAN/AP fibre diameters on the weight ratio of AP and PAN. The concentration of PAN in solution before AP was added was fixed at 10%.....	95
Figure 4.4. Scanning electron microscopy image of (a) as-spun nanofibres, (b) alumina nanofibres calcinated at 1200 °C for 1 h, (c) alumina nanofibres calcinated at 1200 °C for 4 h, and (d) alumina nanofibres calcinated at 1400 °C for 2 h.....	97
Figure 4.5. (a) X-ray diffraction pattern for an alumina nanofibre mat calcinated at 1200 °C for a range of times. (b) Specific surface area of alumina nanofibre mats calcinated under 1200 °C for different time. ....	98
Figure 4.6. Change of fibre morphologies during calcination at 1200 °C with the increasing calcination time: (a) 0 h, (b) 4h and (c) 7h. (d) Fibre diameters of aluminium	



oxide nanofibres electrospun from the same solution but calcinated under different time. The black dots are experimental value, while the solid line is the fitted value..... 100

Figure 4.7. (a) TEM image showing polycrystalline  $\gamma$ -alumina nanofibres calcinated at 1200 °C for 1 h. (b) TEM and ED images of  $\delta$ -alumina crystals grown in polycrystalline  $\gamma$ -alumina nanofibres. (c) TEM image of alumina nanofibre calcinated under 1200 °C for 2.5 h and ED images taken from areas B, C, D, E, F and G respectively. The fibre consists of both polycrystalline  $\gamma$  phase and single crystal  $\alpha$  phase. The enlarged pictures of position B and the fibre inverted ‘T’ crossing point show that the fibres are formed by grain growth of  $\alpha$  grains with sizes close the fibre diameter. .... 102

Figure 4.8. TEM images showing alumina nanofibres predominantly of  $\alpha$ -alumina (position A, B, C and D) and  $\gamma$ -alumina at the end (position E). ED images taken from different positions additionally indicate single crystal structure. The fibre elongates along the [001] direction. In the ED image of position D, separate diffraction spots can be observed around the primary spots (as indicated by the orange arrow), indicating low angle grain boundaries. .... 103

Figure 4.9. Illustration of the crystal structure relationships between  $\gamma$ -alumina (cubic, red),  $\delta$ -alumina (orthorhombic, orange) and  $\alpha$ -alumina (rhombohedral, fade pink). The unit cell of  $\alpha$ -alumina is drawn as hypothetical ideal hexagonal close packing, so that the parameter c is equal to the cubic body diagonal. .... 104

Figure 4.10. TEM and ED images of  $\alpha$ -alumina nanofibres taken from different positions. The fibres elongate along different directions as indicated in the image..... 105

Figure 5.1. (a) Schematic illustration of sparse nanofibres collected with two wood pieces in parallel for individual fibre tensile testing; (b) After fibre mat was peeled from the wood and calcinated, the fibre mat was broken to expose more isolated fibres. .... 109

Figure 5.2. Schematic of the custom-built AFM system used for nanofibre tensile testing. The enlarged region illustrates alumina nanofibres fixed between the TEM lift-out grid and AFM probe. ....	111
Figure 5.3. SEM images showing a typical procedure for tensile test of an individual alumina nanofibre. (a) The AFM probe first contacts an individual alumina nanofibre protruding from the bulk mat; (b) One end of the fibre is fixed to the tip of AFM probe (right) followed by translation of a TEM lift-out grid containing a small amount of SEM glue (left) into contact with the other free end of the fibre and (c) a focused electron beam is used to cure the glue to allow fibre fixation and subsequent tensile testing until (d) the alumina nanofibre fractures towards the middle of the fibre free length. ....	112
Figure 5.4. Signal of laser intensity versus cantilever recorded by optical fibre. ....	113
Figure 5.5. Illustration of bending of AFM probe and stretching of SEM glue (a) before and (b) during tensile testing. ....	114
Figure 5.6. (a) (b) TEM bright-field image and electron diffraction pattern of single crystal $\alpha$ -alumina nanofibre; (c) (d) TEM bright-field image and high resolution TEM image of polycrystalline $\gamma$ -alumina nanofibre. ....	115
Figure 5.7. Plot of the variation in tensile strength of individual polycrystalline $\gamma$ -alumina nanofibres and single crystal $\alpha$ -alumina nanofibres with fibre diameter. ....	116
Figure 5.8. (a) Polycrystalline $\gamma$ -alumina nanofibre bended under force; (b) After the bending force being released, the fibre restored to straight without apparent damage. ....	117
Figure 6.1. Schematic illustration of (a) alumina reaction with MPS; (b) condensation of hydrolyzed MPS. ....	122
Figure 6.2. (a) Schematic showing electrospinning of aligned PAN/AP fibre mat. (b) Schematic illustration of fibre mat formed with aligned fibres rolled to fibre bundle. ....	124
Figure 6.3. Illustration of fabricating polycarbonate composite reinforced with aligned alumina nanofibres with solution impregnation method. ....	126

Figure 6.4. Scanning electron microscopy images of the aligned nanofibre mat after electrospinning for (a) 10 min; (b) 1.5 h and (c) after calcination. ....	127
Figure 6.5. (a) FTIR of alumina nanofibres before and after surface modification; (b) EDS spectrum of alumina nanofibres modified with MPS. ....	129
Figure 6.6. Scanning electron microscopy images of composite cross-sections of (a) AF/PC-BSM and (b) AF/PC-ASM. ....	130
Figure 6.7. Stress-strain curves of polycarbonate composites reinforced with alumina nanofibres before and after surface modification with a concentration of (a) 3.9 vol%, (b) 10 vol% and (c) 15 vol%, respectively. ....	131
Figure 6.8. Comparison between tensile strength and Young's modulus of composites reinforced with aligned alumina nanofibres before and after surface modification. ....	132
Figure 6.9. Porosity of the composites reinforced with different volume fractions of alumina nanofibres. ....	133
Figure 6.10. Schematic illustration of shear lag model. (a) Unstressed composite system; (b) stress $\sigma_L$ applied along the fibre direction. ....	135
Figure 6.11. (a) Length and (b) diameter distribution of nanofibres in composites after hot pressing. ....	137
Figure 6.12. Comparison between theoretical Young's modulus and composite reinforced with aligned alumina nanofibres after surface modification. ....	138
Figure 7.1. The endothermic curves of (a) 5W-AF/PC composites and (b) 10W-AF/PC composites after annealing at 190 °C for different time; (c) Heat of fusion change of both composites 5W-AF/PC and 10W-AF/PC after annealing at 190 °C. ....	148
Figure 7.2. Scanning electron microscopy images show cross-section of AF/PC composites (a) without annealing, after annealing at 190 °C for (b) 0.5 h, (c) 24 h and (d) 24 h, respectively. Sample shown in (a) (b) (c) were prepared by broken in liquid nitrogen, while sample shown in (d) was broken by hand at room temperature. ....	151

Figure 7.3. AFM topographic image (a) and phase image (b) of polycarbonate composite reinforced with 1 wt% alumina nanofibres before annealing. AFM topographic image (c) (e) and phase image (d) (f) of the same composite annealed at 190 °C for 12 h and 24 h, respectively. ....	152
Figure 7.4. Force-displacement curves of amorphous and crystallized polycarbonate.	154
Figure 7.5. (a) Stress-strain curves, (b) tensile strength and (c) Young's modulus of 5W-AF/PC composites after annealing at 190 °C for different time. ....	156
Figure 8.1. Dependence between alumina nanofibre strength and fibre diameter with linear fitting. ....	161

# List of symbols

$a_0$	Lattice parameter of a cubic crystal
$c$	Brunauer-Emmet-Teller (BET) constant
$d$	Distance between the interplanar spacings
$d_{hkl}$	Distance between the crystal lattices of a specific plane marked as (hkl) by the Miller indices
$D$	Diameter of the fibre
$E$	Young's modulus
$E_L$	Young's modulus of the composite along the fibre direction
$E_m$	Young's modulus of the matrix
$E_f$	Young's modulus of the fibre
$E_c$	Young's modulus of the composite
$E_1$	Heat of adsorption for the first layer
$E_2$	Heat of adsorption for the second and higher layers and is equal to the heat of liquefaction
$F$	Force
$F_L$	Force applied on the composite along the direction of fibre alignment
$F_T$	Force applied on the composite transverse to the direction of fibre alignment
$G_m$	Shear modulus of the matrix
$h$	Planck's constant

$k$	Spring constant of the probe cantilever
$K_R$	Constant, and can be selected according to different ways that the fibres are arranged
$l$	Length of the fibre
$l_c$	Critical fibre length for reaching the highest fibre stress
$l_{cb}$	Cantilever bending distance
$l_{cm}$	Moving distance of the AFM stage
$l_{ge}$	Stretching distance of the glue
$l_t$	Minimum fibre length for the fibre to reach the highest fibre stress
$m$	Mass of the total material
$n$	An integer constant
$N$	Avogadro constant ( $6.022 \times 10^{23} \text{ mol}^{-1}$ )
$P$	Partial pressure of the adsorbate gas in equilibrium at the temperature of adsorption
$P_0$	Saturation pressure for the same condition
$r$	Fibre radius
$s$	Cross-sectional area of one adsorbate molecule
$S_{BET}$	Specific surface area
$v$	Quantity of the adsorbed gas at standard temperature and pressure
$v_m$	Monolayer adsorbed gas quantity at standard temperature and pressure
$v_f$	Fibre volume fraction in the composite
$V$	Molar volume of adsorbent gas
$x$	Distance of one point in the fibre away from the fibre end
$\varepsilon$	Strain
$\varepsilon_L$	Strain of the composite along the direction of fibre alignment

$\epsilon_{Lf}$	Strain of the fibres along the direction of fibre alignment
$\epsilon_{Lm}$	Strain of the matrix along the direction of fibre alignment
$\epsilon_T$	Strain of the composite transverse to the direction of fibre alignment
$\epsilon_{Tf}$	Strain of the composite transverse to the direction of fibre alignment
$\zeta$	An empirical shape factor, which describes measure of reinforcement of the composite material that depends on the fibre geometry, packing geometry and loading conditions
$\eta_s$	An length-dependent efficiency factor
$\lambda$	Wavelength of the electron beam
$\theta$	Incident angle of the electron beam
$\nu$	Quantity of the adsorbed gas at standard temperature and pressure
$\nu_m$	Monolayer adsorbed gas quantity at standard temperature and pressure
$\sigma$	Stress
$\sigma_L$	Stress applied on the composite in the composite along the direction of fibre alignment
$\sigma_{Lm}$	Stress applied on the matrix in the composite along the direction of fibre alignment
$\sigma_{Lf}$	Stress applied on the fibre in the composite along the direction of fibre alignment
$\sigma_T$	Stress applied on the composite in the composite transverse to the direction of fibre alignment
$\sigma_{Tm}$	Stress applied on the matrix in the composite transverse to the direction of fibre alignment
$\sigma_{Tf}$	Stress applied on the fibre in the composite transverse to the direction of fibre alignment

- $\sigma_f$  The stress applied on the fibre
- $\sigma_{f \max}$  The highest stress that the fibre can carry
- $\tau$  The shear stress at the fibre–matrix interface
- $\tau_i$  The smaller one of the shear strength of the fibre/matrix interface or the matrix adjacent to the interface



# 1 Introduction

## 1.1 Background

Polymers are commonly reinforced with various strong reinforcements to form composites with enhanced mechanical properties. The newly obtained composite usually exhibits properties that are improved relative to either of the component materials. Plenty of examples of composites can be found in our daily lives: components used for automobile and aircraft manufacturing, oil tank, water pipes and even doors and windows. While man-made composites are commonly found, nature also provides many examples of composite materials such as wood, which is made up of fibrous chains of cellulose molecules in a matrix of lignin. People from ancient times have also made many composite materials from natural materials. Papyrus paper, which dates back to 4000 B.C, is perhaps the first fibrous composite material made by ancient people.<sup>[1]</sup> Made from wood, horn and tendon, the recursive composite bow used by Mongolian soldiers is also notable as a very strong composite. All these materials exhibit improved mechanical performance relative to their constituents and arouse our curiosity to explore more about composite materials.

Composite materials can be classified into three main catalogues based on their structures (see Figure 1.1): (a) fibre-reinforced: aligned continuous fibres and short fibres (aligned or random); (b) particle-reinforced: large-particle and dispersion-strengthened; (c) other

structural: laminates and sandwich panels.<sup>[2]</sup> All of these structures identify a reinforcement that is bound together with a secondary phase referred to as matrix. The matrix is usually the softer phase and helps to transfer the load to the reinforcement, whereas the reinforcement is much stronger and stiffer than the matrix and gives the composite high strength and modulus. A particular advantage of composite materials is the ability to design structures through microstructure adjustment or choosing different matrix and reinforcement materials to meet different requirements.

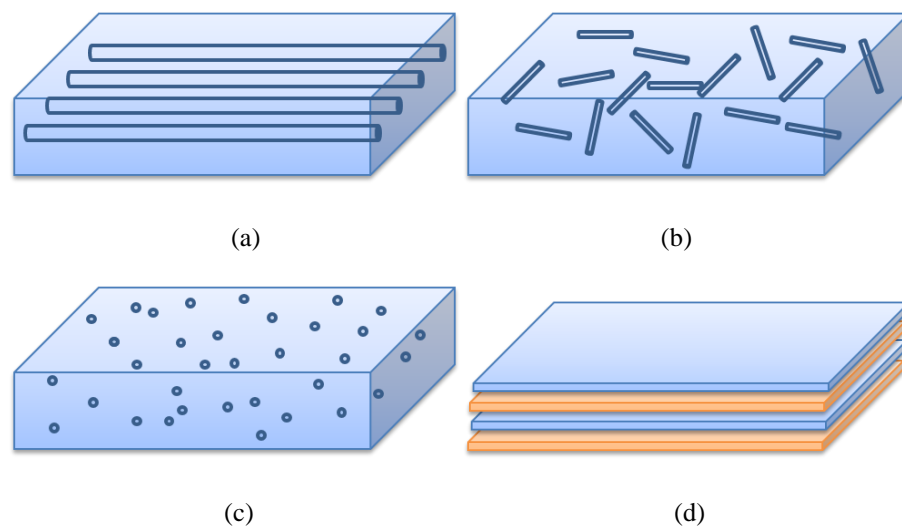


**Figure 1.1. Schematic illustration of composite reinforced with (a) continuous fibres, (b) short fibres, (c) particles and (d) laminate.**

Compared with traditional engineering materials such as steel and rubber, composite materials usually show much higher strength and elastic modulus. Composite materials are now used in a number of applications due to their excellent properties. Polymer composites with natural-organic fillers are made for door panels, roof upholstery and parcel shelves<sup>[3]</sup> whereas carbon nanofibre reinforced composites are commonly used to fabricate aircraft disk brakes because of their excellent thermal stability and light weight.<sup>[4]</sup> Dental materials reinforced with ceramic nanofibres have been shown significantly increased flexural strength and fracture toughness.<sup>[5]</sup> Indeed, researchers are still

developing many other composite materials that can be applied in an increasing number of areas, which signifies the bright future of composite materials. However, fabrication of composite materials is more complicated and expensive than many other materials due to the requirement of extended manufacturing procedures and times, including potentially higher temperatures and pressures. Thus, a lot of researchers have conducted thoroughly investigation into different parameters to fabricate composite with enhanced properties but lower cost.

One of the most efficient methods to fabricate strong composite is usage of strong reinforcement. The demand for reinforcements that provide high mechanical performance and are able to be easily, as well as cheaply, manufactured is therefore significant. The discovery of carbon fibres in the 1960s<sup>[6]</sup> prompted the manufacture of high performance carbon fibre reinforced plastic for aerospace structures and has recently grown into a range of consumer markets such as sports equipment. Carbon nanotubes were firstly identified in the early 1990s<sup>[7]</sup> and have since been the topic of intense research as well as applications as reinforcements in composite structures due to their excellent specific mechanical properties<sup>[8]</sup>. However, the high cost for carbon fibres force manufacturers to invent or discover other materials to serve as substitute. Alumina is a relatively cheap material with remarkable theoretical strength as high as 46 GPa, which makes alumina a strong reinforcement candidate to replace carbon fibres or other ceramics with adequate mechanical properties but less cost.<sup>[9]</sup> However, mechanical properties of brittle materials vary greatly depending on their microstructures. Currently, most alumina fibres used in industries are polycrystalline fibres with the highest tensile strength just reaches 3.3 GPa (3M, Nextel™ 610).<sup>[10-11]</sup> Compared with the 22.3 GPa, tensile strength of alumina whiskers along [110] direction reported by Soltis, the mechanical performance of polycrystalline alumina fibres are relatively poor.<sup>[11-12]</sup> The huge gap between the tensile

strength of alumina fibres and whiskers indicated great potential for further strength improvement.

Another important parameter in defining the resultant composite properties is the interaction between the polymer and fibre surface during processing of the composite. Strong bonding between the matrix and fibres enables more efficient stress transfer from the matrix to the reinforcement and improves the composite mechanical properties. Researchers have studied many different methods to increase the compatibility between polymer matrix and ceramic fibres, such as introducing of surfactants, plasma coating.<sup>[13-14]</sup> These methods sometimes have also been used to improve the fibre dispersion, which is very important for the composite since the overall strength is determined by the weakest part. Another phenomenon that may improve the interface is transcrystallization. Stress concentration could occur in the fibre/matrix interface in composite materials due to different thermal expansion coefficients of both components and sometimes, causing crystallization in thermoplastic matrices.<sup>[15-16]</sup> The formation of transcrystalline interface regions is typically induced in conventional fibrous composite materials but the consideration of similar effects with smaller scale nanofibres is less well recognised. However, though many researchers have reported positive effect of transcrystalline layer on the composite properties<sup>[17-21]</sup>, some other reported the opposite<sup>[22-23]</sup>. Thus, further investigation is needed to confirm the real impact of transcrystallinity on the composite properties.

To address the above questions and fabricate new composite with improved strength but lower cost and easier process, the method to fabricate alumina nanofibres with high strength and strong polymer matrix composites reinforced with strong ceramic nanofibres need to be investigated. A range of techniques will be applied to characterize various properties of both individual alumina nanofibre as well as the composite. Different

parameters affecting the nanofibre and the composite properties will be manipulated so as to push the composite reaching the highest strength.

## **1.2 Project aims**

Based on the descriptions above, fabricating strong but cheap fibres and composite becomes the key point of this work. The aim of this project is therefore to develop a method to produce strong alumina nanofibres and incorporate the nanofibres into composite materials to improve their mechanical properties. To achieve the overall aim, the objective is broken down into smaller milestones as follows:

1. Fabrication of alumina nanofibres with desired crystal structures and morphologies. Electrospinning will be applied to fabricate alumina nanofibres with polymer and inorganic precursor due to the simplicity and flexibility to control the fibre diameters. Different electrospinning parameters and calcination procedures will be controlled to investigate their influences on the final product morphologies as well as crystal structures. The mechanism of alumina crystal structure transformation will also be investigated thoroughly.
2. Tensile testing of individual alumina nanofibres. Tensile strength of the alumina nanofibres will be tested by a specific equipment to explore the structure-property performance of alumina nanofibres. Specifically, the influence of fibre diameters as well as crystal structures will be related to the fibre strength through examining the fibres with transmission electron microscopy and electron diffraction.
3. Fabrication and characterization of polycarbonate matrix composites reinforced with alumina nanofibres. The composite strength is expected to improve significantly after

being reinforced with strong fibres compared with the matrix itself. Uniaxially aligned alumina nanofibres before and after surface modification will be used in this work to examine the effects of introducing surfactant. Theoretical Young's modulus of the composite will be predicted based on the Halpin-Tsai theory and the shear lag theory as well. The predicted results would be compared to the experimental results to check the efficiency of the reinforcement.

4. Investigation into the effect of transcrystallization on the mechanical properties of polycarbonate composite reinforced with alumina nanofibres. The speed of polycarbonate crystallization can be significantly increased with the presence of alumina nanofibres under annealing at 190 °C. Different parameters affecting the transcrystalline layer formation process will be investigated by both direct morphology observation and indirect thermal behaviour studies. The effects of transcrystalline layer on the composite mechanical properties will be examined by mechanical testing.

## **2 Literature review**

### **2.1 Introduction to fibre-reinforced composite**

Fibre-reinforced composites are one of the most important areas of composite materials. In this type of composite, the reinforcement is typically strong and stiff fibres surrounded by matrix, which is usually homogenous and continuous. This section will give a brief introduction to load distribution in both continuous and short fibre-reinforced composites under load along and transverse fibre directions, different materials that can be used as matrices and fibres as well as how nanofibre-reinforced composites show distinct advantages when compared with traditional materials.

#### **2.1.1 Theory of fibre-reinforced composites**

Both continuous and short fibres are commonly used to reinforce polymer matrix for enhancing the composite stiffness. However, descriptions are required to understand how the fibre carries load and acts as reinforcement when the composite is loaded. Many researchers have proposed different theoretical models to predict the mechanical behaviour for fibre reinforced composites. Here we will consider two simple models regarding to both continuous and short fibres reinforced composite to investigate the basic parameters that affect the composite mechanical properties.

## 2.1.1.1 Unidirectional continuous-fibre composites

The rule of mixtures is the simplest approach used to analyse the loading process in continuous unidirectional fibre reinforced composite materials. In this model, the composite is simplified as two parallel slabs of matrix and fibres bonding together<sup>[24]</sup>, as illustrated in Figure 2.1. The two slabs have the same volume portion as the matrix and the fibres shown in composites respectively. When force  $F_L$  is applied along the fibre direction of the composites, the two slabs have the same strain,  $\varepsilon_L$ . The following equation can be derived according to the definition of Young's modulus:

$$\varepsilon_L = \varepsilon_{Lm} = \varepsilon_{Lf} = \frac{\sigma_{Lm}}{E_m} = \frac{\sigma_{Lf}}{E_f} \quad (2-1)$$

where  $\sigma$  represents the stress,  $E$  represents the Young's modulus, the subscript 'm', 'f' and 'L' represents matrix, fibre and longitudinal, respectively.

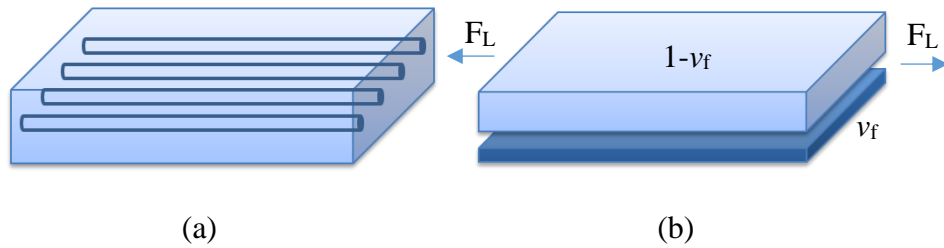


**Figure 2.1. Schematic illustration of (a) composite containing aligned, continuous fibres, and (b) the composite simplified as a model of two parallel slabs under load along fibre direction.**

Therefore, for composites fabricated with soft matrix and stiff fibres ( $E_f > E_m$ ), the fibres would carry most of the load ( $\sigma_{Lf} > \sigma_{Lm}$ ). If the volume fraction of the fibres is defined as  $v_f$ , and the volume of the matrix is  $1 - v_f$ , then the overall stress of the composite along the fibre direction can be expressed as:

$$\sigma_L = (1 - v_f) \sigma_{Lm} + v_f \sigma_{Lf} = (1 - v_f) \cdot \frac{E_m}{E_f} \cdot \sigma_{Lf} + v_f \sigma_{Lf} \quad (2-2)$$



The longitudinal Young's modulus of the composite  $E_L$  is therefore expressed as:

$$E_L = \frac{\sigma_L}{\varepsilon_L} = \left( (1 - v_f) \cdot \frac{E_m}{E_f} \cdot \sigma_{Lf} + v_f \sigma_{Lf} \right) \cdot \frac{E_f}{\sigma_{Lf}} = (1 - v_f) E_m + v_f E_f \quad (2-3)$$

If  $E_f \gg E_m$ ,  $E_L$  are approximated as

$$E_L = v_f E_f \quad (2-4)$$

This equation above shows that the longitudinal Young's modulus of the composite depends on the volume fraction and Young's modulus of the fibres.

When force  $F_T$  is applied transverse the fibre direction, the fibres and the matrix will be subjected to the same stress. An "equal stress" model is used to describe this situation, namely:

$$\sigma_T = \sigma_{Tm} = \sigma_{Tf} = \varepsilon_{Tm} E_m = \varepsilon_{Tf} E_f \quad (2-5)$$

Accordingly, the Young's modulus of the composite transverse the fibre direction can be derived as

$$E_T = \frac{\sigma_T}{\varepsilon_T} = \frac{\sigma_T}{v_f \varepsilon_{Tf} + (1 - v_f) \varepsilon_{Tm}} = \frac{\sigma_{Tf}}{v_f \sigma_{Tf} / E_f + (1 - v_f) \sigma_{Tm} / E_m} = \left( \frac{v_f}{E_f} + \frac{1 - v_f}{E_m} \right)^{-1} \quad (2-6)$$

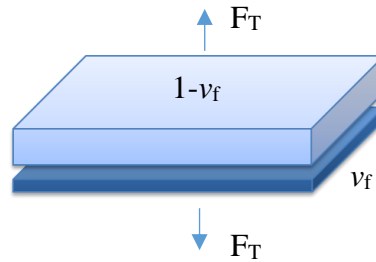


**Figure 2.2. Schematic illustration of composite containing aligned, continuous fibres simplified as a model of two parallel slabs under load along transverse fibre direction.**

The two Young's moduli of the composite in different directions reveal that the mechanical properties of fibre-reinforced composites are critically anisotropic and vary in different directions. For composites reinforced with uniaxially aligned fibres, the mechanical properties such as strength has the highest value in the longitudinal directional

of fibre but the lowest value in direction transverse to the fibre alignment. The volume fraction of the fibres also has a significant impact on the stiffness of composites. Specifically, the strength and stiffness of the composite along fibre direction increase as the fibre volume fraction in the composite increases, though the growth may not be linear.<sup>[25]</sup>

### 2.1.1.2 Unidirectional short fibre composite

The rule of mixtures model gives a description of a rather idealized case for composite reinforced with continuous fibres. In practice, the fibres used in composites are normally much shorter than the composite specimen. The stress transmission from the matrix to the fibres can be considered to be transferred through shear at the fibre/matrix interface. The matrix near the fibres in aligned short fibre reinforced composite is expected to have a higher longitudinal strain than the matrix far away from the fibres due to the lower matrix modulus when the composite is under load. Assuming the fibres and the matrix are perfectly bonded, a shear stress distribution will be created across the fibre/matrix interface in transverse direction (see Figure 2.3).

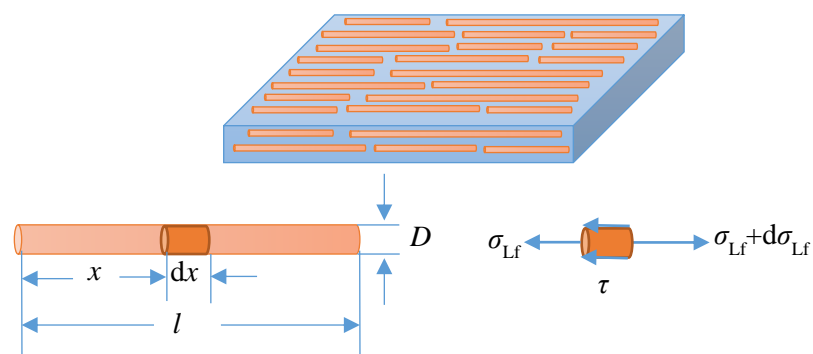


**Figure 2.3. Longitudinal tensile loading of a unidirectional discontinuous fibre lamina.**

Then the stress distribution<sup>[26]</sup> can be calculated according to force equilibrium by neglecting the stress variation at the fibre end:

$$\frac{\pi}{4} D^2 (\sigma_{Lf} + d\sigma_{Lf}) = \frac{\pi}{4} D^2 \sigma_{Lf} + (\pi D \cdot dx) \tau \quad (2-7)$$

This equation can be further simplified as:

$$\frac{d\sigma_{Lf}}{dx} = \frac{4\tau}{D} \quad (2-8)$$

where  $\sigma_{Lf}$  is the stress applied on the fibre in the composite along the direction of fibre alignment at the distance  $x$  from the fibre end,  $\tau$  is the shear stress at the fibre–matrix interface,  $D$  is the fibre diameter.

The shear stress can be assumed as constant across the fibre surface and equal to  $\tau_i$ , which is the shear strength of the fibre/matrix interface or the matrix adjacent to the interface.<sup>[27]</sup>

The stress applied on the fibre from the fibre end to a position  $x$  along the fibre axis can then be expressed as:

$$\sigma_{Lf} = \frac{4}{D} \int_0^x \tau dx = \frac{4\tau_i}{D} x \quad (2-9)$$

According to above analysis, the stress along individual fibres in the short fibre reinforced composite is non-linear. As shown in Figure 2.4, the fibre stress increases linearly with the distance from the fibre end  $x$  and reaches the highest value  $\sigma_{fmax}$  at the fibre central part where:

$$\sigma_{fmax} = 2\tau_i \frac{l_l}{D} \quad (2-10)$$

and  $l_l$  is the minimum fibre length for the fibre to reach the highest fibre stress. Therefore, the critical fibre length  $l_c$  for reaching the highest fibre stress can be expressed as:

$$l_c = \frac{\sigma_{fmax}}{2\tau_i} D \quad (2-11)$$

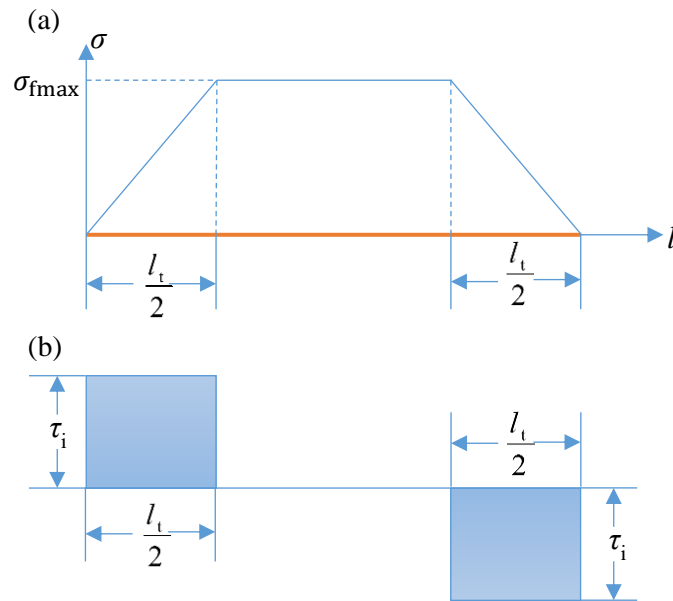


**Figure 2.4. Idealized (a) longitudinal stress and (b) shear stress on an individual fibre under load.**

The equations indicate that only when the fibre length is much larger than the critical length, the fibre can work efficiently as reinforcement. The analysis of fibres stress with different length is illustrated in Figure 2.5. If  $l < l_c$ , the matrix or the interfacial bonding fails before the build of the stress in the fibre is sufficient to cause fibre breakage. If  $l \geq l_c$ , the fibre stress will reach the fibre strength and cause failure. However, the reinforcement is not efficient over the distance equals to  $l_c$  in this situation. Therefore, for effective fibre reinforcement, the fibre length  $l$  need to be much longer than the critical length  $l_c$ . If the fibre length and diameter is fixed, the shear strength  $\tau_i$  can be controlled through surface modification to reduce  $l_c$  to a relatively low value so as to achieve effective reinforcement.

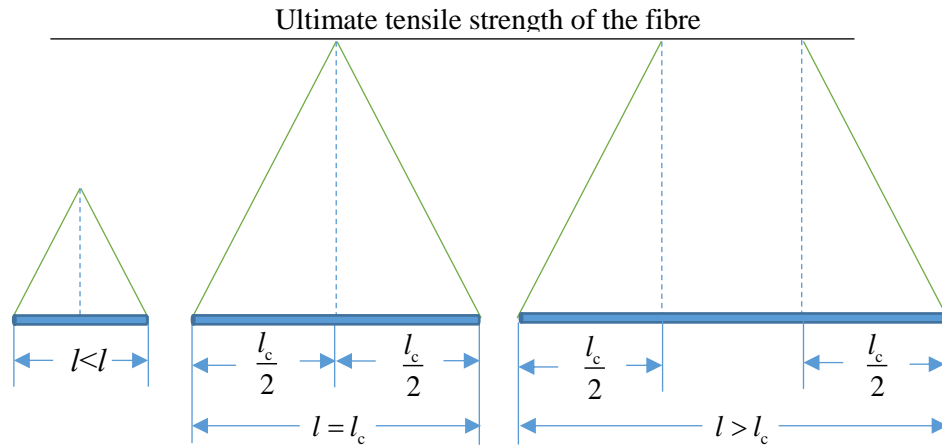


**Figure 2.5. Schematic illustration of critical fibre length on the longitudinal stresses of a discontinuous fibre.**

## 2.1.2 Components of composites

Properties of the composite are mainly determined by three factors: the matrix, the fibres and the interface between these two.<sup>[17]</sup>

### 2.1.2.1 Matrices

The matrix determines the shape and the surface qualities (such as thermal and electrical conductivity, thermal insulation, moisture sensitivity, et al.) of the composite but contributes limited mechanical support while the composite is under load. The stress between the fibres can also be transferred by the matrix to enhance the mechanical properties of the whole composite.<sup>[26]</sup> All these important characteristics of matrix make the selection of its material crucial.

The common choices of matrices are listed in Figure 2.6. Polymers are generally a popular choice for the matrix, due to their light weight, desirable mechanical properties and flexibility of fabrication. Thermoset polymers such as epoxies, polyesters, and vinyl esters usually have low viscosity, thus making them easy for processing and showing

more applications than thermoplastic polymers. However, thermoplastic materials are sometimes favourable since their shape can be modified after initial moulding. Metal matrices show better performance than polymers when serving in corrosive environment. Both ceramic materials and carbon-carbon composites can work at very high temperature environment but carbon-carbon composites have lower density<sup>[28]</sup>, thus they are widely used in aerospace.

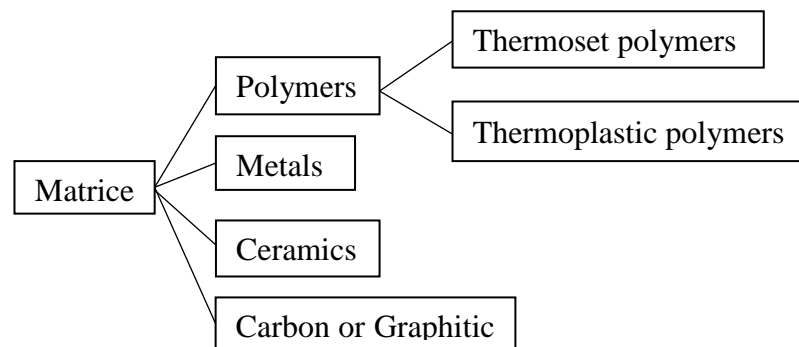


**Figure 2.6. Common materials used as matrices.**

#### 2.1.2.2 Fibres

Fibres typically carry most load and improve the stiffness in the composite. The strength and stiffness of the fibres are therefore one of the most important features of reinforcements<sup>[26]</sup> and requires load transfer from the matrix. Different materials, lengths, diameters and orientation of the fibres all have an important impact on the performance of the final product of the composite.

Examples of commercial fibres, such as glass, carbon, aramid, ceramics and polyethylene, are all playing important roles in current industry. Glass fibres are cheap, have high tensile strength and good chemical corrosion resistance properties. However, the glass fibres are sensitive to abrasion and their fatigue strength is relatively low.<sup>[26]</sup> The high strength to weight ratio of carbon fibres makes them one of the most important materials nowadays

and can be found in various areas such as aerospace, sports, civil engineering and laptops. However, carbon fibre products are usually more expensive than traditional products such as steel because of their more complex manufacturing.<sup>[29]</sup> Ceramic fibres have excellent mechanical properties and are notable as being thermally resistant, which makes them suitable for high temperature applications such as electrodes, catalyst supports and other power supply systems.<sup>[30-31]</sup>

### 2.1.2.3 Coupling agents and coatings

The interface formed between fibres and matrix materials is critical in defining overall composite performance. An effective composite that is able to transfer load from the matrix to reinforcing fibres requires good dispersion of fibres as well as efficient bonding at the fibre-matrix interface. The use of nanofibres as novel reinforcements is challenging as the nanofibres usually aggregate, making spreading of matrix between the nanofibres difficult during manufacturing. The resultant interfaces that form are therefore nanofibre-nanofibre instead of nanofibre-matrix interfaces, which promote sliding between the weakly contacting nanofibres in the aggregates during composite loading for poor mechanical properties.<sup>[32]</sup> To solve these problems and increase the performance of composites, materials such as coupling agents and coatings have been used in traditional composites.<sup>[33]</sup> Coupling agents are normally a substance that can react with both the matrix and the fibres to generate stronger bonding at the interfaces. Titanates<sup>[34]</sup>, zirconates<sup>[35]</sup> and organotrialkoxysilanes<sup>[36]</sup> are examples of common coupling agents that produce networked covalent bonded structures between a variety of fibres surfaces and functional groups in polymer matrices. Additionally, coating of the fibre is used to improve the wetting of the matrix to promote better bonding at interfaces as well as allowing impregnation of liquid matrix phased throughout the fibres during composite manufacturing. Mechanical properties have been shown to be strongly dependent on the

treatments applied to fibres. For example, the fracture behaviour and tensile strength of carbon nanofibre/polymer composites have been significantly improved after plasma treating the fibre surface to promote covalent bonding with the polymer.<sup>[32]</sup>

### **2.1.3 Ceramic nanofibres**

Both the models for long and short fibres have shown that the composite mechanical properties strongly depend on those of the fibres. Numerous works have been carried out in the past century to fabricate strong fibres close to theoretical strength and use them to make composite with better mechanical performance. Ceramic is one of the promising material candidates due to their high theoretical strength. However, the applications of ceramics are largely limited by the pores and other defects inside the materials. To improve the ultimate strength of ceramic materials, the influence of microstructure on mechanical properties has been extensively studied.

The presence of flaws is one of the factors that reduce the strength of ceramic significantly.<sup>[37-38]</sup> The flaw that has the sharpest shape and the largest size will give rise to the highest stress concentration, thus determining the ultimate tensile strength of the materials.<sup>[39]</sup> The possibility of reducing flaws that promote stress concentrations is intrinsically linked to fabricating fibres with reduced diameters. Such reduced fibre diameter tends to limit the flaw size and provides significantly increased mechanical properties, as has been demonstrated.<sup>[37, 40]</sup> This scale advantage makes ceramic nanofibres fabricated through electrospinning an effective reinforcement material.<sup>[41]</sup>

Nanofibres, defined as fibres with diameters less than several hundred nanometres<sup>[42]</sup> provide a promising method to achieve high strength. Griffith<sup>[37]</sup> studied the fracture stress of glass fibres with different diameters and found that fracture stress increased with



decreasing fibre diameter. The reason for the dependence of fracture stress on fibre diameters was suggested to be due to the microscopic flaws in the bulk material. Inspired by Griffith's pioneer work, nanofibres made from brittle materials such as ceramics and some polymers started to attract people's attention. Lee<sup>[43]</sup> compared Young's modulus between TiO<sub>2</sub> nanofibres with different diameters through atomic force microscope (AFM) three-point bending test, which displayed a clear trend of increased elastic modulus with decreased nanofibre diameter. Chen<sup>[41]</sup> also studied the relationship between the ZnO nanowires diameters and their Young's modulus (see Figure 2.7). When the diameters of these nanowires with diameters decreased to 120 nm, the Young's moduli increased significantly and are all significantly higher than that of bulk ZnO. These results of increased mechanical properties of ceramic nanofibres compared to bulk behaviour show great potential for future application of ceramic nanofibres as strong reinforcement in composite.

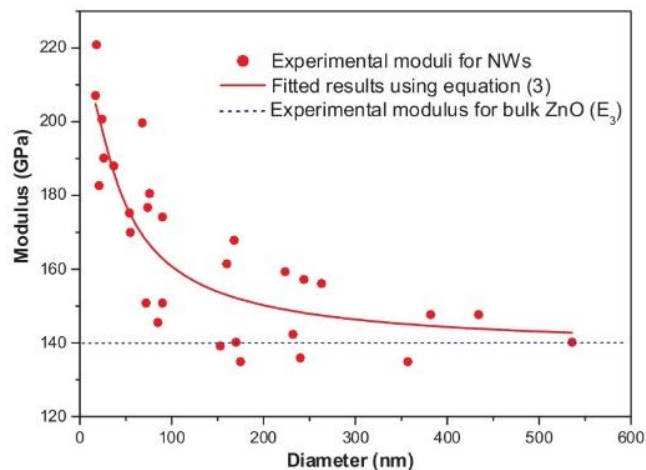


**Figure 2.7. Diameter dependence of effective Young's modulus in [0001] oriented ZnO nanowires from bending: (red dot) experimental results, (solid line) fitted results by the core-shell composite NW model, (dashed line) modulus for bulk ZnO (E<sub>3</sub>).<sup>[41]</sup>**

Ceramic nanofibres not only show improved mechanical properties comparing to the bulk phase, but also have significant changes in optical performance, energy density and some

other properties. Thus they have already been used in a lot of composite for various purposes. Composite made with epoxy resin and 2 vol% of barium titanate electrospun nanofibres increased by a factor of 3 compared with pure epoxy resin in terms of dielectric behaviour.<sup>[44]</sup> As for mechanical reinforcement, zirconia–silica nanofibres have been used to fabricate dental composite with dental resin monomers.<sup>[45]</sup> All these examples demonstrate huge potential for further application in composite in terms of strength improvement as well as other properties enhancement.

### 2.1.4 Polycarbonate

Polycarbonate was commercialized in 1958<sup>[46]</sup> and is now one of the most widely used engineering thermoplastics. Currently, all polycarbonate used for general-purpose are using bisphenol-A as the monomer (see Figure 2.8), and the final polymer normally has a molecular weight ranging 5000~70000.

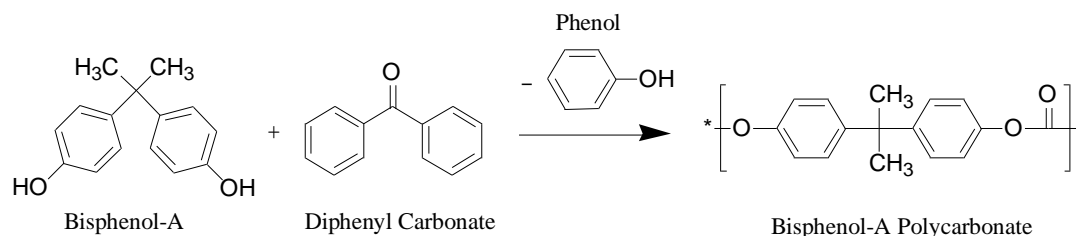


**Figure 2.8. Schematic illustration of synthesis of bisphenol-A polycarbonate.**

The principle advantages of polycarbonate include its excellent impact strength and toughness, excellent creep resistance, good heat resistance, good dimensional stability as well as transparency.<sup>[47-49]</sup> Thus, it has been widely used in industry, especially in areas where both optical clarity and good mechanical properties are required.<sup>[50]</sup> Despite of the advantages, polycarbonate certainly has its limitations. Though polycarbonate generally does not react with oils and acids, it can be affected by some chemicals, including most aromatic solvents, esters and ketones.<sup>[51]</sup> Polycarbonate has a limited scratch resistance

and tendency to yellow after being exposed in ultraviolet for a long time. While designing polycarbonate matrix composite, both the advantages and disadvantages need to be considered.

Many different kind of fibres, such as glass fibres<sup>[52-53]</sup>, carbon fibres or nanotubes<sup>[54-56]</sup>, natural fibres<sup>[57]</sup> and other ceramic fibres<sup>[58]</sup> have been used to reinforce polycarbonate to fabricate composites. Most of these composites are reported to have a significantly improved mechanical properties. Carneiro<sup>[59]</sup> has investigated both the mechanical and thermal properties of vapour-grown carbon nanofibre reinforced polycarbonate composite. The report reveals that the fibres delayed thermal decomposition of the matrix and the thermal stability has been improved. The hardness and Young's modulus of the composite have also been enhanced compared to pure polycarbonate, despite of the decrease of the friction coefficient. Multi-walled carbon nanotubes (MWCNT) has also been used as reinforcement in polycarbonate by many researchers. Eitan<sup>[60]</sup> reported that a 95% increase of the Young's modulus and a relatively low yield stress increase of around 32% were witnessed with incorporation of 5 wt% surface modified MWCNT. All these encouraging examples demonstrate a promising future of polycarbonate matrix composite reinforced with fibres with improved mechanical properties.

## **2.2 Fundamentals of alumina**

Among all ceramic materials, alumina stands out for a number of advantageous properties including high compressive strength, chemical stability, electrical insulation, corrosion resistance, low thermal conductivity, high-temperature resistance (melting point around 2000 °C) and low cost<sup>[61-62]</sup>, which makes alumina an important structural material. Nanofibres made from alumina retain all the advantages of bulk alumina but have been of interest due to potential variation in properties as the material becomes smaller and

increased strength-to-weight ratio, showing broad market prospects in various areas, such as building, refractory and insulators.

Composites based on alumina nanofibres have already been extensively studied. However, most current alumina nanofibre applications still focus on their insulation and heat resistance properties, such as composites made of branched alumina nanofibres and thermal conductive resin used to help electronic devices with problems of heat accumulation<sup>[63]</sup>. *Alumina nanofibres exhibiting strength approaching a theoretical maxima are expected to replace carbon nanofibres and provide composites with comparable mechanical properties but at lower cost. Methods to fabricate alumina nanofibres are critical in achieving high performance and will be discussed in this section.*

### **2.2.1 Fabrication of alumina nanofibres with electrospinning**

Various methods have been used by previous researchers to fabricate alumina nanofibres, for example, using hydrothermal<sup>[33, 64-65]</sup>, sol-gel route<sup>[66]</sup> and electrospinning<sup>[67]</sup>. Nanofibres prepared from the sol-gel and hydrothermal methods are usually thin and short whereas electrospinning provides continuous fibres with sufficient control to vary fibre diameters accurately. Electrospinning was invented in the late 19<sup>th</sup> century and has been predominantly exploited to fabricate polymeric fibres, with ceramic nanofibres produced relatively recently.<sup>[40]</sup> Currently, more than 50 different kinds of ceramic nanofibres have been produced and applied in different areas such as sensors, catalysts and drug delivery components.<sup>[30]</sup>

The first alumina nanofibre, containing small amounts of boron oxide, was fabricated by Dai<sup>[68]</sup> using electrospinning, and has provided inspiration for manufacturing alumina

nanofibres with different diameters and grain size using further materials as shown in Table 2.1. The alumina precursors provide a source of aluminium that was dissolved within a solution of polymer and a suitable solvent indicated in this table. The viscosity of the solution for electrospinning was controlled by altering the concentration of the polymer and is important in the effective production of fibres. After electrospinning, the calcination process will remove the organic parts in the as-spun nanofibres and produce ceramic nanofibres with desired crystal structure through controlled calcination procedures. Fibres produced with different ratios of materials and calcination procedures had a range of fibre diameters, morphologies and mechanical properties. The average diameter of these fibres produced using the materials in Table 2.1 is around 200-500 nm. However, though a progress has been made on fabrication of aluminium nanofibres, the mechanical properties of these fibres have yet to be measured.

**Table 2.1. Materials used to produce alumina nanofibres by electrospinning.**

Ref	Inorganic Precursor	Polymer	Solvent	Diameter of Al <sub>2</sub> O <sub>3</sub> nanofibre	Grain Size
[67]	Aluminium 2,4-pentanedionate	PVP	ethanol	150 nm	3-5 nm
[69]	Aluminium 2,4-pentanedionate	PAN	DMF	150-500 nm	10 nm
[70]	Aluminium di-sec-butoxide ethylacetoacetate	/	Ethanol and HCl <sub>aq</sub>	<200 nm	/
[71]	Aluminium acetate	PVA/PEO	water	20-500 nm	/
[72]	Anhydrous AlCl <sub>3</sub>	PVP	ethanol	100-800 nm	/
[73]	Boehmite nanoparticles	PVA	water	200-300 nm	/
[74]	Al(NO <sub>3</sub> ) <sub>3</sub>	PAN	DMF	200-350 nm	/

## 2.2.2 Crystal structures of alumina

Ceramics usually have several different crystal structures, and the transformation procedure of these crystal structures are strongly determined by the calcination process. For better manipulating the mechanical properties of the final alumina nanofibres products, the structure of common alumina crystals and their transformation relationship need to be understood thoroughly.

### 2.2.2.1 Common crystal structures of alumina

Alumina has more than 20 different crystalline forms<sup>[75]</sup> due to various possible atom arrangements<sup>[76]</sup>. The alumina crystal structures can be divided into two types based on the oxygen atoms arrangements: face-centred cubic (fcc) or hexagonal close-packed (hcp). Some of the common crystal structures of alumina are listed in Table 2.2.

The transformation sequences of alumina between these different structures are organized and displayed in Figure 2.9 depending on different starting status. As shown in this figure, both the starting status of the raw materials and the heating processes have profound impact on the transformation sequences of alumina. However, despite of the complex intermediate status, , the final product after calcination above 1100 °C is always  $\alpha$ -alumina.<sup>[77]</sup>

**Table 2.2. Several common polymorphs of alumina.**

Polymorph	Arrangements of oxygen atoms	Crystal system
$\alpha$	hcp	trigonal
$\beta$	/	hexagonal
$\gamma$	fcc	cubic
$\delta$	fcc	tetragonal / orthorhombic
$\eta$	fcc	cubic
$\theta$	fcc	monoclinic
$\kappa$	hcp	orthorhombic
$\chi$	hcp	hexagonal

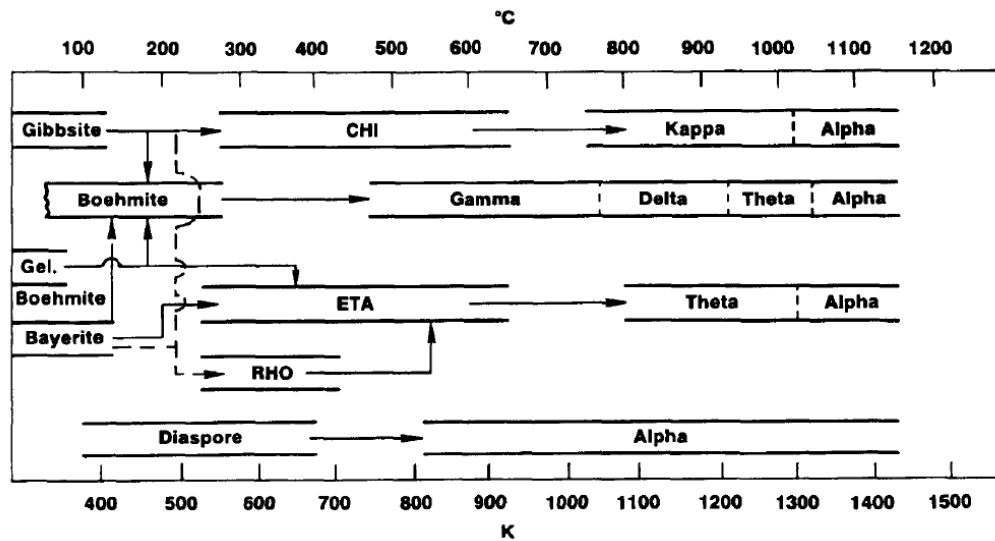


**Figure 2.9. Schematic illustration of alumina crystal structure transformation sequences from different start materials.<sup>[78]</sup>**

Alumina nanofibres prepared through electrospinning have been reported by several other researchers<sup>[67, 69, 71, 79-80]</sup> and the crystal transformation are mainly reported as  $\gamma\text{-Al}_2\text{O}_3 \rightarrow \delta\text{-Al}_2\text{O}_3 / \theta\text{-Al}_2\text{O}_3 \rightarrow \alpha\text{-Al}_2\text{O}_3$ . Among all the four crystal structures involved in alumina nanofibre fabrication,  $\alpha$ -alumina is the strongest and the stiffest form. Generally, the

complete conversion to  $\alpha$  phase requires calcination to occur for more than 1 h at 1200–1300 °C.<sup>[12]</sup> The transformation between these four crystal structures are very sensitive to the calcination procedures. However, the details about the transformation procedure and how the fibre shape was kept haven't been clearly explained in these works. To have a better understanding of the growth mechanism of alumina nanofibres, details about these four crystal structures need to be explored in priority.

$\gamma$ -Alumina ( $Fd\bar{3}m$ , no. 227) is one of the common unstable phases and will transform to  $\delta$ -alumina after being exposed under 700–800 °C.  $\gamma$ -Alumina has a typically described as defect spinel structure<sup>[81]</sup> with cubic closed-packed oxygen atoms and the aluminium atoms occupying both octahedral and tetrahedral interstitial locations, as shown in Figure 2.10.<sup>[82]</sup> One characteristic of  $\gamma$ -alumina that stands out is the low surface energy, which helps  $\gamma$ -alumina maintain small size and large specific area, making it very useful as catalyst support.<sup>[83]</sup> However catalysts made of  $\gamma$ -alumina can't be used under too high temperature since it will transform to more stable phase ( $\alpha$ -alumina).

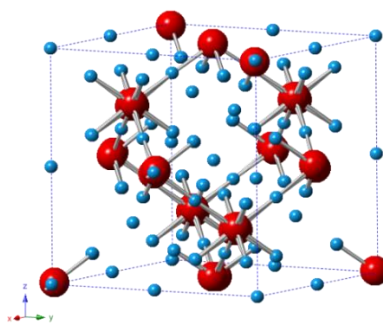


**Figure 2.10. Conventional unit cell of  $\gamma$ -alumina (blue spheres: aluminium; red: oxygen).**

$\delta$ -Alumina is one of the transition crystal structures that appear between  $\gamma$  and  $\alpha$  alumina and is normally viewed as a superstructure of  $\gamma$  phase.<sup>[84]</sup> Two unit cells for  $\delta$ -alumina have been identified currently according to previous researchers. One has a tetragonal unit cell and space group of  $P\bar{4}m2$  (no. 115)<sup>[85-86]</sup>; while the other one has an



orthorhombic unit cell and space group P222 (no. 16)<sup>[87-88]</sup>. But both  $\delta$  phases have a tetragonal lattice for oxygen arrangements. The reported tetragonal  $\delta$ -alumina are transformed from a starting status as boehmite (AlOOH), and orthorhombic  $\delta$ -alumina are transformed through thermal oxidation from precursor or quenched melt.<sup>[84, 87]</sup>

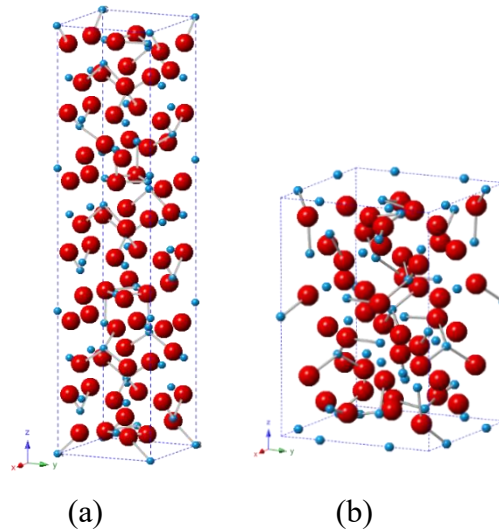


**Figure 2.11. Conventional unit cell crystal structure of  $\delta$ -alumina with both tetragonal and orthorhombic crystal systems (blue spheres: aluminium; red: oxygen).**

The crystal structure of  $\theta$ -alumina is normally considered as a defect-free monoclinic structure<sup>[89]</sup> (space group C2/m, no. 12), with half of the  $\text{Al}^{3+}$  ions are in octahedral sites and the other half in tetrahedral sites.<sup>[84, 90]</sup> The research and application of  $\theta$ -alumina is very limited due to the favourable transformation to  $\alpha$  phase.

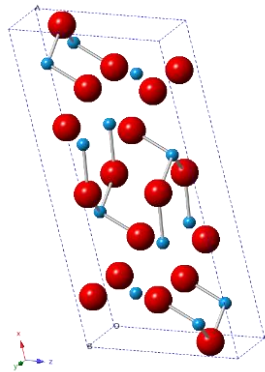


**Figure 2.12. Conventional unit cell of  $\theta$ -alumina (blue spheres: aluminium; red: oxygen).**

$\alpha$ -Alumina is the most stable phase compared to all other phases and it has the highest strength due to the specific ionic-covalent bonding of this material. Bonding in  $\alpha$ - $\text{Al}_2\text{O}_3$  is mainly ionic, with a proportion of covalent bonds accounting around 20%.<sup>[91]</sup> As shown in Figure 2.13, the crystal structure of  $\alpha$ -alumina can be described as octahedral formed by hexagonal close packing of O atoms with a space group:  $R\bar{3}c$  (No. 167). Each Al atom is located at an octahedral interstice, and is linked to three oxygen atoms in each of the two neighbouring oxygen planes. The  $[\text{AlO}_6]$  octahedrons may constitute a layer by sharing edge, which is perpendicular to threefold axis, at the direction parallel to threefold axis, the hexagonal platelet (prism) is formed by the interval arrangement between two kinds of octahedrons:  $[\text{AlO}_6]$  octahedrons which are stacked by sharing-facet and octahedrons which are surrounded by  $\text{O}^{2-}$ , and three-fold axis is formed by linkage of  $[\text{AlO}_6]$  octahedrons along c-axis.

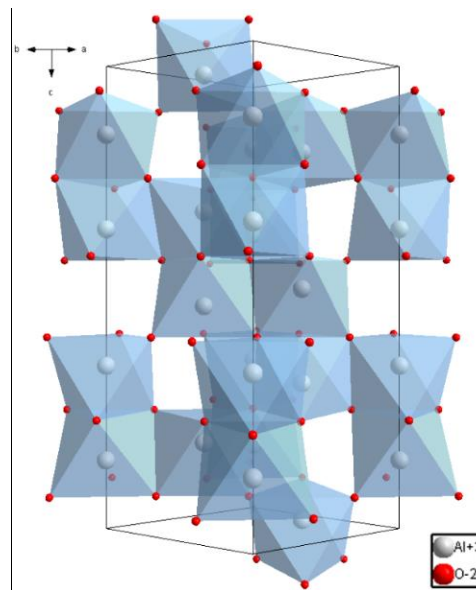


**Figure 2.13. Schematic illustration of crystal structure of  $\alpha$ -alumina.**

#### 2.2.2.2 Transformation from $\gamma$ -alumina to $\alpha$ -alumina

Understanding of the transformation mechanism from  $\gamma$  phase to  $\alpha$  phase is necessary to fabricate alumina nanofibres with desired morphology and mechanical properties.

However, no consistent conclusions have been reached regarding to transformation mechanism between these different crystal structures, despite extensive efforts. Three different routines have been reported currently for the explanation of transformation from  $\gamma$  phase to  $\alpha$  phase:  $\gamma \rightarrow \alpha$ <sup>[92]</sup>,  $\gamma \rightarrow \delta$  (tetragonal)  $\rightarrow \theta \rightarrow \alpha$ <sup>[84-85, 93]</sup>, and  $\gamma \rightarrow \delta$  (orthorhombic)  $\rightarrow \alpha$ <sup>[87, 94]</sup>.

Chou<sup>[92]</sup> has studied the transformation process from  $\gamma$  phase to  $\alpha$  phase directly without observing the intermediate  $\delta$  or  $\theta$  phase. According to the report, the phase transformation from  $\gamma$  to  $\alpha$  phase occurred by a nucleation and growth mechanism. The nucleation sites dwell on the  $\{220\}$  planes of  $\gamma$ -Al<sub>2</sub>O<sub>3</sub> since the layered structure formed high-population structural defects. After nucleation, the  $\alpha$  phase experienced explosive grain growth following the mechanism of interface boundary migration and lattice epitaxy due to several lattice match between  $\gamma$  and  $\alpha$  phase. However, Levin<sup>[76]</sup> has pointed that the work that they presented has some contradictions and the electron diffraction pattern of the polycrystalline  $\gamma$  phase could actually be the  $\delta$  or  $\theta$  phase.

The transformation of alumina from  $\gamma$  phase to  $\alpha$  phase via tetragonal  $\delta$  phase and monoclinic  $\theta$  phase started from boehmite is one of the most widely accepted transformation procedure and has been studied deeply.<sup>[85, 95-96]</sup> The transformation from  $\gamma$  to  $\delta$  and  $\theta$  phase follow a topotactic transformation and only need very small energy. The transformation from  $\theta$  to  $\alpha$  phase starts from nucleation and grain growth, leading to formation of a vermicular grain structure.<sup>[95]</sup>

Jayaram<sup>[87]</sup> has studied the transformation procedure from  $\gamma$ -alumina to orthorhombic  $\delta$ -alumina and concluded that both of these two phases have face centred cubic packing of oxygen atoms. Though, the  $\delta$  phase has a higher degree of aluminium atom ordering. The transition started from the spots of the disordered spinel and continuously transferred

through diffuse transformation until discrete superlattice reflections of the  $\delta$  phase appeared. However, this work reports that the orthorhombic  $\delta$  phase transformed from the melt  $\gamma$  phase has a space group of  $P2_12_12_1$  for the structure with  $a_\delta = 2a_\gamma$ ,  $b_\delta = 1.5b_\gamma$ ,  $c_\delta = a_\gamma$ .

Despite of the normal transformation of  $\theta$ -alumina from tetragonal  $\delta$ -alumina, monoclinic  $\theta$ -alumina transformed from orthorhombic  $\delta$ -alumina has also been reported by Gangwar.<sup>[97]</sup> However, most of the peaks in the XRD pattern of this  $\delta$  phase that they reported match well with the tetragonal  $\delta$ -alumina reported by Sergey<sup>[98]</sup>. Therefore, further confirmation is required for determination of the actual transformation procedure.

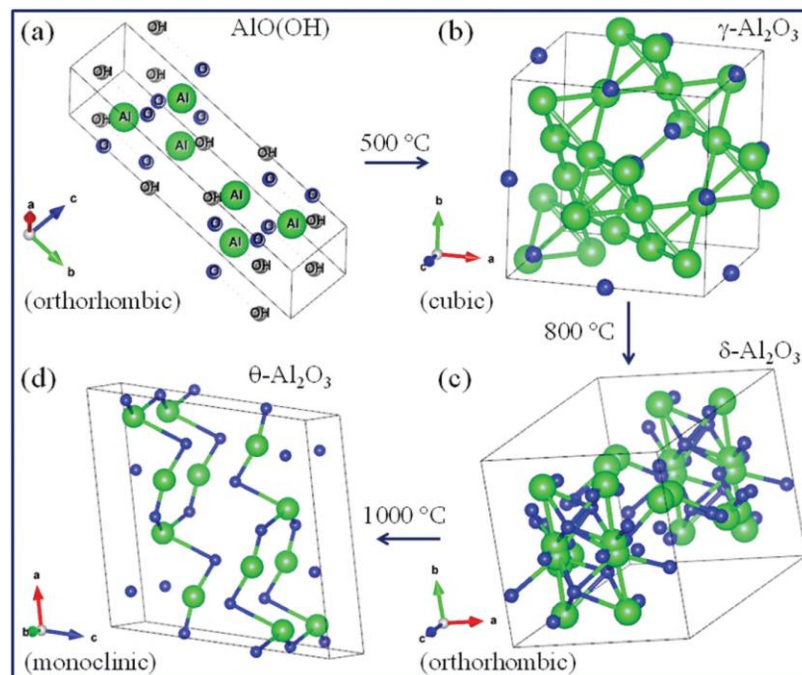


**Figure 2.14.** Unit cells of (a) uncalcined AlO(OH) (orthorhombic) and calcined Al<sub>2</sub>O<sub>3</sub>: (b)  $\gamma$ -Al<sub>2</sub>O<sub>3</sub> (cubic), (c)  $\delta$ -Al<sub>2</sub>O<sub>3</sub> (orthorhombic) and (d)  $\theta$ -Al<sub>2</sub>O<sub>3</sub> (monoclinic).<sup>[97]</sup>

Though extensive investigation of transformation between these crystal structures have been conducted, there's still many remained problems, such as the real transformation mechanism from orthorhombic  $\delta$  phase to  $\alpha$  phase and could  $\gamma$  phase truly transforms to

$\alpha$  phase without intermediate status. A lot of more work is required to answer these questions.

### **2.2.3 Growth mechanism and mechanical properties of $\alpha$ -alumina whiskers**

Monocrystalline whiskers are elongated single crystal materials that are normally regarded as defect-free, leading to extraordinary mechanical properties. Single crystal  $\alpha$ -alumina nanofibres fabricated through electrospinning have been reported previously by Yu<sup>[80]</sup>. The nanofibre share similar morphology and single crystal structure with alumina whiskers. Therefore, the growth mechanism and the mechanical properties of  $\alpha$ -alumina whiskers are good references for alumina nanofibres and will be briefly summarised firstly.

Alumina whiskers can be fabricated via growing on a single crystal alumina substrate by heating aluminium filings to 1400°C under the atmosphere of moist hydrogen.<sup>[99-100]</sup> The growth habit of  $\alpha$ -alumina has been confirmed by a lot of researchers. The main growth directions of these whiskers are  $\langle 0001 \rangle$ ,  $\langle 1\bar{1}20 \rangle$  and  $\langle 1\bar{1}00 \rangle$ , since these three directions are Burgers vector directions in  $\alpha$ -alumina and the whiskers can grow along these directions following a screw dislocation mechanism. Song<sup>[101]</sup> has reported that the orders of growth rate of  $\alpha$ -Al<sub>2</sub>O<sub>3</sub> various facets are  $\{001\} < \{113\} = \{1\bar{1}\bar{3}\} < \{110\}$ . The growth of  $\{001\}$  is inhibited in this crystallographic direction relative to the rate of growth in other predominant direction such as  $\{1\bar{1}3\}$ .

The tensile strength of alumina whiskers along these three directions have also been measured by Soltis<sup>[11]</sup>. The strength along three different directions are listed as: 10.9 GPa, 22.3 GPa and 15.3 GPa for direction  $\langle 0001 \rangle$ ,  $\langle 1\bar{1}20 \rangle$  and  $\langle 1\bar{1}00 \rangle$ , respectively. The tensile strength of the alumina whiskers is extremely high compared to its bulk phase,

which is only up to several hundred MPa. The current strongest commercial alumina fibre has a strength just reaching 3.3 GPa. The excellent mechanical properties of alumina whiskers indicate great potential for fabricating alumina nanofibres with extra high strength.

#### **2.2.4 Application of alumina fibres in composite**

Alumina fibres have been applied with various matrix including metal<sup>[102-103]</sup> and ceramics<sup>[104-105]</sup> to fabricate composite for increasing strength of these matrix materials. Polymers have also been used to fabricate composites with alumina fibres several decades ago.<sup>[106]</sup>

However, most of the applications of alumina fibres in composite focus on electrical properties. Alumina nanofibres have been fabricated into composites together with matrix such as epoxy and polyimide to enhance thermal conductivity of insulating materials for electric devices due to the heat conducting network build by the nanofibres as well as the high thermal conductivity of alumina.<sup>[106-108]</sup> In one of the few papers using alumina as reinforcement, both alumina nanoparticles and nanofibres have been used to reinforce epoxy matrices, and Young's modulus of the composites were confirmed as improved when adding reinforcement.<sup>[109]</sup> This previous work additionally highlighted the importance of the crystal structure of alumina, with  $\alpha$ -Al<sub>2</sub>O<sub>3</sub> providing the strongest crystal type when compared to the  $\gamma$ -Al<sub>2</sub>O<sub>3</sub> phase.

Despite of the wide application of alumina nanofibre, these applications are still limited by their relatively low strength. Therefore, huge potential of alumina fibres is expected if the alumina fibres with mechanical properties comparable to the alumina whiskers can be fabricated.

## 2.3 Electrospinning

Electrospinning is able to produce aluminium oxide nanofibres through a multi-step process and allows fibre diameter control. This section will give a brief introduction to the basic theory of electrospinning and important parameters that influence the process.

### 2.3.1 Electrospinning setup and procedures

A typical electrospinning setup consists of a syringe pump, a syringe, a needle, a high voltage power supply and a collector, as shown in Figure 2.15.

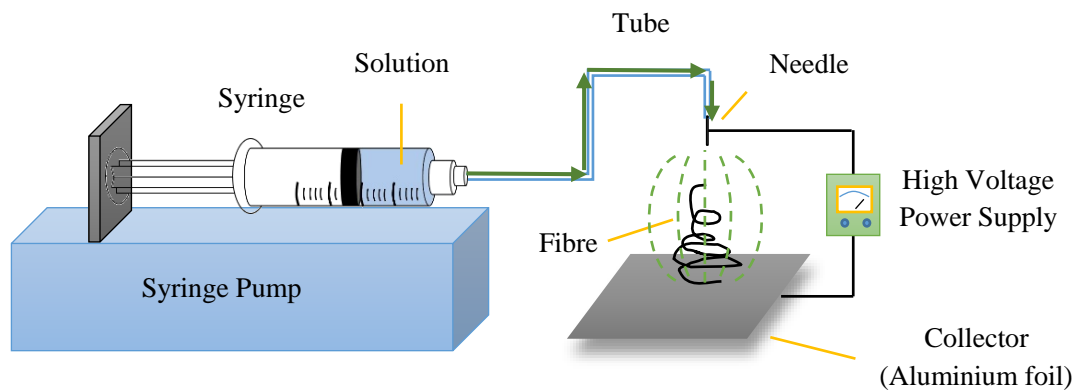


**Figure 2.15. Schematic illustration of typical electrospinning setup.**

A solution prepared from ceramic precursors, polymer and solvent first flows to a needle using a syringe pump, which is used to control the feed rate of the solution. The solution in the syringe flows through a tube which connects the syringe with a needle. The needle is charged by a high voltage power supply that normally applies a bias voltage ranging from 6 kV to 30 kV<sup>[42]</sup> between the needle and a collector material, which is normally conducting material such as aluminium foil. The sharp needle end provides an increase in the electric field and concentrates the electric charge provided by high voltage.<sup>[110]</sup> When the solution arrives at the tip of the needle, the solution drop at the end of the needle

experiences both the repulsion due to build up surface charge and drawing towards the collector from the action of the electric field. The deformation of the liquid droplet at the end of the needle forms a characteristic geometry known as the Taylor cone, which was described by Taylor<sup>[111]</sup> in 1964. Increasing the applied voltage causes an increase in the charge built up within the liquid droplet at the needle end until, at a critical voltage, charge repulsion overcomes the surface tension of the solution and a jet forms and is stretched out from the needle to the collector.<sup>[30]</sup> Due to bending instability and quick solvent evaporation during this process, progressive elongated and thinning of a liquid jet with nanometre-scale diameters occurs, resulting in deposition of solid nanofibres on the collector.<sup>[112]</sup> The continuous supply of the solution and high voltage ensure the continuous production of large quantities of nanofibres.

### **2.3.2 Parameters affecting electrospinning**

Electrospinning is a complex process and requires understanding of a number of different processing parameters. Many of these parameters interact with each other and affect the final nanofibre product including the resultant mechanical properties of the nanofibre. The most important processing parameters in electrospinning are discussed below.

#### **2.3.2.1 Solution viscosity**

The viscosity of electrospinning solution is essential in controlling the resultant spun fibres. Electrospinning stretches a liquid drop at the tip of the needle by an electric field to form fibres. The stretching of the solution is thus dependent on the viscosity of the solution with low viscosity solutions tending to break up into liquid droplets whereas higher viscosity solutions are able to be drawn into continuous smooth fibres. However, a relatively high solution viscosity requires significant electric fields in order to be drawn towards the collector, which may not be achievable with the power supply. The viscosity



of the solution should therefore be within a proper range i.e. not too low or not too high, and is defined by the amount of polymer within the solution. The most common polymers used in solution for fabricating ceramic nanofibres are poly(vinyl alcohol) (PVA), polyvinylpyrrolidone (PVP), poly(methyl methacrylate) (PMMA) and polyacrylonitrile (PAN).<sup>[30]</sup> The relationship between the concentration of these polymers and the solution viscosity has been studied systematically.<sup>[113-118]</sup> All these studies confirmed that higher concentration of polymers would give rise to higher viscosity of the solution and longer relaxation time, which eventually yield uniform nanofibres with less beaded structures.<sup>[119]</sup> The molecular weight of these polymers also has an effect on the viscosity of these solutions. Polymers with higher molecular weight usually have longer chains, and increase the chance of entanglement of the chains in the solution, leading to higher viscosity.<sup>[42]</sup>

#### 2.3.2.2 Voltage

During the electrospinning process, high voltage is required to cause the solution drop at the tip of the needle to form a Taylor cone as well as generate strong electric field to stretch the polymeric solution to form fibres. Voltage higher than a threshold value is necessary to form a stable Taylor cone and is dependent on the feed rate of the solution. Specifically, a relatively high solution feed rate to the needle requires a correspondingly large applied voltage to the spinning needle whereas a low solution feed rate requires lower applied voltage. The greater stretching force caused by an increasing electric field gives reduced fibre diameters. However, if the voltage continues to increase, the electrospinning jet will accelerate and more volume of the solution will be drawn out leading to a smaller and unstable Taylor cone<sup>[120]</sup>. The strong electric field also reduces the flight time of the electrospinning jet, therefore less time is left for the fibres to stretch and elongate. When the voltage exceeds this upper limit of the working condition,

spontaneous electron emission will cause the breakdown of the gas phase around the spinning needle to give a corona discharge<sup>[113, 121]</sup>.

Lee<sup>[122]</sup> and Yuan<sup>[123]</sup> reported that electrospun fibres were relatively straight when spinning from a relatively low voltage and became finer with an increased voltage. However, when the voltage kept increasing, fibres began to curve and the arrangement of the fibres was irregular due to the unstable whipping jets of the polymer solution as the Taylor cone receded into the needle. In this case, voltage sufficient for electrospinning but lower than the value that could cause spontaneous electron emission is appropriate for fabricating fine nanofibres.

#### 2.3.2.3 Feed rate

A suitable feed rate in electrospinning helps to provide adequate volume of solution to maintain a stable Taylor cone and keeps effective electrospinning. Higher feed rate normally gives rise to increased fibre diameters or beads sizes and a correspondingly higher voltage is required because more volume of solution needs to be drawn away from the tip of the needle.<sup>[42, 124]</sup> Wang<sup>[116]</sup> has investigated the relationship between the feed rate and the fibre diameters and the results showed that, when all the other parameters are kept at constants, the cone depth will increase with a raised feed rate, which leads to larger fluid jet size and larger fibre diameter. However, the effect of reducing fibre diameter with increased voltage contradicts the effect of increased feed rate, thus increased feed rate has a limited effect on raising fibre diameters. A problem with increased feed rate and voltage is that the solvent may not completely evaporate before the fibres deposit on the collector surface due to shortened flight time and increased amount of solvent, resulting in fibres fusing together. Therefore, lower feed rate is normally favoured to produce fine and dry fibres<sup>[125]</sup>.

#### 2.3.2.4 Distance between needle and collector

The distance between the needle and the collector affects the diameter and morphology of fibres by directly changing the electric field strength as well as the time for the fibre moving from the needle to the collector. A shorter distance gives rise to stronger electric field and less flight time when the voltage is kept constant. The stronger stretching force accelerates the electrospinning jet and further shortens the flight time of the fibre, which may result in insufficient time for the solvent to evaporate. Conversely, the electric field will be too weak to form the electrospinning jet if the distance between needle and collector is too large, thus fibres are not formed. The typical range for the distance between the needle tip and the collector is 10-30 cm<sup>[126]</sup>.

### 2.3.3 Aligned nanofibres fabricated with electrospinning

According to experience from traditional textile industry, maximum effect of the fibres can be achieved only when uniaxial oriented fibres are used.<sup>[29]</sup> To make full use of electrospinning and develop potential application, efforts have been made by researchers to obtain aligned fibres through different techniques.

One of the simplest way to collect aligned fibres is to use a drum<sup>[127]</sup> or disc<sup>[128-129]</sup> with a high rotating speed, see Figure 2.16. This method is capable to fabricate aligned nanofibres with a large area. However, alignment of fibres produced with this method is relatively poor<sup>[130]</sup>, thus other new collectors such as parallel electrodes have also been developed.

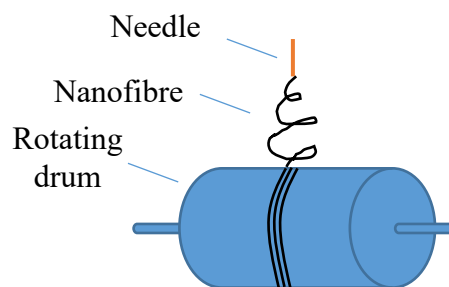


**Figure 2.16.** Schematic illustration of rotating drum for collecting aligned fibres.

Paralleled electrode was used by Li<sup>[131]</sup> in 2003 to collect aligned electrospun nanofibres, as shown in Figure 2.17. The collector is made up of two paralleled pieces of silicon wafers and the distance of the gap between the two wafers ranges from hundreds of micrometres to several centimetres. During electrospinning, the nanofibres were stretched by the electrostatic force and landed across the gap, forming aligned nanofibres. This method can produce nanofibres with a large area with very good alignment, however the thickness and length of the aligned fibres are limited.

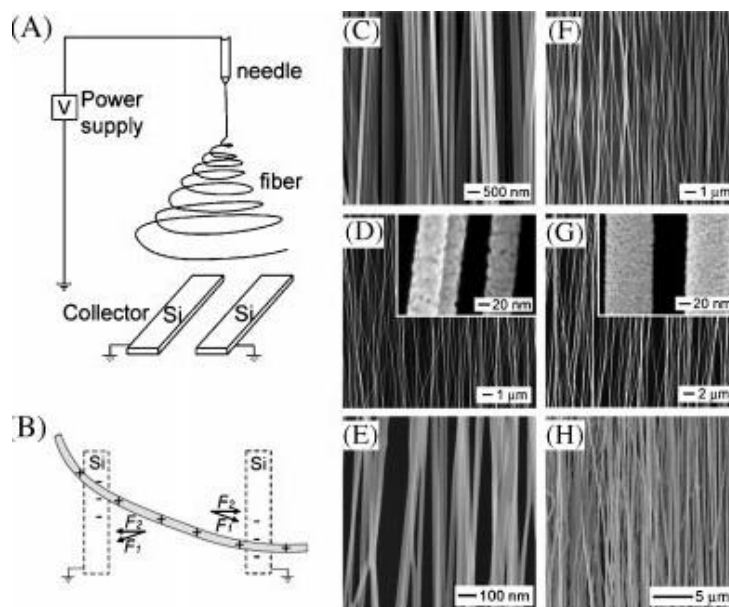


**Figure 2.17.** (A) Schematic illustration of the setup for collecting nanofibres with two strips of silicon wafers. (B) Schematic illustration of the electrostatic force working on nanofibres. (C–H) SEM images of aligned nanofibres made of (C) carbon, (D) anatase  $\text{TiO}_2$ , (E)  $\text{NiFe}_2\text{O}_4$ , (F)  $\text{TiO}_2/\text{PVP}$ , (G) Sb-doped  $\text{SnO}_2$ , and (H)  $\text{BaTiO}_3$ .<sup>[30]</sup>

Yan<sup>[132]</sup> has reported using parallel collectors with different dielectric material to obtain different electric field profiles so as to facilitate electrospinning aligned nanofibres, see Figure 2.18. Their results revealed that relative permittivity of the collector play important roles for deposition behaviour of the electrospun nanofibres. By using this collecting method, the fibres can have good alignment even with relatively low voltage.

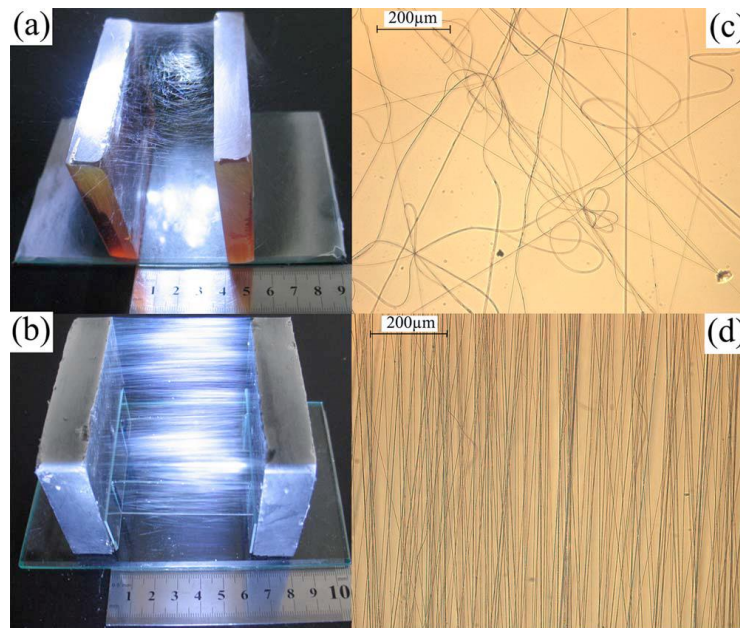


**Figure 2.18. (a) (b) Digital camera images of prepared nanofibre meshes using epoxy and ferrite as the collectors, respectively; (c) (d) Optical micrographs of (a) and (b).**<sup>[132]</sup>

Apart from the methods mentioned above, other methods such as using wire drum collector<sup>[133]</sup> or rotating tube collector with knife-edge electrodes below<sup>[134]</sup> have also been applied for fabricating aligned nanofibres. All of the methods have their advantages and disadvantages and different methods need to be selected or further developed for their special purposes.

## 2.4 Measurement of the mechanical properties of individual nanofibres

Measuring the ceramic nanofibre mechanical properties is crucial for composite design and other future application as well as providing information on optimized processing conditions. However, due to the extremely small scale of electrospun nanofibres, conventional testing methods are not applicable and advanced methods are required. Therefore, this section will briefly summarize some of the advanced methods proposed by previous researchers.

### 2.4.1 Nano tensile testing

Tensile testing is a fundamental method for obtaining characterizing mechanical properties including Young's modulus, yield strength as well as strain-hardening of the material at the same time. A suitable tensile test approach should follow conventional testing for relatively large materials i.e. tensile forces are applied to both ends of the fibre, causing deformation until failure. However, tensile testing of nanofibres is the most challenging mechanical method currently compared with other methods since the test requires direct application of force, ideally to an individual fibre with a diameter of the order of 100 nm, and manipulation of these extreme small fibres are required.<sup>[135]</sup> Through years of development, various methods for nanoscale tensile test have been studied by a lot of previous researchers.<sup>[136]</sup> The tensile test can be carried out with a nano tensile tester<sup>[137-138]</sup> or atomic force microscopy (AFM) cantilevers<sup>[136]</sup>.

Commercial nano tensile tester (Nano Bionix System, MTS, USA) has been used to test tensile strength of electrospun polycaprolactone nanofibre with diameters of  $1.4 \pm 0.3 \mu\text{m}$ .<sup>[137]</sup> As shown in Figure 2.19, fibres were electrospun on a plastic frame before testing.

After the frame is mounted in the tester, the frame was cut along the discontinuous lines before stretching the fibre. This nano tensile tester is able to conduct the tensile test of continuous fibres of a few millimetres to several centimetres in length. However, if the diameter of the fibre is too small to be observed optically, higher resolution imaging is then required to identify the number and dimensions of the fibres being tested.

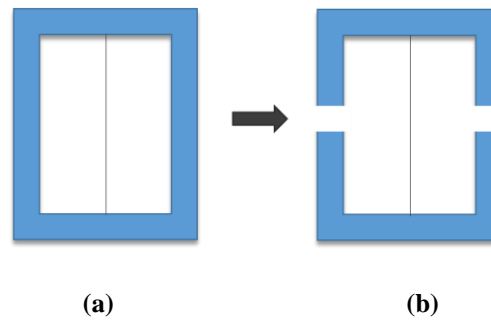


**Figure 2.19. Schematic showing electrospun fibres on a plastic frame used for nano tensile tester (a) before and (b) after cutting the frame.**

An AFM cantilever has shown improvements over the nano tensile tester by incorporation into an SEM to help observe the fibre.<sup>[139]</sup> Ever since the method has been applied by Yu<sup>[140]</sup> to test tensile strength of carbon nanotubes (see Figure 2.20), similar systems has been developed widely used for tensile testing of many nanofibres made from different materials. The basic principle for this system is simple. The fibre is normally fixed between two AFM probes or between one AFM probe and another stable object. Then the tensile testing is performed by withdrawing the AFM probe until the fibre breaks. The applied force can be calculated after measuring the spring constant of the cantilever and deflection of the AFM cantilever as observed in SEM. If stress-strain curve is required, a calibration with cantilever fixed directly on the stable object is required and the bending of the cantilever need be recorded with an optical fibre, as explained by Fei<sup>[141]</sup>. Tensile strength of polyethylene oxide nanofibres<sup>[136]</sup>, nylon-6,6 nanofibres<sup>[142]</sup>, multiwalled

nanotube/poly(methyl methacrylate) composite nanofibres<sup>[143]</sup> and even mineralized collagen fibrils from bone tissue<sup>[144]</sup> have all been tested with this system.

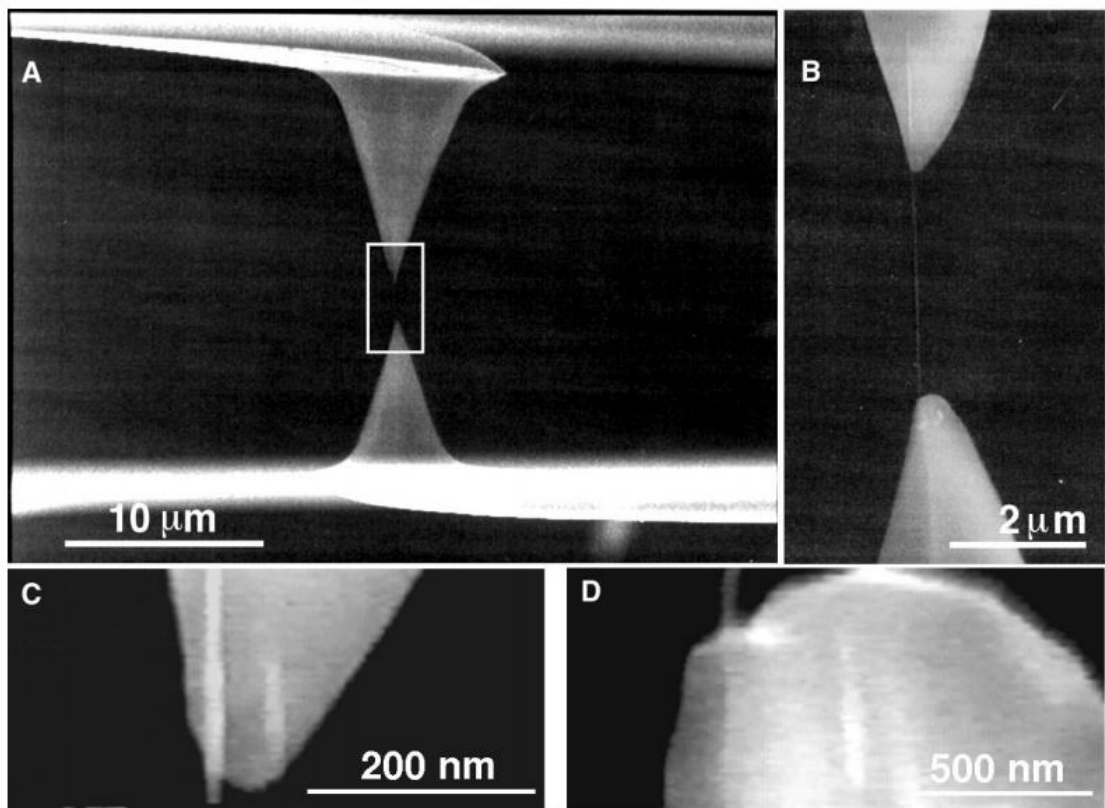


**Figure 2.20.** Scanning electron microscope images of individual MWCNT mounted between two opposing AFM probes.<sup>[140]</sup>

However, despite of the improved accuracy, operation of this method is still challenging and not all fibres are capable for this measurement due to the operation under vacuum and electron beam. Equipment much easier to operate is expected with development of these new technologies in the future.

## 2.4.2 Three-point bending test

Three-point bending testing is commonly performed to measure the flexural strength and Young's modulus of different materials. For a bending test at the nanoscale, precise force resolution down to the pico-Newton range is required, and this requirement makes AFM



an appropriate tool. The first attempt to use AFM to determine the mechanical properties of individual nanotubes was conducted in the late 1990s<sup>[145]</sup>. Generally, a bending test is performed by first placing a fibre on a substrate with holes or grooves, as shown in Figure 2.21. The location of the fibre is then acquired by using AFM topography imaging. The AFM probe then moves towards the middle of the fibre and applies a force to the fibre until the displacement reaches a set value. The attractive and repulsive force as well as the displacement of the AFM cantilever as the probe applied force to the fibre will be recorded by the system during the whole process.

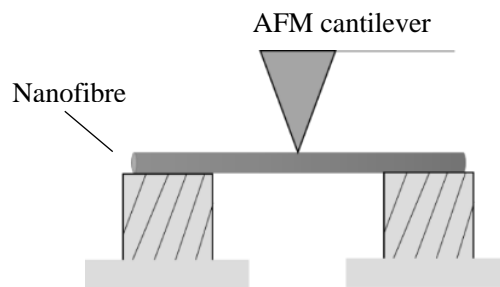


**Figure 2.21. Schematic showing of a nanofibre bending test using an AFM probe.**

According to beam bending theory, the Young's modulus of a clamped fibre can be calculated according to the following formula:

$$E = \frac{FL^3}{192\delta I} \quad (2-12)$$

Where  $E$  represents the sample's elastic modulus;  $F$  represents the applied force;  $L$  represents the suspended length of the fibre;  $\delta$  represents the deflection of the fibre;  $I$  represents the second moment area of the beam ( $I = \pi \cdot D^4/64$  for a filled cylinder,  $D$  is the cylinder diameter).<sup>[135]</sup> Thus, the elastic modulus of an individual electrospun fibre can be calculated from recording the force required to bend the fibre using AFM.

Almecija<sup>[146]</sup> has used similar method to measure the tensile properties of single nanofibres by suspending electrospun nanofibres over the notches on silicon substrates prepared previously. A theoretical model was applied to calculate the tensile strength and

Young's modulus of the fibres. However, it's not a direct measurement of tensile strength thus a certain degree of deviation from the actual value is expected. Young's modulus of electrospun titania nanofibres have been measured by Lee<sup>[43]</sup> with three-point bending test and the results clearly revealed the relationship between the nanofibre diameters and the mechanical properties.

The guarantee that no indentation happened during this experiment is very important, therefore this method is more suitable for measurement of hard materials such as ceramic fibres rather than soft materials such as polymer nanofibres.

### **2.4.3 Nanoindentation**

Nanoindentation is another way to test the elastic modulus and hardness of a nanoscale material.<sup>[147]</sup> This testing involves pushing an indenter probe into a sample and measuring the load and displacement of the probe in order to determine mechanical properties of the sample. Both elastic and elastic-plastic properties can be obtained through this method.

Nanoindentation of nanofibres are normally performed with AFM as nanoindenter, despite of the primary purpose of AFM in surface image scanning.<sup>[148-149]</sup> During the experiment, the sharp probe of AFM is pressed into the sample surface and the force-displacement curve during the process is recorded, as shown in Figure 2.22. Young's modulus of the sample can then be calculated according to indentation models built by Hertz<sup>[150]</sup> or other researchers. However, if models such as Hertz's theory are used, the curved surface of nanofibres should also be taken into account, since the Hertz's theory assumes that the indented sample is flat. The surface of the fibre can be considered as flat only if the fibre diameter is much bigger than the indenting AFM probe radius of curvature.<sup>[151]</sup>

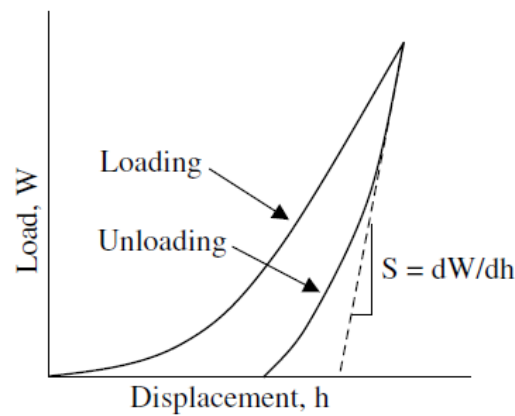


**Figure 2.22. Method of obtaining contact stiffness from the load–displacement curve.**<sup>[152]</sup>

Nanoindentation has been applied to measure mechanical properties of many fibre-like structures such as platelet graphite nanofibres<sup>[153]</sup>, magnetic nanofibres with iron oxide nanoparticles and poly(ethylene terephthalate)<sup>[154]</sup>, electrospun silk fibres<sup>[155]</sup> and ZnO nanowires<sup>[156]</sup>. Measurement of fibre Young's modulus with AFM nanoindentation has only been reported in a few papers, since the curved fibres surface makes it very difficult to perform the testing. Nevertheless, the results in these papers agree well with their bulk phase or other works.

#### 2.4.4 Oscillation methods

A number of other methods have been used to measure the mechanical properties of nanofibres due to their oscillation as an alternative to nanoindentation, bending and tensile testing mentioned above.

Yuya<sup>[157]</sup> used two AFM cantilevers to test the Young's modulus of single nanofibres suspended between two AFM cantilevers (see Figure 2.23). Young's modulus of the fibre was obtained by measuring the natural resonant frequencies of this cantilever-nanofibre system by AFM, which was related to the Young's modulus of the nanofibre bridging between the AFM cantilevers.

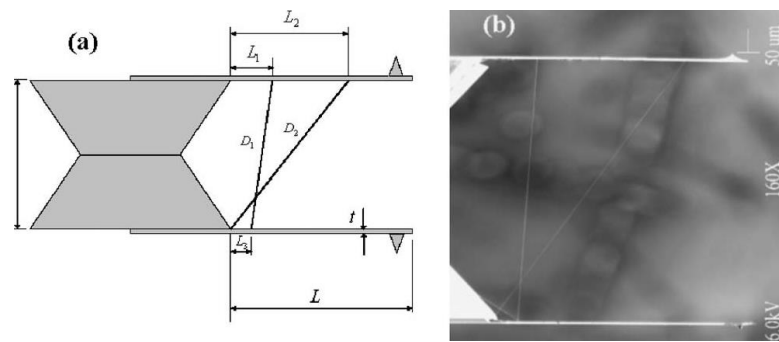


**Figure 2.23. (a) Schematic image and (b) SEM image showing nanofibres attached to two similar AFM cantilever probes.**<sup>[157]</sup>

Transmission electron microscopy (TEM) has also been used by Treacy<sup>[158]</sup> to determine Young's modulus of isolated carbon nanotubes by measuring the amplitude of their intrinsic thermal vibrations. This method confirmed the high modulus of these nanotubes. This method is limited due to the requirement of special setup in the vacuum chamber of TEM.

These different techniques have helped researchers learn the intrinsic mechanical properties of different materials and contribute for further composite fabrication. However, limitations of these methods in manipulating the fibres still exist nowadays and the development remains to be explored in new systems for observing the sample under test and manipulating the fibres easily.

## 2.5 Interface improvement between ceramic and polymers

Generally, methods used to modify the surface properties of materials can be divided into four categories, including: mechanical, combustion, chemical and plasma techniques.<sup>[159]</sup> However, mechanical methods are not applicable here due to the extreme small scale of the fibres. Thermal methods are also not suitable here since ceramics are normally

thermally stable. Thus, this section will focus on the latter two techniques, and give a brief introduction on surface modification with coupling agents and plasma treatment.

## **2.5.1 Coupling agents**

In inorganic materials reinforced polymer composites, bonding between the matrix and the reinforcement has always been a problem due to the different chemical compatibility between organic and inorganic materials. As mentioned in section 2.1.2.3, coupling agents can significantly enhance the interfacial bonding, thus play important role in deciding mechanical properties of the final composite materials. In this section, several coupling agents commonly used to improve the ceramic/polymer interface will be concisely introduced.

### **2.5.1.1 Silane**

Silane is one of the most frequently used coupling agent for forming strong bonding between organic and inorganic materials. For addition of silane to organic materials, silane help to improve wettability and miscibility between organic and inorganic materials. It can also form chemical or hydrogen bonding with organic materials, thus help improve the mechanical properties. The typical structure of silane normally contains two different function groups connected by Si, as shown in Figure 2.24. In the formula, the functional group R represents a nonhydrolyzable organic group, which can be adjusted to adapt different requirements. While OR' represents a hydrolysable group such as: alkoxy or acyloxy, and sometimes halogen and amine are also used.

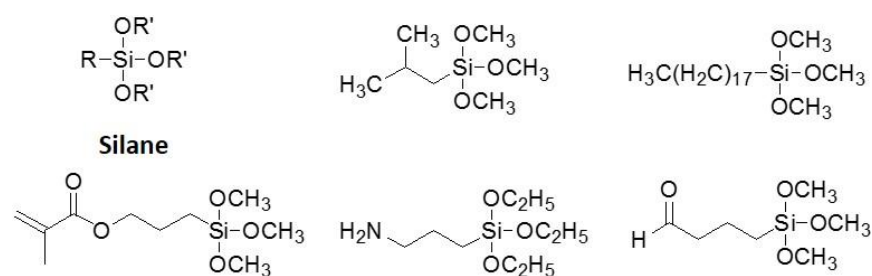


**Figure 2.24. Several commonly used silanes.**

The procedure of grafting silane to inorganic materials is illustrated in Figure 2.25. After hydrolysis and generating highly reactive silanols with the presence of water, the coupling agent forms a weak hydrogen bonding with the surface of the inorganic material. Then the following condensation process leads to a much stronger and more stable chemical bonding by removing the water. Besides of silica, the strong siloxane linkages can also be formed stably on the surface of oxides such as:  $\text{Al}_2\text{O}_3$ ,  $\text{ZrO}_2$ ,  $\text{TiO}_2$  and  $\text{NiO}$ . However, the bonding with other oxides such as:  $\text{B}_2\text{O}_3$  and  $\text{Fe}_3\text{O}_4$  would be much weaker.

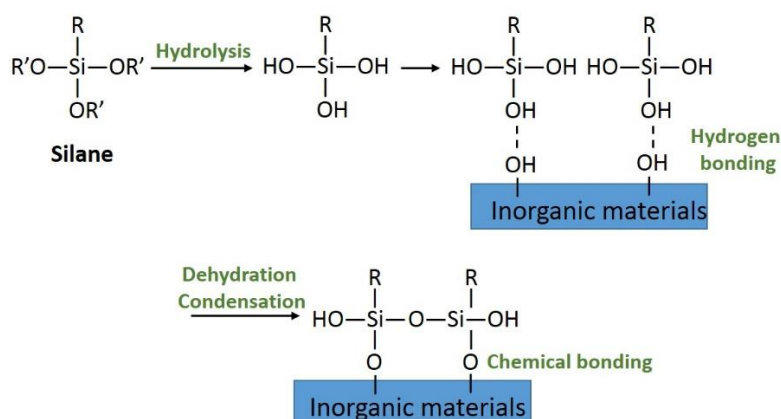


**Figure 2.25. Functional mechanism of silane coupling agent on inorganic substrate.**

Many previous researchers have successfully used silane coupling agent to improve the properties of polymer/ceramic composites.  $\gamma$ -Aminopropyltriethoxy silane was used by Dang<sup>[160]</sup> to improve the compatibility between barium titanate ( $\text{BaTiO}_3$ ) and polyvinylidene fluoride (PVDF). 3-Trimethoxysilylpropylmethacrylate (MPS) has been used to increase the bonding between hydroxyapatite and polyethylene.<sup>[161]</sup> Apart from

the positive results, there are also some negative results. Eight different functional trialkoxy silane coupling agents have been selected to study their effects on improving the interface between polypropylene and calcium carbonate ( $\text{CaCO}_3$ ).<sup>[162]</sup> Among all these silane coupling agents, only the amino functional silanes have improved the composite strength, while the others are reported to reduce the fibre surface tension, and decrease the composite strength.

#### 2.5.1.2 Titanate

Titanate is a kind of titanium-derived coupling agent that can react with inorganic surface to produce organic compatible interface or reactive organic monomolecular layers depending on requirement. The typical procedure of titanate reacting with chemical structure of titanate can be expressed as:  $(\text{Y-R-X-O})_3\text{-Ti-OR}'$ .<sup>[163]</sup> The group OR' is hydrolyzable and can react with inorganic surface to form strong chemical bonding. While the functional group on the other side of Ti could be divided into three parts as indicated above. The X could be alkylate, carboxyl, sulfonyl, phenolic, phosphate, pyrophosphate or phosphite groups. The R is normally a long carbon chain that helps improve the compatibility of the inorganic materials with the organic part. The Y is an optional part, which could either be an amino, methacrylic or acrylic group according to different needs.

Maiti<sup>[164]</sup> has used titanate as a coupling agent to improve the mechanical properties of  $\text{MgSiO}_3$  particles reinforced isotactic polypropylene composites. The introduction of the coupling agent has successfully enhanced the interface interaction between the particles and matrix. The dispersion of the particles in matrix has been improved as well, leading to an increase of Young's modulus of the final composite. Similar effects were witnessed in potassium titanate whisker reinforced polypropylene composite after surface

modification of the whiskers through tetrabutyl orthotitanate.<sup>[165]</sup> With the presence of the coupling agent, not only the dispersion, but also the mechanical properties have been enhanced, indicating improved interface between the matrix and whiskers.

### 2.5.1.3 Carboxylic acid

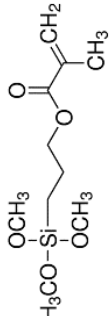
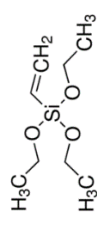
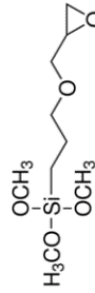
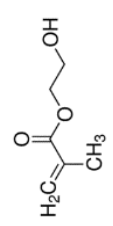
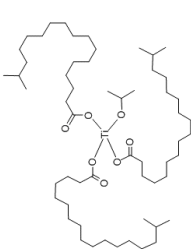
Carboxylic acid (-COOH) has used in some ceramic-polymer composites for coupling agent due to the reactive carboxyl group. Khaled<sup>[166]</sup> has used methacrylic acid to increase the bonding between PMMA and TiO<sub>2</sub>. During the experiment, the acid firstly forms a Ti-carboxylic coordination bond with the TiO<sub>2</sub> nanofibres. Then the double bond in the acid would react with methyl methacrylate (MMA) monomer, forming n-TiO<sub>2</sub>-PMMA nanocomposite. The coupling agent help increase the fibres distribution in the matrix and Young's modulus of the composite was improved. Sonoda<sup>[167]</sup> has compared the efficiencies of different carboxylic acids serving as coupling agents in barium strontium titanate-polymer composites and concluded that aliphatic carboxylic acid with longer carbon chain can give better dispersion of the ceramic particles in the polymer matrix and lead to better relative permittivity of the composite as well.

### 2.5.1.4 Other coupling agents

Besides of the coupling agents mentioned above, there're still some other materials that have been used by researchers to modify the surface properties of ceramic materials. Fe<sub>3</sub>O<sub>4</sub> particles have been modified with aryl diazonium salt 2-hydroxyethylphenyl-diazonium tetrafluoroborate (BF<sub>4</sub>, N<sub>2</sub>-C<sub>6</sub>H<sub>4</sub>-(CH<sub>2</sub>)<sub>2</sub>-OH) and the particles can dissolve in water after reaction.<sup>[168]</sup> In some other cases, more than one coupling agents will be used to achieve better results. Kamal<sup>[169]</sup> has used both carboxylic acid following titanate or silane as coupling agents to improve the properties of calcium carbonate nanoparticle filled polypropylene.



Table 2.3. Summary of some coupling agents used in polymer/ceramic system

Polymer	Filler	surfactant	Ref
Poly(methyl methacrylate) (PMMA) / Vinyl ester resin	SiO <sub>2</sub> / Al <sub>2</sub> O <sub>3</sub> / TiO <sub>2</sub> / CuO / ZrO <sub>2</sub>	3-(trimethoxysilyl)propyl methacrylate 	[170-172]
Epoxy vinyl ester resin	Al <sub>2</sub> O <sub>3</sub>	triethoxyvinylsilane 	[173]
vinyl ester / Epoxy resin / Polyimide	ceramic fibres	(3-glycidyloxypropyl)tri- methoxysilane 	[174-175]
polypropylene-graft- poly(styrene-stat-divinylbenzene)	Ba <sub>0.55</sub> Sr <sub>0.45</sub> TiO <sub>3</sub>	carboxylic acids (caproic acid, lauric acid, behenic acid and stearic acid) , lauric acid (LaA), and behenic acid	[167]
PMMA	TiO <sub>2</sub>	2-Hydroxyethyl methacrylate 	[176]
Polyethylene	Hydroxyapatite- Al <sub>2</sub> O <sub>3</sub>	Titanium triisostearyl isopropoxide 	[177-178]

In summary, suitable treatment of reinforcement in composites can enhance the reinforcement distribution in matrices and strengthen the interfacial bonding between the target materials, resulting in composites with remarkably improved mechanical properties. The choosing of the coupling agents should consider the properties of both the matrix and the reinforcement to achieve the best result.

## **2.5.2 Plasma treatment**

Ever since 1960s, plasma treatment has been used to improve the fibre surface properties in wide areas such as textiles, plastics, metallurgy and electronics industries.<sup>[179]</sup> Plasma treatment is mainly used on fibres, particles or whiskers reinforced composites to modify the physical or chemical surface properties of the reinforcement to improve the bonding between the matrix and the reinforcement without changing their bulk properties.

Though there are several different kinds of plasma treatment according to applied temperature or electrical supplement, the plasma treatment technique used to modify fibre surfaces is normally cold plasma treatment, which is usually performed in a vacuum chamber charged with a small amount particular gases flow (such as argon, or oxygen) before treatment.<sup>[180-181]</sup> Then electric power is applied to generate ionized or excited molecules and radicals to react with the surface of the present materials.<sup>[182]</sup> Plasma treatment could have both physical and chemical influence on the fibre/matrix. As for the physical aspect, the sputtering effect could increase the roughness of the fibre surface<sup>[183]</sup>, leading to increase in the contact area and the friction between the fibres and the matrix; while for the chemical aspect, the grafted active polar groups could reduce the surface energy and improve the bonding.

Derand<sup>[184]</sup> has significantly increased the bonding strength between the dental resin agent and zirconia ceramic through plasma spraying treatment with hexamethyldisiloxane. Oxygen plasma treatment<sup>[185]</sup> was used on multiwall carbon nanotubes reinforced epoxy composites and the dispersion of the nanotubes in the matrix has been improved, leading to better mechanical properties. These applications of plasma treatment in composite fabrication demonstrate this method to be an effective tool for improving mechanical properties of many composite materials.

## **2.6 Transcrystallization in fibre reinforced thermoplastic composites**

The matrices in fibre reinforced thermoplastic composites are commonly found to crystallize around the fibres under certain conditions. Due to the unique morphology of polymer growing in the direction perpendicularly to the fibre surface (see Figure 2.26), this phenomenon is then named as transcrystallinity. In this section, fundamentals about transcrystallinity, including the formation mechanism and its influence on composite mechanical properties, as well as the investigation of polycarbonate crystallization, will be briefly reviewed.

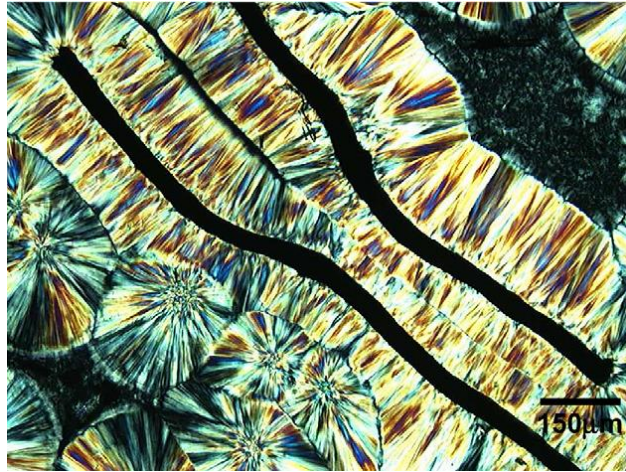


**Figure 2.26. Optical image of transcrystalline interfaces of polypropylene surrounding the carbon nanotube fibres isothermally crystallized at 125 °C.<sup>[186]</sup>**

### **2.6.1 Growth mechanism of transcrystallinity**

Transcrystallinity has been reported in systems with various polymer such as: polypropylene<sup>[187]</sup>, polyethylene, poly (phenylene sulfide), polycarbonate, and different fibres such as: carbon fibres, aramid fibres, polytetrafluoroethylene (PTFE) fibres<sup>[187]</sup>, alumina fibres<sup>[188]</sup> and glass fibres<sup>[189]</sup>. The formation of transcrystallinity is a complicated process that can be affected by a lot of different parameters related to the materials, including: the strength, modulus, surface energy, surface roughness, as well as the parameters related to the processing, such as: cooling rate, crystalline temperature and stress.<sup>[6, 17, 190]</sup>

However, opinion varies regarding to the exact cause for transcrystallinity growth. The epitaxial effect was reported as the primary mechanism for transcrystallinity formed in aramid fibre reinforced composites with polymer matrices such as poly(etherketone-ketone), poly(etherether-ketone), or poly(phenylenesulfide); while the thermal conductivity mismatch was reported as the possible reason for transcrystallinity formation in the composite having the same matrix but reinforcement with polyacrylonitrile-based

carbon or E-glass fibres.<sup>[21]</sup> Thomson<sup>[190]</sup> believed that the differences between the thermal expansion coefficients of the fibre and the matrix during solidification of the matrix from melting status could cause stress, which induced nucleation leading to transcrystallization regardless of the type of fibres and annealing temperature were used. Apart from the above possible reasons, stretching has also been reported as the cause of transcrystallinity phenomenon in polypropylene composite fibre reinforced with SiO<sub>2</sub>–MgO–CaO whiskers.<sup>[191]</sup>

Despite of various materials and processing conditions, heterogeneous nucleation of the polymer on the fibres surface is mainly accepted as the mechanism for initiation of spherulites.<sup>[192-193]</sup> The growth of the spherulites is blocked by the closely packed nuclei and forced to the direction perpendicularly to the fibre surface, leading to formation of transcrystallinity.<sup>[194]</sup> The nucleation in transcrystallinity is not only responsible for the primary nucleation of the polymer, but also the subsequent crystal growth. Therefore, the secondary nucleation of the polymer crystals is responsible for further crystal growth after primary nucleation.<sup>[190]</sup> Heterogeneous nucleation in transcrystallinity is much faster than homogeneous nucleation in pure polymers, thus the induction time of crystallinity in transcrystallinity has been notably reduced and the morphology between the fibres and matrix also has significant difference<sup>[195]</sup>.

### **2.6.2 Effects of transcrystallization on composite properties**

The interfacial layer between the fibre and the matrix plays fundamental role in fibre reinforced polymers.<sup>[188]</sup> The dramatic change in the microstructures of the interface between fibre and matrix caused by transcrystallinity could have significant impact on the composite mechanical properties.<sup>[190]</sup>

Most researchers have concluded a positive effect of the transcrystalline layer on composite mechanical properties. Wang<sup>[187]</sup> has reported that the transcrystalline layer between the fibre and the matrix helped to improve the frictional stresses, and the stress increased with the growth of the layer thickness. In carbon nanotube reinforced polypropylene composite<sup>[186]</sup>, the strength and Young's modulus of the transcrystallized polypropylene have been reported to increase significantly compared to the amorphous phase, and even the elongation to break has also been increased. Chen<sup>[21]</sup> has examined the influence of transcrystallinity on interfacial bonding between fibre and matrix for various polymer/fibre systems including three different polymer resins as well as four different types of fibres. This study shows that transcrystallinity has a positive effect on fibre-matrix interfacial bond strength, though the effect became less obvious as the fibre content increased.

Conversely, other studies have reported a negative effect of transcrystallinity on fibre reinforced composite.<sup>[17]</sup> The fibre pull-out experiment of polypropylene/flax composites showed a negative effect of the transcrystalline layer for the fibre and matrix interface<sup>[23]</sup>, though Zafeiropoulos<sup>[196]</sup> has reported a contradicting positive effect of the transcrystalline layer. The reason for the inconsistency in these two works may be caused by the different testing methods and the effect of various defects in the matrix.

Hence, different systems and conditions may cause different consequence for the effect of transcrystallinity in composite. Further investigation into the effect of transcrystallinity on the mechanical properties of different composite systems is still necessary.

### 2.6.3 Crystallization of polycarbonate

Polycarbonate is a commonly used matrix in industry due to its lightweight and excellent resistance to environmental conditions such as heat, and sunlight. The phenyl groups in polycarbonate on the main chain and the methyl side not only reduce the mobility of individual molecules, leading to relatively high viscosity, but also increase the molecular stiffness, which inhibits crystallization of polycarbonate. Thus, polycarbonate presents an extremely slow crystallization rate with a crystallization half-time of 12 days at 190 °C<sup>[197]</sup>, therefore is normally regarded as amorphous polymer. Due to the dramatic difference between properties of amorphous phase and crystallized phase, researchers has tried to investigate the mechanism and influence of polycarbonate crystallinity for further application of polycarbonate in future.

#### 2.6.3.1 Crystallization behaviour of polycarbonate

The crystallization behaviour of pure polycarbonate has been investigated by Alizadeh<sup>[198]</sup>. Differential scanning calorimetry (DSC) revealed that after the pure polycarbonate has been annealed under the 185 °C after 40-50 h, two endothermic peaks gradually appeared (see Figure 2.27). The stronger peaks around 228 °C are independent of annealing time and linked to the primary crystals, while the weaker peaks which are related to secondary crystallization shift slightly to higher temperature with increased annealing time.<sup>[199]</sup> After annealing for 680 h, the increase rate of heat of fusion becomes very slow and the degree of crystallization is close to a limitation of around 22-28% depending on the polymer molecular weight.

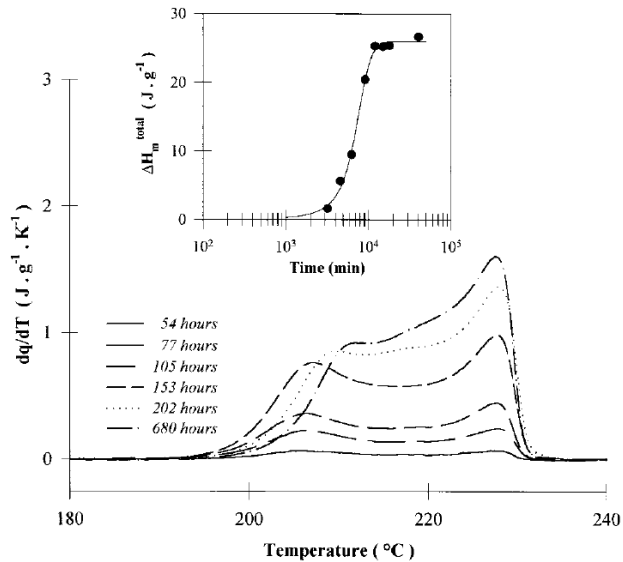


**Figure 2.27.** Heating traces of polycarbonate crystallized at 185 °C for times ranging from 54 to 680 h (heating rate = 10 °C·min<sup>-1</sup>). Inset shows the corresponding development of the total heat of fusion.<sup>[198]</sup>

Only a few reports about accelerated crystallization speed of polycarbonate in polycarbonate matrix composite despite transcrystallinity being a common phenomenon in fibre reinforced semi-crystalline polymer composites.<sup>[200-201]</sup> Takahashi<sup>[200]</sup> has reported that the crystallization rate of polycarbonate has been found significantly increased by adding vapour-grown carbon fibres (VGCF) and heat of fusion for the composite became saturated around 27 J·g<sup>-1</sup> (see Figure 2.28). Interestingly, carbon fibre can increase the crystallization of polycarbonate whereas carbon nanotubes are reported as having no effect for inducing polycarbonate crystallization<sup>[202]</sup>. The crystallization speed of polycarbonate can also be enhanced by other materials such as: graphite<sup>[203]</sup> and plasticizer tricresyl phosphate<sup>[204]</sup>. Surfactant such as alkali metal salts of organic acids, including carboxylic acids, have been reported with the ability to induce nucleating of bisphenol-A polycarbonate as well<sup>[205]</sup> but have not been applied to ceramic fibres yet.



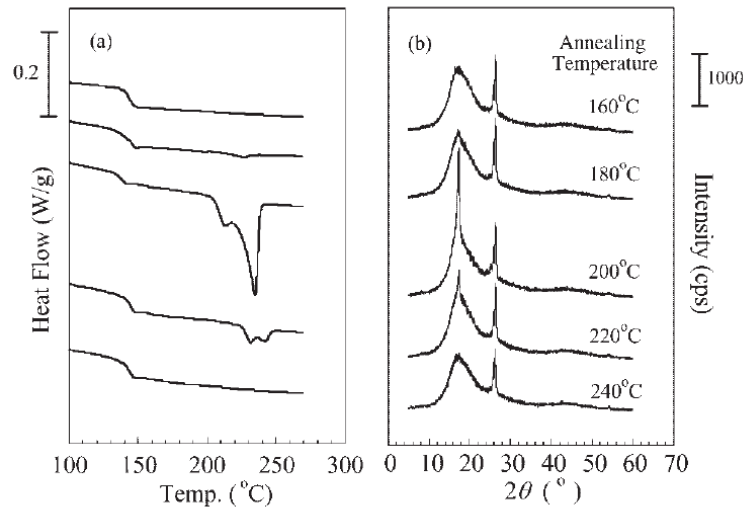


**Figure 2.28. (a) The first heating DSC (lower direction is endothermic) curves at the heating rate of 10 °C/min; (b) WAXD traces for annealed PC/VGCF™ (95:5 wt. ratio) composite at 160, 180, 200, 220 and 240 °C for 2h, respectively. [200]**

### 2.6.3.2 Mechanical properties of crystallized polycarbonate

The mechanical properties of crystallized polycarbonate have been investigated by previous researchers for future composite design and application. Both experimental and theoretical efforts have been conducted to give a more reliable result.

Polycarbonate reinforced with carbon fibres annealed at 190 °C for 3 h is reported to exhibit better Young's modulus, lower linear expansivity and greatly reduced breaking strain than composite before annealing, though there's no big difference between XRD structure analysis for both samples. [206] Brady has reported improved mechanical properties for carbon fibre reinforced polycarbonate composite with the presence of matrix crystallinity. [201] However, better adsorption is believed to be the primary reason for the improved mechanical properties rather than the interfacial crystallization, since the temperature used for annealing in this study is relatively high, which may not help to promote polycarbonate crystallization. Tensile strength of crystallized PC induced by acetone has been measured to reach 187.4 MPa by Kobayashi [207]. Scanning probe

microscopy was used by Harron<sup>[208]</sup> to investigate the crystallization of PC induced by butyl acetate vapour and explore the relationship between the growth of an individual spherulite and time. The size of the spherulite grows with time but then after around 30 min, the growth rate decreased quickly due to the impingement of neighbouring spherulites. Contrary to previous research, Harron mentioned in this work that the existence of crystals caused considerable strength loss of PC film. Therefore, further study is necessary for figuring out the exact effects of transcrystallization on polycarbonate composites reinforced with fibres.

Theoretical estimation of Young's modulus of polycarbonate has also been conducted by several researchers. Conix<sup>[204]</sup> has calculated the Young's modulus of crystallized polycarbonate following Dulmage's theory<sup>[209]</sup>, and the value is between 9.8 GPa to 19.6 GPa. Robertson<sup>[210]</sup> has predicted that the Young's modulus for crystallized polycarbonate for stretching the chain is 54 GPa and for separating a bundle of parallel chains is 1.76 GPa. Though Ward<sup>[211]</sup> argued that the theory is extremely inaccurate.

Though great efforts have been made to study the polycarbonate crystallinity behaviour, currently no consistent conclusion of the influence of crystallinity on the polycarbonate mechanical properties. For a better understanding of the polycarbonate properties and application in future work, more in-depth study is required.

## **2.7 Summary**

This chapter has reviewed the background fundamentals related to fabrication and characterization methods of alumina nanofibres as well as fibre reinforced polymer composites.

To fabricate strong ceramic reinforced polymer composite, the determining parameters for composite mechanical properties have been reviewed and strong reinforcement is summarized as the most important one. Alumina is a cheap material with high theoretical strength but relatively poor practical mechanical properties due to the presence of defects. Previous researchers have proved that mechanical properties could be improved significantly by reducing the material dimensions. Therefore, electrospinning technique could be an effective method to fabricate alumina nanofibres with enhanced properties. The parameters to control the as-spun fibre morphologies as well as the crystal structures of the calcined fibres were then reviewed for preparing alumina nanofibres with desired morphologies. Measurement of mechanical properties of individual nanofibre is very challenging due to their extremely small dimensions, thus several advanced techniques to manipulate and test these small fibres are briefly explained. Apart from the reinforcement, the fibre/matrix interface is another parameter that affect the composite greatly. The poor chemical compatibility between organic and inorganic materials could decrease the reinforcement efficiency. Hence, different surface modification methods to improve the interfacial bonding between ceramics and polymers are summarized for later selection of proper surfactant to improve the stress transfer from the matrix to the reinforcement. The reinforcement induced matrix transcrystallinity has also been reviewed since it could affect both the interfacial bonding as well as the matrix itself. The formation mechanism and the effect of the transcrystalline layer have been summarized for further investigation of the optimal condition for fabricating strong composite.

## **3 Methodology**

This chapter will summarize the fundamental methods used to fabricate and characterize the alumina nanofibres and the fibre reinforced polycarbonate composites. The fabrication methods include producing alumina nanofibres through electrospinning and solution casting of alumina nanofibre reinforced composites with polycarbonate matrix, while the characterization methods include a series of standard methods related to observation of crystal structures and morphologies, as well as measurement of mechanical and other related properties.

### **3.1 Fabrication of alumina nanofibres and polycarbonate composites reinforced with alumina nanofibres**

#### **3.1.1 Materials**

Polyacrylonitrile (PAN, average  $M_w$  150,000), aluminium 2,4-pentanedionate (AP, 99%), N,N-dimethylformamide (DMF, anhydrous, 99.8%), chloroform (anhydrous,  $\geq 99\%$ ), 3-methacryloxypropyltrimethoxysilane (MPS,  $\geq 98\%$ ), and heptane (anhydrous,  $\geq 99\%$ ) were purchased from Sigma Aldrich, UK. Polycarbonate (PC, Lexan® 161R) was purchased from SABIC, Saudi Arabia. All above materials were used as starting materials without any further purification.

### 3.1.2 Fabrication of alumina nanofibres

Electrospinning is a commonly used method to fabricate ceramic nanofibres due to the practical operation and easy controlling over the fibre properties. Here the alumina nanofibre fabrication follows a typical electrospinning methods with polymer, alumina precursor and solvent as starting materials. PAN was used as the polymer to increase the solution viscosity, AP was the alumina precursor to provide the source of aluminium ions, while DMF was the solvent. By adjusting the concentration of PAN and AP in the DMF solution, the fibre morphology can be manipulated easily.

The main procedure for fabricating alumina nanofibres were performed by the following three steps:

1. Preparation of polymer/alumina precursor solution: PAN/DMF solutions were firstly prepared by mixing PAN, DMF and a magnetic stir bar in a sealed bottle. The mixture was stirred for 4 h at 50 °C until all solid was dissolved. The solution was then stirred for another 10 min at room temperature after AP was added into the solution to obtain the PAN/AP/DMF solution for electrospinning. The colour of the final solution was light yellow.
2. Electrospinning of polymer/ alumina precursor nanofibres: A 5 ml plastic syringe filled with PAN/AP/DMF solution was connected to a 21-gauge needle through a PTFE tube (PTFE syringe tubing gauge 20, Sigma Aldrich, UK). A syringe pump (PHD 2000 Infusion, Harvard Apparatus, UK) was applied to control the feed rate. Aluminium foil was placed under the needle with the collector distance kept at 15 cm below the end of the needle. A DC power supply (Glassman PS/FC30P04.0-22, Glassman High Voltage Inc, USA), which provided a voltage up to 30 kV, was used

to generate steady DC voltage between the needle and the foil. After reaching a certain thickness, the PAN/AP nanofibre mat was peeled from the collector for further calcination.

3. Calcination: The obtained films made of PAN/AP nanofibres were placed in an alumina crucible and calcinated in a box furnace (BRF15/5, Elite Thermal Systems Limited, UK) at 1200 °C for various times with a heating rate of 5 °C·min<sup>-1</sup>. Samples were collected for further characterization after the furnace cooled to room temperature. The calcinated samples present a white film morphology made of nanofibres.

During electrospinning, various collecting methods could be used depending on the requirements for fibre arrangement. Details about collecting randomly oriented and aligned nanofibres are explained in section 4.2.1 and section 6.2.2, respectively. Sparsely distributed fibres were collected by two paralleled wood pieces, as explained in section 5.2.1.

### **3.1.3 Fabrication of polycarbonate composite reinforced with alumina nanofibres with solution casting method**

Most of the methods used to fabricate fibre reinforced composites in industry involve impregnating fibres with a polymer matrix.<sup>[212]</sup> The thermosetting polymer matrices normally have low viscosity, thus allowing flow and ease of infiltration into the fibres to form composites after curing. While the thermoplastic polymers are usually dissolved in solvent to form solution or melt if no suitable solvent is available, solution casting methods have been frequently used to fabricate composites reinforced with fibres due to their simplicity and flexibility.<sup>[213]</sup> Polycarbonate is a thermoplastic polymer with a

relatively high melting point and high viscosity after melting. Hence, a solution casting approach was used to fabricate polycarbonate matrix composite reinforced with alumina nanofibres.

As shown in Figure 3.1, the solution casting method generally involves these steps: dissolving polymer matrix in a suitable solvent with adequate concentration; place the fibres into the solution; dry the mixture to remove the solvent; apply thermal treatment with or without pressure on the film to remove stress as well as form the desired shapes. The solvent used in this method could be alcohol, water, or any organic solvent that has a relatively high volatility and no effect on the fibres.

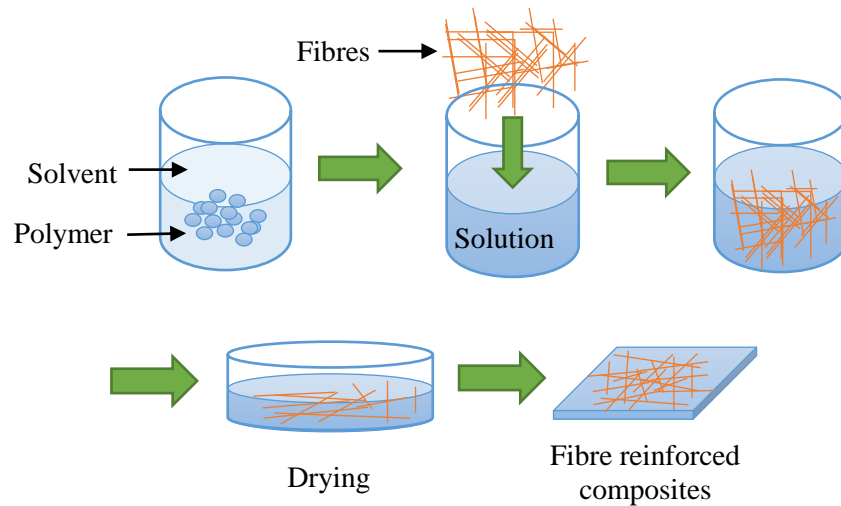


**Figure 3.1. Process of solution casting to fabricate polymer matrix composite.**

Here in this work, both randomly oriented nanofibres and aligned fibres were used to reinforce polycarbonate matrix and the solution casting methods are slightly different depending on the fibre alignment. For fabricating composite reinforced with randomly oriented alumina nanofibres, the fibres were firstly broken and dispersed in the solution of polycarbonate in chloroform, followed by stirring of the polymer/fibre solution to uniformly dispersed nanofibres. Continuous aligned nanofibres were immersed into the

polycarbonate solution overnight to allow the polymer solution to cover the porous structure of the fibre mat. After removing all the solvent and dried completely in vacuum oven at 80 °C overnight, both composites were hot pressed with a Laboratory Platen Presses (Type P 300 E, Dr. Collin GmbH, Germany) to remove voids and form a compact composite shape.

## **3.2 Imaging methods**

Electron microscopy is used here to image the resultant materials produced. Due to the limitation of the wavelength of the light, traditional optical microscopy has a maximum resolution of around 200 nm. While the wavelength of electrons beam is much smaller, leading to a resolution for electron microscopy reaching 0.1nm. This section will give a brief summary of the advanced imaging techniques used in this work.

### **3.2.1 Scanning electron microscopy imaging**

Scanning electron microscopy (SEM) has become an important research tool ever since its development in early 1950's.<sup>[214]</sup> Compared with traditional optical microscope, SEM uses electrons instead of light to capture images, thus it can provide much higher resolution owing to the shorter wavelength of the electrons than that of the visible light.

The functional elements of a typical SEM are illustrated in Figure 3.2. All SEM contain these basic parts: electron gun, anode, magnetic lenses and detector. During SEM scanning, the electron gun firstly produces a beam of electrons on the top of vacuumed chamber in the microscope. Then the electron beam will be accelerated by the anode and passes through the electromagnetic fields and lenses, which help to focus the beam down towards the sample. After the beam hits the surface of the sample, a detector will collect



the backscattered and secondary electrons ejected from the sample and convert the information to the final image. X-rays can also be produced when the beam hits the sample atoms and provides elemental information.

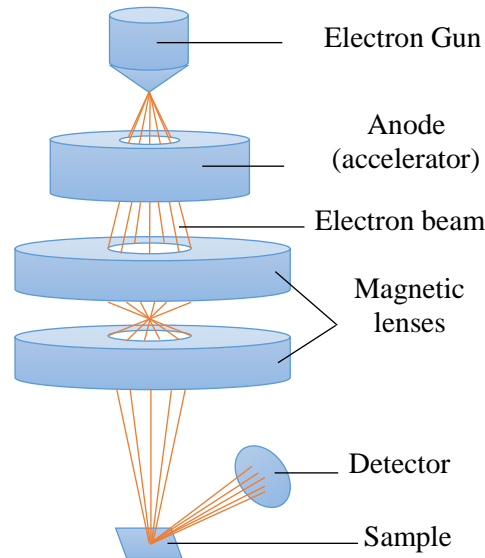


**Figure 3.2. Schematic representation of a typical scanning electron microscope setup.**

One parameter that is critical in SEM imaging operation is the accelerating voltage applied to the electrons.<sup>[215]</sup> Generally, higher accelerating voltage will produce images with better resolutions. However, too high voltage may also cause possible damage at the specimen surface, reduction in structural details in secondary electron mode, or a charging effect. Therefore, suitable accelerating voltage needs to be selected carefully for optimal imaging.

Coating the sample's surface prior to SEM imaging with a thin layer of conductive materials such as palladium (Pt) or Gold (Au) is usually necessary for samples with poor conductivity to avoid charging effect<sup>[216-217]</sup> and improve the image quality. The coating layer could also help reduce thermal damage and enhance the secondary electron signal. Carbon coating are sometimes used as an alternative to metals for X-ray microanalysis in SEM. The carbon layer is usually deposited on the sample through thermal evaporation

after the carbon source is heated to its evaporation temperature and typically is less invasive when collecting spectroscopic information.<sup>[218]</sup>

In this work, a typical SEM (FEI Inspect F, UK) was used. A thin layer of gold was coated on each sample by sputter coating (Automatic sputter coater, Agar Scientific, USA) before observing in SEM to avoid charging effect. The accelerating voltage applied on the electrons used here was kept at 10 kV and the working distance was maintained at 10 mm for all samples.

### **3.2.2 Transmission electron microscopy imaging**

Transmission electron microscopy (TEM) is another commonly used imaging method to observe materials at the micro or nano scale. Both TEM and SEM use a beam of accelerated electrons as a source of illumination. However, TEM provides images with even higher resolution and higher magnification than SEM, and TEM can also give detailed structure information, including crystal structures and specimen orientations through diffraction pattern analysis.

Despite the fundamental development in electronic circuitry of TEM through all these years, the basic elements of TEM has not changed that much comparing with the earliest generation with current modern machines. Generally, TEM normally contains five main sections regardless of the model and producer (from top to bottom, see Figure 3.3): the electron gun, the illumination system, the objective lens, the magnification and projection system and the detector.<sup>[219]</sup> After the electron gun ejects a beam of electrons, the illumination system will transfer the electrons to the sample, forming either a broad beam or focused beam.<sup>[220]</sup> All the lenses below the specimen serve to get the image of the specimen with higher magnification. The objective lenses are the most important part in

TEM, as it produces the first intermediate image and determines the quality of the final images. The intermediate lens and projector lens compose the imaging system. By changing the magnetic strength, the magnification of the final image can be adjusted ranging from hundreds to several hundred thousands of times. The detector usually refers to the viewing screen and the photographic camera. Further items include the cooling system, the vacuum system, the high voltage system as well as radiation shields.

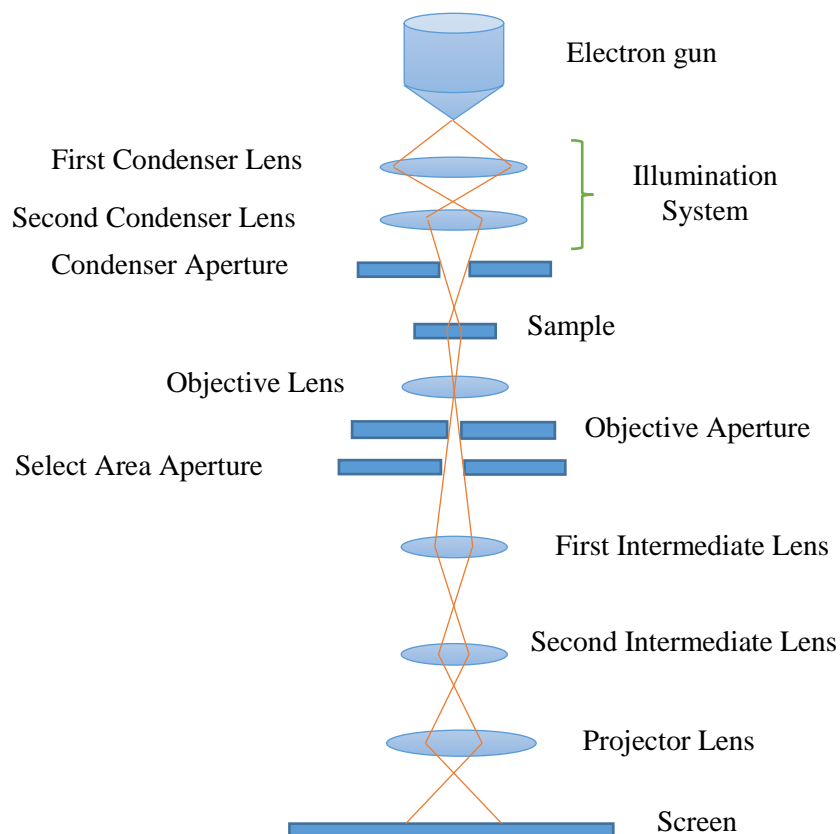


**Figure 3.3. Schematic of a typical TEM setup.**

The TEM equipment used in this work is JEOL JEM-2010 (Japan). The sample dimensions need to be relatively small to allow transmission of electrons. For observation of individual fibres in the TEM system, fibre mats after calcination were ground into small pieces and suspended in ethanol before pipetting onto a carbon-coated copper grid (Agar Scientific, UK). The sample then was ready for the observation after the ethanol evaporated completely and only fibres remained on the grid.

### 3.2.3 Atomic force microscopy imaging

Unlike SEM and TEM, atomic force microscopy (AFM) uses a physical probe instead of electrons to scan the sample surface. This method allows AFM to operate in ambient or liquid instead of the vacuum environment of electron microscopy.

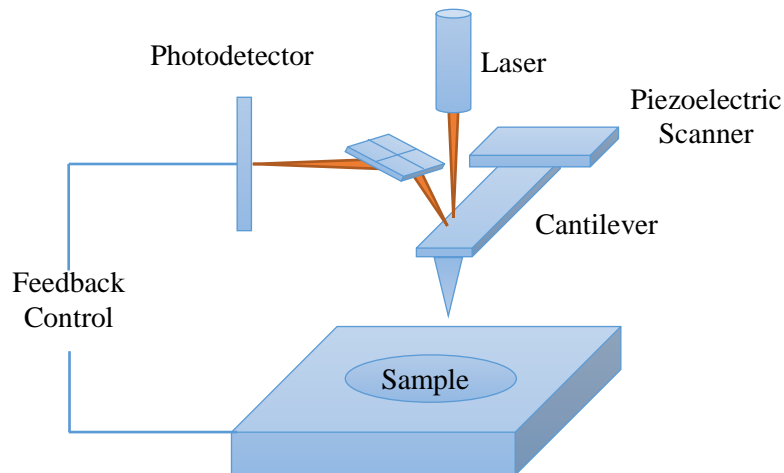


**Figure 3.4. Schematic illustration of the atomic force microscope setup.**

As illustrated in Figure 3.4, during the scanning, the AFM probe attached to the cantilever moves over the sample surface and the cantilever bends due to the atomic force between the sample and the probe. A laser is used together with a position sensitive photodetector to monitor the deflection of the cantilever. The movement of the sample stage is recorded by the feedback control system and the surface topographic image is then generated through the recording of the photodetector. Depending on the sharpness of the probe, the image scanned with AFM has a resolution between 1-20 nm.

Contact mode and tapping (semi-contact) mode are two commonly used mode while scanning with AFM. These two modes differ in terms of how the probe interactions with the sample surface. During contact mode, the probe remains in discrete contact with the surface and the force between the probe and the sample is set and controlled by the

piezoelectric scanner. This ‘hard’ contact between probe and sample therefore provides a contact pressure on the sample’s surface. Surfaces that are relatively fragile can be easily damaged or lose material removed due to contact mode imaging. Tapping mode provides an alternative option to address these problems. In tapping mode, the cantilever oscillates so that the AFM probe is in intermittent contact with the sample surface, usually at the boundary of the oscillation amplitude that can be considered the point when the cantilever will move down towards the sample in Figure 3.4. Such an oscillation ensures that the AFM probe tends to interact less with the sample surface by applying a contact pressure, as in contact mode, and can interact more through attractive van der Waals forces acting between the AFM probe and sample.

AFM is able to provide topographic information by scanning the probe in the plane of the sample and effectively recording the interactions with the sample surface. In addition, mechanical information can be provided from the interaction between the AFM probe and sample, such as through phase imaging or a nanoindentation approach. Details of how AFM can be applied to measure mechanical properties will be explained later in section 3.4.2. All these functions make AFM a powerful tool for surface analysis.

In this work, an atomic force microscopy (NT-MDT NTEGRA, Russia) with single crystal silicon cantilevers (Aspire CT300, Nanoscience instruments, USA) with a spring constant around  $40 \text{ N}\cdot\text{m}^{-1}$  were used for surface structure scanning of alumina nanofibre reinforced polycarbonate composites. Phase contrast images of the samples were provided through tapping mode to obtain improved contrast for compositions that contained differing mechanical behaviours, such as differing polymer forms.

### **3.3 Structural analysis**

Understanding the relationship between material structures and properties is important for material synthesis, fabrication and application. Since the material properties with the same chemical elements and the same molecular formula may vary due to complex molecular or atom arrangements, identifying materials with accurate structures is critical for fabricating materials with desired properties. Therefore, this section will give a brief summary for methods used for analysis of polymer and crystal structures in this experiment.

#### **3.3.1 Differential scanning calorimetry**

Differential scanning calorimetry (DSC) is one of the most widely used tools to study polymer crystallinity through studying their thermal behaviours. The basic concept of DSC is to track the change of a material's heat capacity with temperature<sup>[221]</sup>, then information of the properties such as glass transitions, and degree of crystallization of polymers can be easily interpreted from the DSC data.

The DSC equipment normally contains two pans, as illustrated in Figure 3.5. One is a sample pan, while the other one is a reference pan. During the experiment, the two pans are heated and kept at the same temperature. Due to the heat capacity of the sample pan changing due to the sample, heat flow to the sample pan will differ from that of the reference pan in order to maintain the temperature of the pans to the same value. The thermal behaviour of the sample is therefore evaluated by measuring the difference between the heat flows put on both pans.

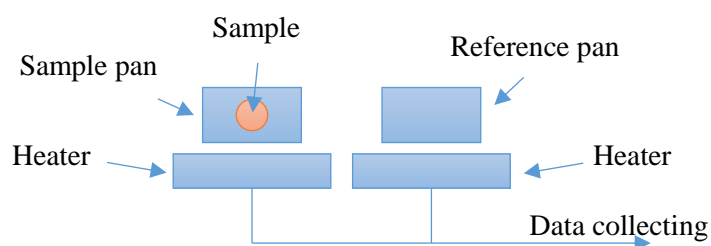


**Figure 3.5. Schematic illustration of a typical DSC setup.**

In this experiment, differential scanning calorimetry (DSC 4000, PerkinElmer, USA) was used. For preparing samples for DSC testing, 5~10 mg of each sample was weighted and put in a platinum pan. A compatible lid drilled with a hole in the middle was sealed on the pan by a crucible sealing press. The sample pan was then put into the DSC furnace with auto sample loading system for measurement. Nitrogen was used as purge gas with a flow rate of  $20 \text{ ml}\cdot\text{min}^{-1}$ . The heating rate for the measurement is  $10 \text{ }^\circ\text{C}\cdot\text{min}^{-1}$  with a range from room temperature to  $250 \text{ }^\circ\text{C}$ .

### 3.3.2 Fourier transform infrared spectroscopy

Fourier transform infrared spectroscopy (FTIR) is a practical technique to identify the presence of specific functional groups in a molecule.<sup>[222]</sup> When the infrared radiation hits the sample surface, some of the radiation will be absorbed, while some other will pass through. A wide range of spectrum is normally applied to collect high spectral resolution data. The obtained signals become the characteristic spectrum for each sample and different functional groups will show peaks at specific spectrum frequencies.

A typical FTIR instrument basically consists the following parts (as shown in Figure 3.6): an infrared light source, a beam splitter, a sliding mirror that could move back and forth, a fixed mirror and a detector.<sup>[222]</sup> When the light source reach the beam splitter, the light will be split into two beams. Half of the light would be allowed to pass through the splitter

and be reflected by the fixed mirror, while the other half will be reflected by the beam splitter and reaches a moving mirror. Both the fixed and the moving mirror would reflect the beams back to the beam splitter and the two separated beams would then converge into one again. The half beam reflected by the moving mirror would travel a constantly changing path, while the other half that reflected by the fixed mirror would have a fixed travel length. Therefore the final obtained beam would be the result of the two beams “interfering” with each other. The recombined beam would pass through the sample and the sample would absorb all the different wavelengths that differ from its characteristic spectrum, leaving the specific spectrum captured by the detector.

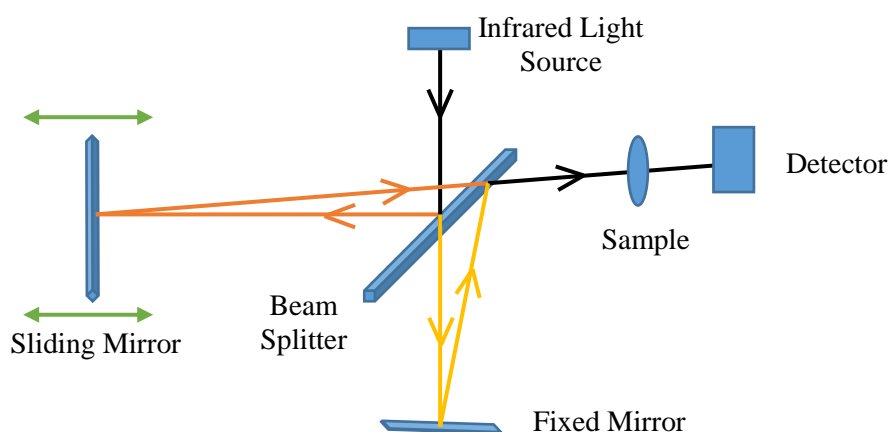


**Figure 3.6. Schematic illustration of a typical FTIR setup.**

In this work, infrared spectra of nanofibres before and after surface modification were obtained (Tensor 27, Bruker, USA) to confirm surface modification of the alumina nanofibres. Before measurement, a baseline was provided by first scanned without sample. Afterwards, each sample measurement was performed with 32 scans and  $2\text{ cm}^{-1}$  resolution within the wavenumber range of  $4000\text{--}400\text{ cm}^{-1}$ .



### 3.3.3 X-ray and electron diffraction

Diffraction is one of the most powerful methods to measure the distance between atoms in a regular material structure and can be used to identify the crystal structures of different materials. In a typical diffraction experiment, the surface of the sample is evaluated by an incident wave and the outgoing directions and intensities of the diffracted waves are recorded by a detector. Diffraction requires discrete wavelengths of the incident wave that correlate with distance between the atoms. Therefore incident radiation with appropriate wavelengths from X-ray, electron and neutron are commonly used to provide diffraction. Despite the different physical mechanisms between these three waves, all follow conditions defined by Bragg's law. In this section, the basic theory of Bragg's law as well as the fundamentals of X-ray diffraction and electron diffraction will be briefly explained.

#### 3.3.3.1 Bragg's law

Bragg's law is the most important equation of explaining why the X-ray or electron beams can be reflected at certain angles of incidence while going through the crystal lattices. As illustrated in Figure 3.7, after the beam pass through the lattice, the difference in the path length between the path length of beam 1 and 2 is  $2d \cdot \sin\theta$  (as indicated with orange lines). Since constructive interference would occur when the path length difference equals to the wavelength of the beam, Bragg's law can then be expressed as:

$$n \cdot \lambda = 2d \cdot \sin\theta \quad (3-1)$$

Where  $n$  is an integer constant,  $\lambda$  is the wavelength of the electron beam,  $d$  is the distance between the crystal lattices, and  $\theta$  is the incident angle of the electron beam. Therefore, for diffraction experiment, the wavelength of the beams need to be comparable to the lattice spacing of the crystals.

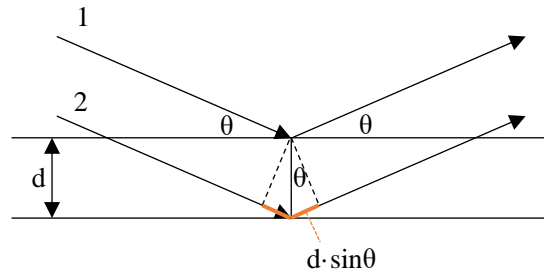


**Figure 3.7. Schematic illustration of Bragg's law.**

The diffraction pattern normally consists many distinct peaks with different intensities, which are corresponding to different interplanar spacings,  $d$ . Take cubic crystals with the lattice parameter of  $a_0$  as example, for the plane marked as  $(hkl)$  by the Miller indices, the interplanar spacing can be expressed as:

$$d_{hkl} = \frac{a_0}{\sqrt{h^2 + k^2 + l^2}} \quad (3-2)$$

The relationship between the interplanar spacing and the lattice parameters varies depending on the crystal structures. The details of this relationship are found in literature<sup>[223]</sup>.

Bragg's law describes the relationship between the wavelength and the crystal structures, therefore this theory can then be used to determine the wavelength of a certain beam with a known crystal structure, or determine the crystal structure with a known wavelength. Both electron diffraction (ED) and X-ray diffraction (XRD) follow Bragg's law for interpreting the diffraction patterns, but the wavelength of electron is much shorter than that of X-rays and the incident angle of ED is with  $2^\circ$  while that for XRD ranging from  $0^\circ$  to  $180^\circ$ .

### 3.3.3.2 X-ray diffraction

X-ray is a form of electromagnetic radiation with a wavelength between 0.01 Å to 100 Å and energy ranging from 100 eV to 100 keV. Since the wavelength of the radiation needs to be comparable to the distance between atoms<sup>[224]</sup>, only X-rays with wavelength ranging from a few Å to 0.1 Å are used.

A typical XRD setup normally consists of an X-ray tube, a sample holder and an X-ray detector, as illustrated in Figure 3.8. After being emitted from the X-ray source, the X-ray beam will hit the material and interact with the electron cloud around the atoms. The electrons will then oscillate with a frequency the same as the radiation, forming interference. For most directions the interference is destructive, except for some directions that will have constructive interference due to the regularly arranged atoms. Thus, the diffracted beam actually consists a large quantity of scattered rays that interfere with each other. The reflected X-rays will be recorded when the sample and the detector are rotated. When the Bragg's law is satisfied and constructive interference happens, the detector will record the signal and transform all the signals to the final figure. Owing to the interference between the diffracted waves from each atoms, the resultant diffracted waves could have very strong peaks if the materials have periodic arrangement (such as crystals).

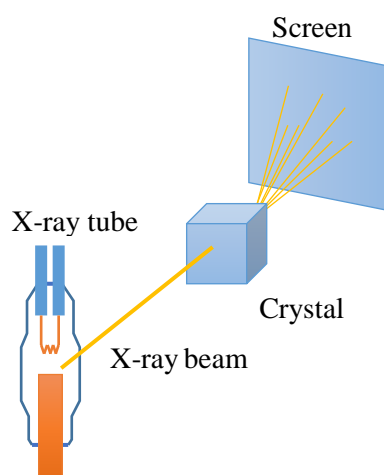


**Figure 3.8. Schematic illustration of a typical XRD setup.**

Among several different kinds of XRD techniques, the most widely used one might be the powder XRD. The sample prepared for this measurement usually has a powdery form, meaning that randomly oriented crystals exist in the sample. The recorded 2-D pattern of powder XRD usually shows a series of concentric rings with various diameters, which are corresponding to various specific interplanar spacing of the crystals. After comparing the peaks with the standard PDF card, the material then can be identified. This technique can be used to characterize the crystalline materials, measure the sample purity or determine the unit cell dimensions.

Here, alumina nanofibre mats calcinated at 1200 °C for different times were scanned with X-ray diffraction (PANalytical X'Pert PRO, Netherlands) using Cu K-alpha ( $\lambda=0.15418$  nm) radiation. The obtained intensities of the diffraction peaks at different scanning degrees will be arranged into the XRD pattern and compared with standard pattern to identify the correct crystal structures.

### 3.3.3.3 Electron diffraction

Louis de Broglie proposed the theory that the electrons could present both particle and wave properties, therefore the wavelength of an electron wave  $\lambda$  could be expressed similar to the photon wave as:

$$\lambda = \frac{h}{p} = \frac{h}{\sqrt{2mE}} \quad (3-3)$$

Where  $h$  is the Planck's constant,  $E$  is the kinetic energy of the particle in the non-relativistic limit,  $p$  and  $m$  are the momentum and the mass of the electron, respectively. The wave properties of the electrons in Louis de Broglie's theory have already been confirmed<sup>[225]</sup>, thus if the electron beam hit the surface of a substrate, they will interact with the electric cloud around the atoms through Coulomb forces and generate an electron wave function, which follows the Bragg's law. The small wavelength of the electron waves match with the atomic lattice, therefore electron diffraction (ED) were used frequently to examine the crystal structures of ceramic materials.

ED is normally performed in a TEM with the same structure as illustrated in Figure 3.3. When the electron beam hits the material surface, a diffraction pattern will be formed and the resultant diffraction pattern can be observed both directly on a fluorescent screen and recorded through a CCD camera. The electron diffraction exhibits quite a few advantages compared to the X-ray diffraction. Firstly, the electron diffraction pattern can be observed directly on the screen due to the high energy of the diffracted electron beams. Thus, the changing of the diffraction pattern can also be viewed simultaneously while tilting the viewing angles of the crystals. Additionally, the electron diffraction pattern can be obtained in a small area of the sample selected with a diffracted aperture, so the pattern obtained from areas can be easily compared. Despite of the above advantages, multiple

scattering could happen in ED due to the strong interaction of the electron waves and the atoms, therefore making the crystal structures interpretation more difficult.

Here, the individual alumina nanofibres or nanofibre mat produced by varying calcination conditions were investigated with ED in TEM. The ED patterns of the fibres were then carefully interpreted into the corresponding crystal structures and labelled with Miller indices. The obtained information of the fibre crystal structures were then used together with the X-ray diffraction patterns to study the growth mechanism and the crystal structure transformation of the alumina nanofibres.

### **3.4 Mechanical testing**

The mechanical properties of the produced materials is a critical aim of this work, especially as achieving the theoretical mechanical properties of alumina would exceed those of many typical engineering materials. Hence, appropriate techniques for measuring the mechanical properties of individual fibres as well as the composites are required. In this section, various methods to measure the mechanical properties of both individual nanofibres and composites will be briefly introduced.

#### **3.4.1 Combined AFM-SEM system for nanotensile testing of individual alumina nanofibres**

Though mechanical properties of fibres with diameter around 10  $\mu\text{m}$  can be tested easily using conventional tensile testing equipment<sup>[226]</sup>, these methods are not suitable for evaluating fibres with further reduced diameters. Therefore, combining both AFM and SEM was used here to measure the tensile strength of individual nanofibres with an extremely small diameter more accurately and directly. The small scale of an AFM probe

matches the dimension of the nanofibres thus allowing manipulation of single fibres. This combined AFM/SEM system is an effective tool for small scale tensile testing.

As shown in Figure 3.9, the setup for a combined AFM/SEM system generally comprises a movable positioner, an AFM head and a piezo scanner. The equipment is then fixed in a conventional SEM chamber for observation. An AFM probe sits on the AFM head. The positioner controls the moving of the sample stage to the proper position for the AFM probe to pick the individual nanofibre from the sample. The piezo scanner and fibre optics are used to record the bending of the AFM probe, thus obtaining the force applied on the fibre.

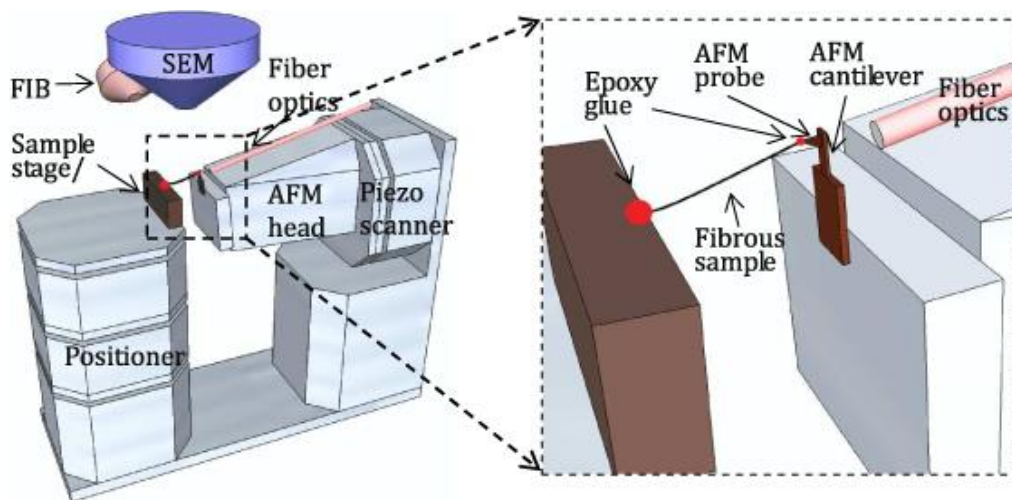


**Figure 3.9. Schematic illustration of the in situ configuration of tensile testing of a nanofibrous sample with a combination of AFM-SEM.<sup>[141]</sup>**

To measure the fibre strain, a calibration of the AFM probe fixed directly on the sample stage is required and the calculation details have been explained previously.<sup>[141]</sup> Tensile testing by combining AFM and SEM is generally performed by fixing one end of the fibre to the AFM probe by glue and the other fibre end into a glue droplet, as shown in Figure 3.10. After the glue cures, the AFM probe is moved away from the glue drop and causes tensile deformation of the nanofibre between the probe and glue droplet until failure (see

Figure 3.10d). AFM cantilever bending during this tensile test allows determination of the force acting on the single nanofibre. The limitation with the AFM/SEM system is the relatively long time required to carry out each test due to the difficulty in manipulating small fibres with the AFM probe.<sup>[135, 227]</sup>

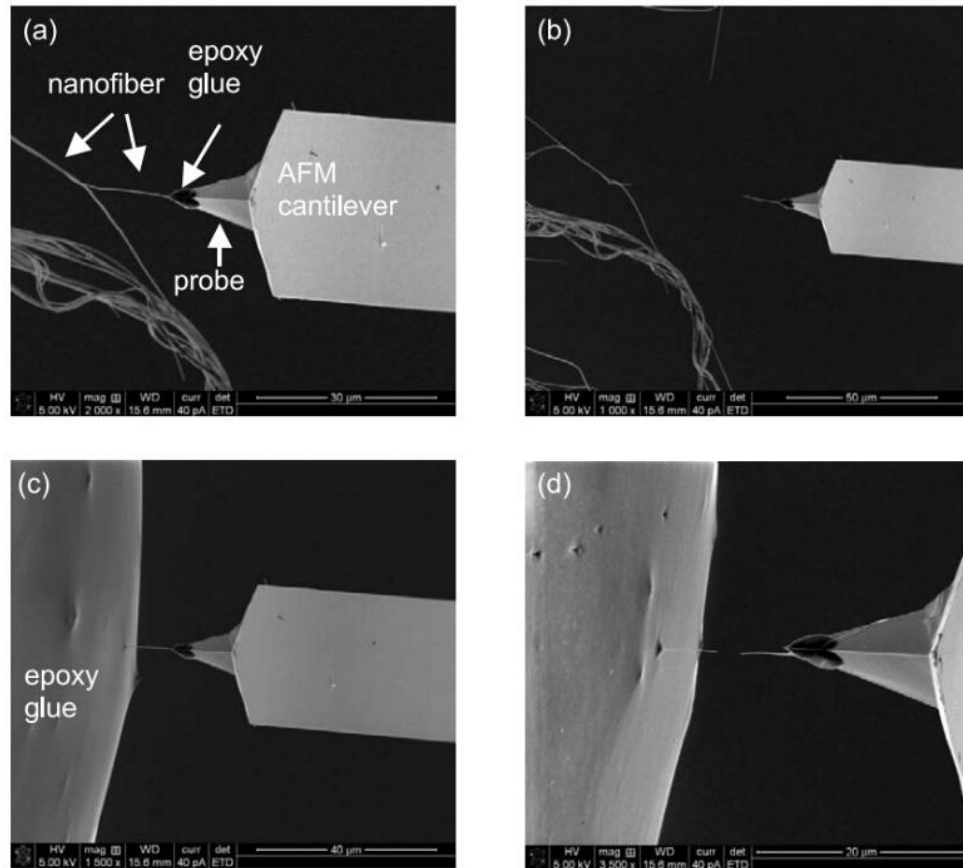


**Figure 3.10. SEM image showing a typical tensile testing procedure of electrospun nanofibres with AFM/SEM system: (a) AFM contacts one end of the fibre with glue on the probe; (b) AFM probe moves away with the fibre fixed to the probe apex; (c) AFM probe moves towards a glue drop and allow the other end of the fibre contacts the glue; (d) Curing of the glue and translation of the AFM probe/probe away from the glue drop provides tensile deformation until failure.<sup>[141]</sup>**

A custom-built atomic force microscope (AFM, attocube systems AG, Germany) and scanning electron microscope (SEM, FEI Quanta, USA) combined system was used here



to test the tensile strength of individual alumina nanofibres. Spring constant of the AFM cantilevers (Aspire CT300, Nanoscience instruments, USA) were calibrated in a conventional AFM equipment (NT-MDT NTEGRA, Russia) before each testing. The individual nanofibres were tested by first fixing the fibre mat onto a TEM lift-out grid (Omniprobe, Agar Scientific, UK) using a special SEM-compatible glue (Kleindiek Nanotechnik GmbH, Germany). The fibre mat was then placed within the AFM/SEM system and the steps shown in Figure 3.10 followed. The force required to break the fibre was recorded through the bending distance of the cantilever and used to calculate the fibre strength together with the accurate fibre diameters measured through TEM.

### **3.4.2 AFM Nanoindentation**

AFM nanoindentation is a useful tool for measuring elastic properties and hardness of materials, especially in a nanoscale. The fundamental theory of AFM nanoindentation is the same as shown in section 3.2.3. However, the nanoindentation process need to be explained further.

The whole process for AFM nanoindentation is schematically illustrated in Figure 3.11. Firstly, the AFM probe approaches the sample surface gradually. In position 1, the probe is still far away from the sample and no force between the probe and the sample can be identified. As the probe moves closer to position 2, the force between the sample and the probe increases and the probe bends under force, as shown in position 3. When the probe starts to withdraw from position 4, the force that the probe bear changes from pushing to pulling. At position 5, the probe probe detaches from the sample suddenly and a sharp force change is witnessed. As the probe withdraws further, the cantilever returns to the original status in position 6. The obtained curve of voltage output versus the piezoelectric actuator displacement is recorded during the whole experiment and will then be

transformed into a typical force-displacement curve, which can be used to calculate the sample's Young's modulus later. Prior to measurement, the spring constant need to be calibrated to obtain accurate results.

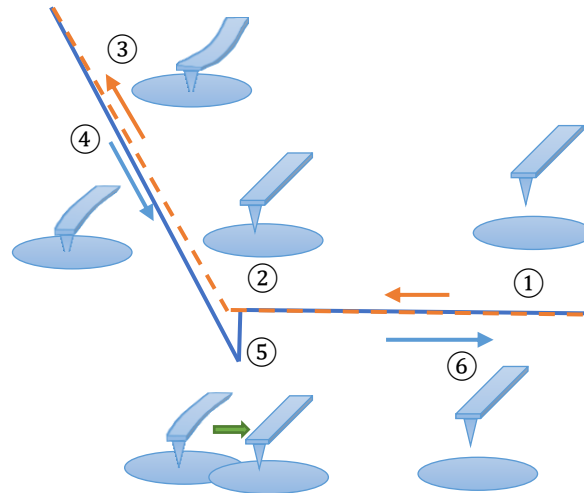


**Figure 3.11. Schematic illustration of AFM nanoindentation. X axis is the piezoelectric actuator displacement, while y axis is the voltage output.**

An atomic force microscope (AFM, NT-MDT NTEGRA, Russia) with single crystal silicon cantilevers (Aspire CT300, Nanoscience instruments, USA) was used for AFM nanoindentation in this work. The spring constant of the probes used here were around  $40 \text{ N}\cdot\text{m}^{-1}$  and were calibrated with the normal noise methods<sup>[228]</sup> before each nanoindentation testing for later force calculation. After surface scanning, the nanoindentation was performed with piercing the head of the AFM probe into the sample surface. During the nanoindentation test, the AFM probe movement was accurately controlled by a piezoelectric actuator and the bending of the cantilever was recorded by a position sensitive photo-diode<sup>[229]</sup> together with the z-piezo positioner displacement. After the testing, the conversion from photodiode current (nA) to cantilever deflection (nm) was calibrated and determined using a sapphire sheet, assuming that the sheet only displays a

purely elastic response. The unloading curves showing retracing of the probe were used to calculate the elastic properties based on the Hertzian model<sup>[230-231]</sup>.

### 3.4.3 Micro-tensile testing

Tensile testing has been widely used to determine mechanical properties of the materials including: Young's modulus, tensile strength and ultimate strain. In a typical tensile testing, a sample with a “dog-bone” shape is hold between a fixed and a movable head as shown in Figure 3.12. During the experiment, the movable head will pull the sample until the material fails. The force and moving distance applied on the head will be recorded simultaneously and translated into the stress and strain information later.

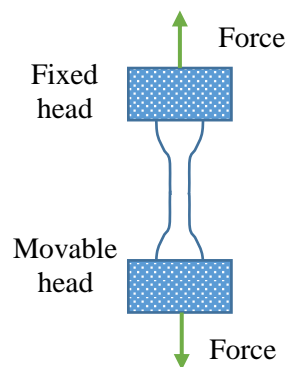


**Figure 3.12. Illustration of a conventional tensile testing setup.**

The stress strain curves of alumina nanofibre reinforced polycarbonate composites were obtained with a tensile stage with the maximum pulling force reaching 200 N (Microtest 200N tensile stage, Deben, UK). After using hot press (Laboratory Platen Presses Type P 300 E, Dr. Collin GmbH, Germany) with a heating temperature of 250 °C to form a regular flat film, the composite was cut into a rectangle shape (0.07 mm × 1.5 mm × 15 mm) and fixed between two stages. The samples were then stretched at a rate of 0.2 mm·min<sup>-1</sup> until the composite failed. The force-distance curves were recorded and

transferred to stress-strain curve after measurement of the accurate dimensions of the sample with an optimal microscope (BX51, Olympus Microscopes, Japan) for later calculation of the composite porosities.

## 3.5 Other methods

### 3.5.1 Specific surface area

Brunauer-Emmet-Teller (BET) theory is one of the commonly used methods to determine the specific surface area and porosity. The BET theory extended the Langmuir theory, which describes the monolayer molecular adsorption of gas, to a multi-layer physisorption adsorption. The BET equation can be expressed as:

$$\frac{1}{v \left( \frac{P_0}{P} - 1 \right)} = \frac{c-1}{v_m \cdot c} \cdot \frac{P_0}{P} + \frac{1}{v_m \cdot c} \quad (3-4)$$

$$c = \exp \left( \frac{E_1 - E_2}{RT} \right) \quad (3-5)$$

where,  $P$  is the partial pressure of the adsorbate gas in equilibrium at the temperature of adsorption,  $P_0$  is the saturation pressure for the same condition,  $v$  is the quantity of the adsorbed gas at standard temperature and pressure (STP), and  $v_m$  is the monolayer adsorbed gas quantity at STP,  $c$  is the BET constant,  $E_1$  is the heat of adsorption for the first layer and  $E_2$  is that for the second and higher layers and is equal to the heat of liquefaction.

For multipoint measurement,  $\frac{1}{v(P_0/P)}$  is plotted against  $P_0/P$ , and the relationship is expressed by a straight line according to equation (3-4) to calculate  $c$  and  $v_m$ . The

approximate relative pressure should be kept in the range between 0.05 and 0.3. The specific surface area  $S_{BET}$  can then be calculated by the equation:

$$S_{BET} = \frac{v_m \cdot N \cdot s}{V \cdot m} \quad (3-6)$$

Where  $N$  is the Avogadro constant ( $6.022 \times 10^{23} \text{ mol}^{-1}$ ),  $V$  is the molar volume of adsorbent gas,  $s$  is the cross-sectional area of one adsorbate molecule, and  $m$  is the mass of the total material.

Specific surface areas of the alumina nanofibre mats calcinated under different heating procedures were measured by Surface Area Analyzer (Gemini VII 2390, Micromeritics Instrument Corporation, USA) according to the BET theory. Before measurement, the nanofibre mats were heated at 200 °C in nitrogen atmosphere overnight. Then the experiment were conducted at 77.15 K under vacuum. The vacuum rate was 300 mmHg·min<sup>-1</sup> and the vacuum time was 6 min. The total measurement time for each sample was around 1 h.

### 3.5.2 Porosity

A pycnometer is generally used to measure the accurate volume and density of solid materials based on the hypotheses that the gas behaves ideally in pycnometer and the temperature are constant during testing. After measuring the apparent volume, the composites porosity can then be calculated with the actual material volume measured by the gas pycnometer.

The basic theory of pycnometer is to measure the pressure change caused by the displacement of the solid sample. As shown in Figure 3.13, a gas pycnometer normally contains two chambers: a sample chamber (with a removable lid), and a reference

chamber with fixed inner volume. The volume of the reference chamber need to be calibrated prior to the measurement. The transducer is used to measure the absolute gas pressure. Before measuring the accurate solid volume with pycnometer, a baseline is built firstly by expanding a quantity of gas of known pressure into the empty sample chamber. After the samples being placed into the chamber, the chamber would be resealed again and purged into the same quantity of gas at the same pressure. The change of gas pressure caused by the volume occupied by the solid will be recorded. The pressure difference between the baseline and the one with sample will be applied to calculate the true volume of the solid.

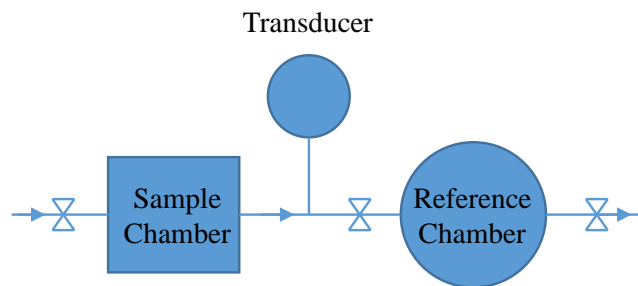


**Figure 3.13. Schematic illustration of gas pycnometer.**

Gas pycnometer (AccuPyc 1330, Micromeritics Instrument Corporation, USA) using a supply of helium gas has been applied to confirm the porosity of the composite in this work. The composites after hot pressing generally have a regular film shape with constant depth. After being dried at 80 °C under vacuum overnight, the samples were measured with the gas pycnometer to obtain the actual solid volume. The apparent volume can then be calculated after measuring the area of the film with an open source scientific tool ImageJ (NIH, USA). By dividing the actual volume with the apparent volume, porosity of the composite can then be calculated.

## 3.6 Summary

This chapter has summarized typical standard methods for fabricating nanofibres as well as polycarbonate reinforced composites. Alumina nanofibres were fabricated through electrospinning following by calcination, and the resultant alumina nanofibre mats were then fabricated into composites with polycarbonate through solution casting methods.

Different characterization methods involved in this work to valuate various properties of both individual nanofibres and composites have also been listed and explained. SEM, TEM and AFM were used to observe the fibre and composite morphologies. The fibre crystal structures were characterized by both XRD and ED. BET was used to measure the specific surface area of the fibre mats. The thermal behaviour and porosity of the composites were studied by DSC and gas pycnometer, respectively. The mechanical properties of the samples were measured through nanotensile testing, AFM nanoindentation as well as micro tensile testing.

# 4 Alumina nanofibre fabrication and fibre growth mechanism

## 4.1 Introduction

Alumina nanofibres were first fabricated using electrospinning over a decade ago and have prompted additional work due to the availability of the base materials. [67, 69, 71-72, 80]

A calcination step required to give alumina nanofibres is generally identified as critical in defining both the grain size but also the crystal structure, leading to significant changes in resultant mechanical properties. Increasing calcination temperature produces typical alumina transformation from: amorphous alumina  $\rightarrow$   $\gamma$ -alumina (cubic,  $Fd\bar{3}m$ , No. 227)  $\rightarrow$   $\delta$ -alumina (tetragonal,  $P\bar{4}m2$ , No. 115),  $\delta$ -alumina (orthorhombic,  $P222$ , No. 16),  $\theta$ -alumina (monoclinic,  $A2/m$ , No. 12)  $\rightarrow$   $\alpha$ -alumina (rhombohedral,  $R\bar{3}c$ , No. 167), and the intermediate state varies depending on the starting materials.<sup>[78]</sup> Alumina nanofibres fabricated by previous researchers are reported to experience the transformation from polycrystalline  $\gamma$  alumina to single crystal  $\alpha$  alumina fibres after adequate calcination time and temperature through the formation of elongated  $\alpha$ -alumina colonies.<sup>[80]</sup>

However, though many studies indicate a transformation from  $\gamma$  alumina to  $\alpha$  phase, the formation of these  $\alpha$ -alumina colonies and the mechanism for fibre growth direction



needed to develop high strength nanofibres are not clearly identified.<sup>[76, 92, 232]</sup> Single crystal structures are usually considered free from defects associated with grain boundaries, making the strength of nanofibres less dependent on fibre diameters. To thoroughly investigate the dependence of tensile strength on fibre dimensions and crystal structures, the strength of both polycrystalline and single crystal alumina nanofibres are systematically measured and compared.

Here in this work, ultra-strong continuous alumina nanofibres are fabricated using electrospinning and post-calcination methods. The effects of electrospinning solution concentrations on the as-spun fibre diameters are investigated. The transformation mechanism of alumina nanofibre from polycrystalline  $\gamma$  phase to single crystal  $\alpha$  phase is investigated thoroughly by manipulating the calcination parameters followed by morphology observation and crystal structure analysis through transmission electron microscopy and electron diffraction.

## **4.2 Materials and methods**

### **4.2.1 Sample preparation**

Electrospinning with solution made of polyacrylonitrile (PAN), aluminium 2,4-pentanedionate (AP) dissolved in N,N-dimethylformamide (DMF) was used to prepare alumina nanofibre mat. Here, the concentration of PAN in the solution ranges from 7% to 10% and different amount of AP ranging from 33.3 wt% to 106 wt% of PAN were used to study their influence on the fibre morphologies. The electrospinning equipment and procedures were used following section 3.1.2. The feed rate of the PAN/AP/DMF solution was set at  $0.6 \text{ mL}\cdot\text{h}^{-1}$ . The whole process was conducted at room temperature in

air with a humidity of around 10-40%. The as-spun PAN/AP nanofibre mats were removed from the aluminium foil after electrospinning for 2 hours. The obtained film made up of PAN/AP nanofibres was placed in an alumina crucible and calcinated at 1200 °C for several hours ranging from 0 h to 8 h with a heating rate of 5 °C·min<sup>-1</sup>. After the furnace cooled naturally to room temperature, the sample would be collected for further characterization.

## **4.2.2 Characterization of morphology of alumina nanofibres**

### 4.2.2.1 Morphology observation

The microstructures of the nanofibres were examined by both scanning electron microscopy (SEM) and transmission electron microscopy (TEM). Prior to observation in SEM, the calcinated alumina nanofibre mat were coated with a thin layer of gold to avoid charging effects. To prepare TEM samples, calcinated samples were ground into small pieces and suspended in ethanol before pipetting onto a carbon-coated copper grid for TEM examination.

### 4.2.2.2 Fibre diameter distributions

SEM was used to measure the diameter distribution of electrospun nanofibres as well as nanofibres calcinated under different conditions. More than 50 diameters of nanofibres randomly chosen from the same sample were measured and the numbers of fibres in different diameter ranges were counted. Normal distribution was fitted afterwards to calculate the average diameter of the fibre mat.

#### 4.2.2.3 Crystal structure characterization

Both Electron diffraction (ED) and X-ray diffraction were used in this work to study the crystal structure development of the alumina nanofibres. ED patterns of individual nanofibres calcinated under different heating procedures were observed in TEM equipment to examine the fibre structures. X-ray diffraction (XRD) were detected using Cu Ka ( $\lambda=0.15418$  nm) radiation.

#### 4.2.2.4 Specific surface area measurement

Specific surface areas of the fibre mats calcinated with different calcination procedures were measured by Surface Area Analyzer according to the BET theory. Before measurement, the fibre mats were heated at 200 °C in nitrogen atmosphere. Then the experiment was conducted under 77.15 K and the total measurement time for each sample was around 1 h.

### **4.3 Results and Discussion**

#### **4.3.1 Effect of concentrations of PAN and AP on fibre morphologies**

The concentrations of the polymer and ceramic precursors have great impact on the morphology of the final fibres. Previous work done by Gu<sup>[233]</sup> and Wang<sup>[234]</sup> have proved that the concentration of PAN has a significant impact on the diameter of electrospun nanofibres. Higher concentration of PAN in DMF would increase the viscosity of the solution and give rise to larger fibre diameters. However, the role of ceramic precursor in controlling the diameter of the fibres has rarely been revealed in work done before. In this

section, the effect of both the polymer and ceramic precursor concentrations on the fibre morphologies would be investigated.

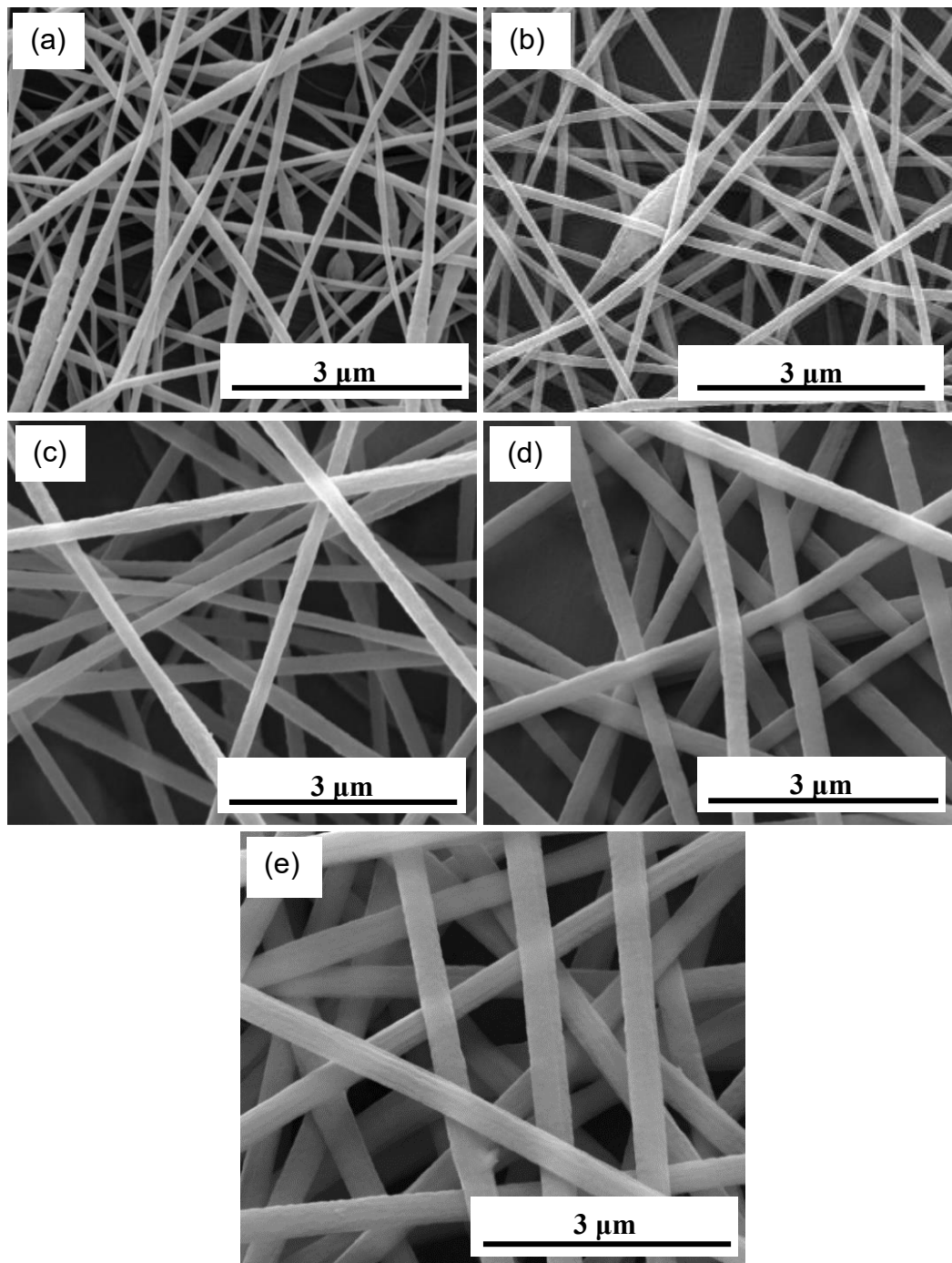


**Figure 4.1.** Scanning electron microscopy images of electrospun PAN/AP nanofibres with different concentrations of PAN in PAN/DMF solution: (a) 6 wt%, (b) 7 wt%, (c) 8 wt%, (d) 9 wt% and (e) 10 wt%. For all these solutions, the ratio between PAN weight percentage and AP weight percentage is fixed at 3.

The changing of morphologies of PAN/AP nanofibres with increased concentration of PAN and AP are shown in Figure 4.1. Here, the ratio between PAN weight percentage and AP weight percentage in all solutions were fixed at 3. When the concentration of PAN (before AP was added) is 6 wt%, the viscosity of the solution for electrospinning is relatively low and the fibre diameters is not uniform. Many beads are observed while electrospinning PAN/AP/DMF solution with the lowest PAN/AP concentration (see Figure 4.1a). The nanofibres become smoother and the diameters are more even as the concentration of PAN and AP increases gradually. The rate of fibre diameter growth is faster and steadier after the fibres were uniform.

The diameter distributions of PAN/AP fibre diameters fabricated from different solution concentrations were shown in Figure 4.2. The marked legends in Figure 4.2 represent the weight of percentage of PAN in PAN/DMF solution before AP was added. The diameters of as-spun PAN/AP nanofibres with different AP concentrations are shown in Figure 4.3. For all the solutions with different AP concentrations, the concentration of PAN in solution before AP was added was fixed at 10 wt%. The as-spun nanofibre diameters for all samples show typical normal distributions. The fibre diameter increases significantly with the increased concentration of AP, as shown in Figure 4.3e. This increase of diameters could be attributed to the increased solution viscosity. The diameter of the fibres variation increased when more amount of AP was added.

Understanding the effect of concentrations of polymer and aluminium precursor helps to control the fibre diameters in desired ranges. These results lay a foundation for later exploring the relationship between the strength and the fibre diameters.

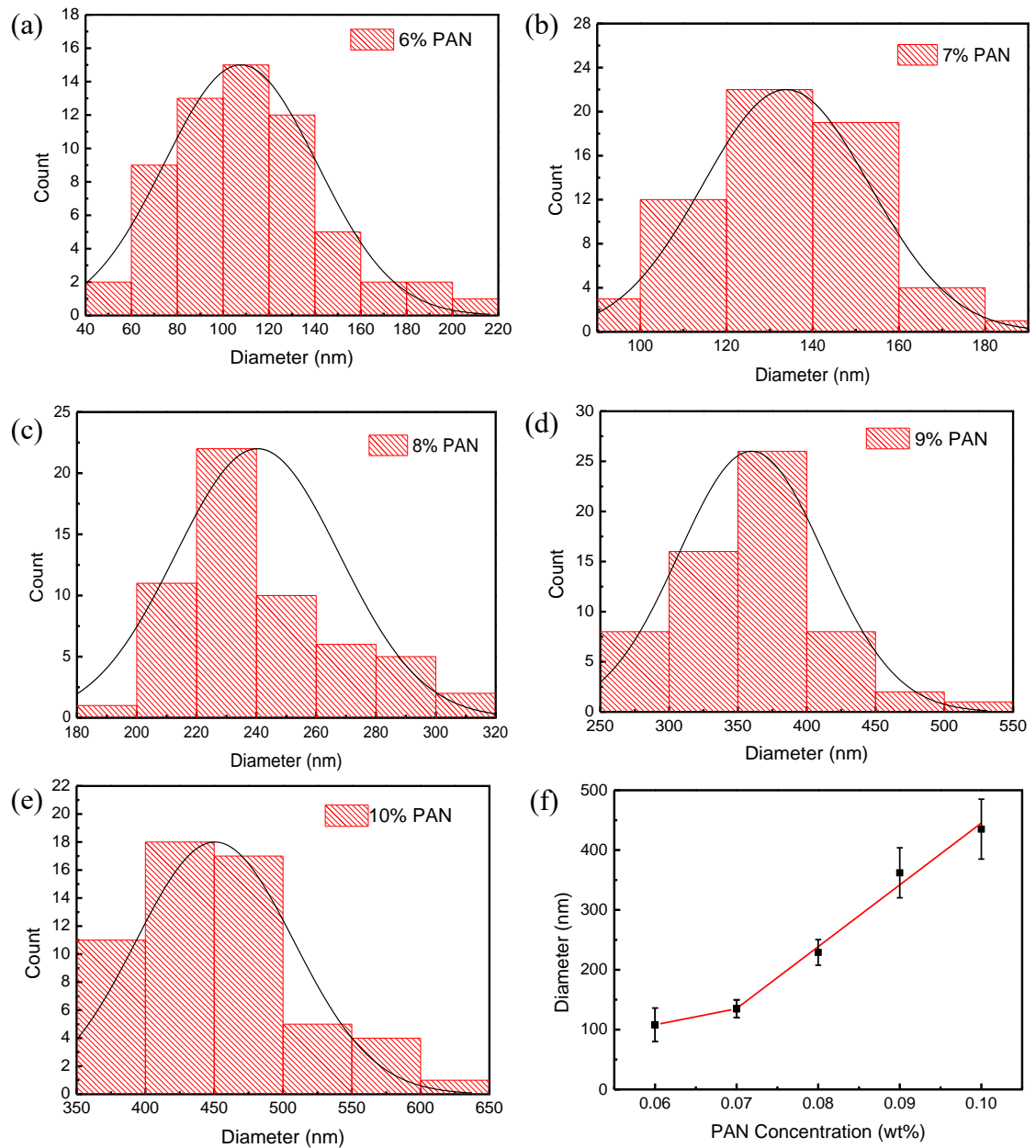


**Figure 4.2. (a) (b) (c) (d) (e) Frequency distributions of diameter of PAN/AP fibres electrospun from different concentration of PAN and AP. The weight ratio of PAN and AP was fixed at 3 and the changing of PAN and AP were represented by the variation of PAN in PAN/DMF solution; (f) The dependence of PAN/AP fibre diameters on the PAN/AP weight percentage in PAN/AP/DMF solution.**

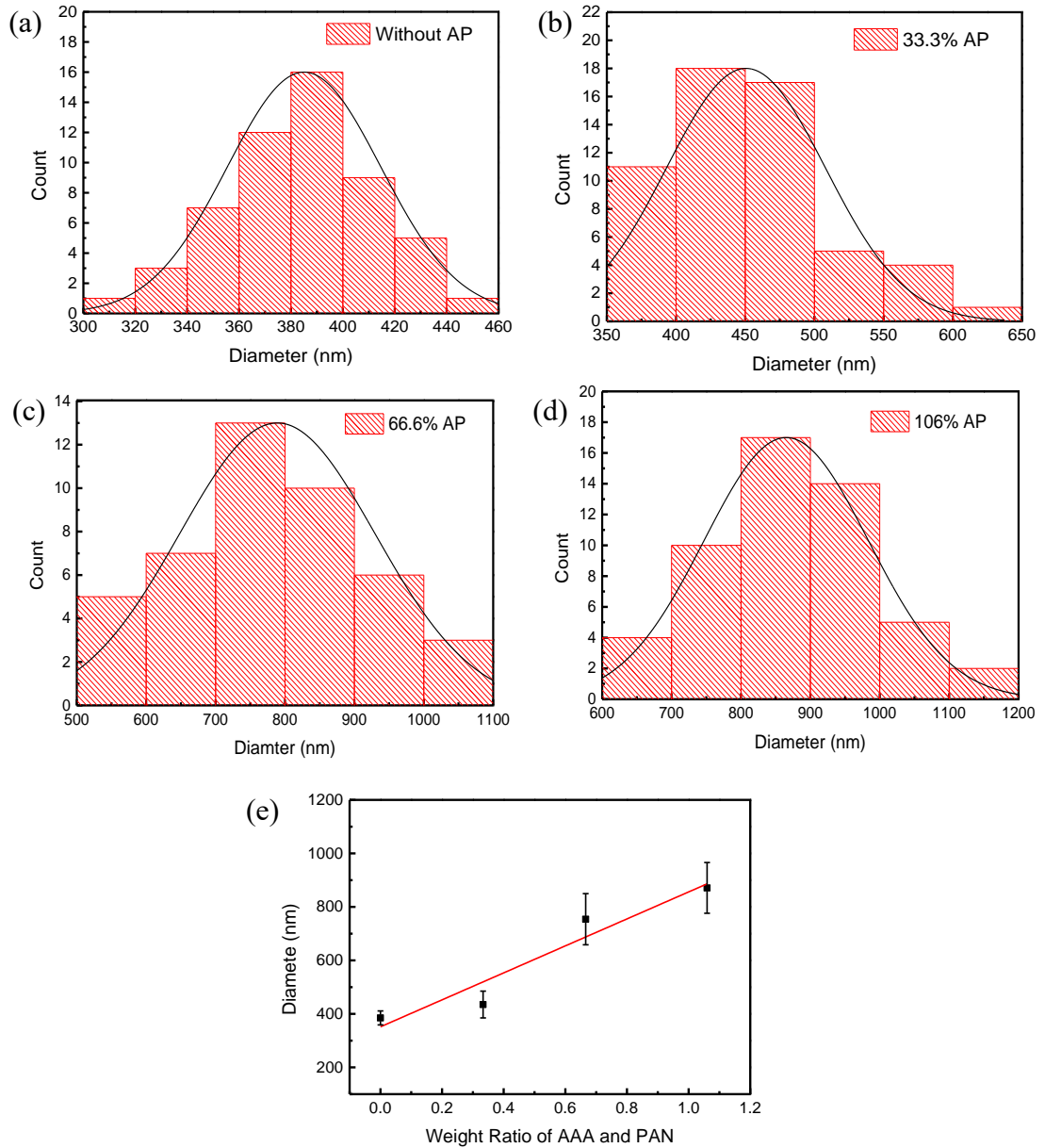


**Figure 4.3.** (a) (b) (c) (d) Frequency distribution of diameter of PAN/AP fibres electrospun from different concentration of PAN and AP; (e) The dependence of PAN/AP fibre diameters on the weight ratio of AP and PAN. The concentration of PAN in solution before AP was added was fixed at 10%.

### 4.3.2 Effect of heating procedure

Alumina has more than 20 different crystal structures and the transformation procedures differ depending on the starting status of alumina.<sup>[78]</sup> The heating procedure not only

affects the fibre morphologies and grain growth in the fibre, but also the transformation between the crystal structures. To obtain nanofibres with desired morphology and crystal structure, the influence of different calcination procedures was studied by applying different calcination temperatures and time.

The SEM images of nanofibres before and after calcination are displayed in Figure 4.4. The as-spun PAN/AP nanofibres have a straight and solid string morphology (Figure 4.4a). The calcination process degrades all the organic components with temperature so that aluminium atoms are left to react with the oxygen in the air, forming alumina nanofibres. Alumina has more than 20 different crystal structures due to the complicated possible arrangements of oxygen atoms, and the transformation procedures differ depending on the starting state of alumina.<sup>[76, 78]</sup> The influence of calcination parameters is studied by applying different calcination temperature and time to obtain nanofibres with desired morphology and crystal structure. Figure 4.4b shows polycrystalline alumina nanofibres, formed after calcination under 1200 °C for 1 h, with a diameter around 80-160 nm and grain size ranging from 15 nm to 30 nm. These fibres are slightly curved, which might be caused by the surface tension and internal stress during fibre formation as well as shrinkage of the fibre volume. Continued calcination for 4 h produce larger grains and a reduction in grain boundaries as well as a smooth external fibre surface (Figure 4.4c). Despite the important role of calcination time, the temperature is also expected to contribute significantly to the calcination process. Low temperature provides insufficient energy for atomic diffusion to form a dense fibre as well as crystal structure transformation from  $\gamma$  phase to  $\alpha$  phase. Conversely, high temperature results in enhanced mobility of atoms that lead to deformation of the alumina geometry from fibrous to platelet (Figure 4.4d), caused by a preferential growing rate direction of  $\alpha$ -alumina.



Specifically, the flat surface of the platelet corresponds to the (001) face as  $\alpha$ -alumina has the lowest surface energy and the lowest growth rate in the [001] direction.<sup>[235-236]</sup>

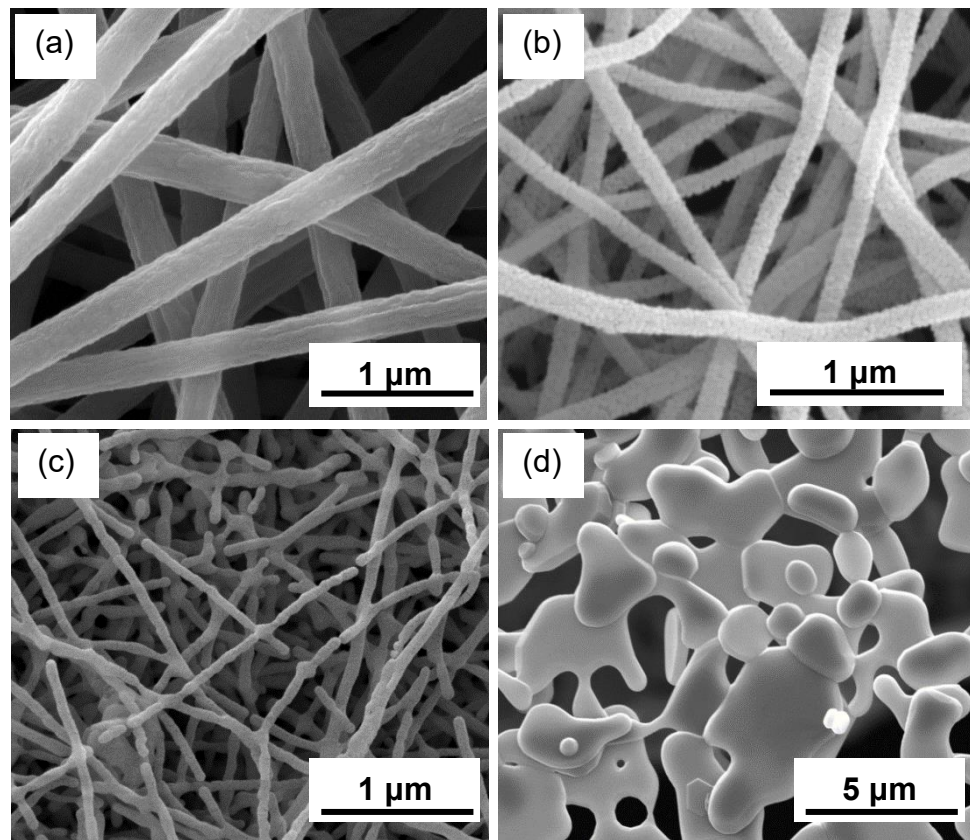


**Figure 4.4.** Scanning electron microscopy image of (a) as-spun nanofibres, (b) alumina nanofibres calcinated at 1200 °C for 1 h, (c) alumina nanofibres calcinated at 1200 °C for 4 h, and (d) alumina nanofibres calcinated at 1400 °C for 2 h.

The fibre growth procedure of alumina nanofibres was investigated with XRD, TEM and ED. The crystal structure transformation procedure of alumina fibres calcinated at 1200 °C with different time have been examined with XRD, and the results are displayed in Figure 4.5a. Here, the alumina fibre mat follows the transformation procedure as:  $\gamma \rightarrow \delta$  (orthorhombic)  $\rightarrow \alpha$  with increased calcination time, and no tetragonal  $\delta$  phase and  $\theta$  phase have been identified in this work, which is different from previous works.<sup>[67, 79-80,</sup>

<sup>87]</sup> The patterns agree well with JCPDS card No. 50-0741 for  $\gamma$ -alumina, No. 46-1215 for  $\delta$ -alumina, and No. 10-173 for  $\alpha$ -alumina, respectively. This XRD images shows that after

calcination under 1200 °C after 2 h, most of the fibres are already  $\alpha$ -alumina, but there is still a very small amount of  $\delta$  alumina in the fibre mat. After calcination for 4 h, the fibres have all converted into  $\alpha$ -alumina.

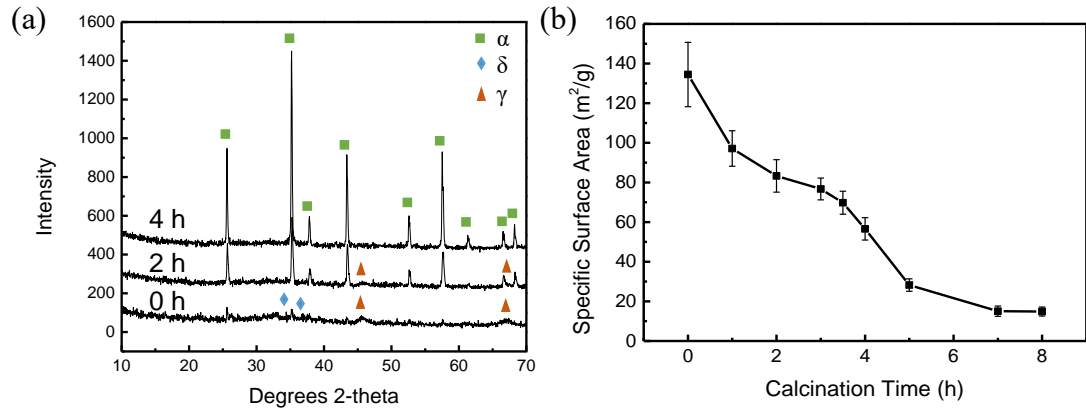


**Figure 4.5. (a) X-ray diffraction pattern for an alumina nanofibre mat calcinated at 1200 °C for a range of times. (b) Specific surface area of alumina nanofibre mats calcinated under 1200 °C for different time.**

Apart from direct morphology and crystal structure observation, the calcination process can also be indirectly explained by the relationship between the specific surface area (SSA) of alumina nanofibre mats and the calcination time under constant calcination temperature (Figure 4.5b). The overall trend of SSA declines with increased calcination time, and it is interesting to find that the declining rate during the whole process follows the sequence of fast-slow-fast. This phenomenon is caused by different sintering mechanisms during different sintering stages as well as the transformation of alumina crystal structures. In this process, the primary driving force for sintering begins with the curvature gradient in the interparticle neck region, then shifts to the excess surface energy accompanied by different atom diffusion mechanisms.<sup>[237]</sup> When the temperature has just been raised to 1200 °C, the fibres are made of very small grains and the large specific surface area provides strong driving force for sintering, leading to a rapid decrease of SSA.<sup>[238]</sup> With the pores gradually eliminated, the driving force transferred to elimination

of excess surface energy until the grain boundary disappear and the fibres showed a completely smooth surface. Grain-boundary diffusion is the dominant sintering mechanism during this stage. The fibre diameters begin to shrink due to atoms arrangements and coalescence of nanocrystals.<sup>[239]</sup> After the fibres become smooth as shown in Figure 4.4c, the atoms started to move towards the joint centre of fibres and the shape of the fibres started to change driven by the tendency to reduce the surface area, leading to orientation of forming the plate-like shape (Figure 4.4d). The decreasing rate of SSA thus falls again with the decreasing of SSA and a corresponding decreasing driven force. The changing of SSA has validated from another side that the optimal calcination time is around 3.5-4 h.

### **4.3.3 Fibre diameter change during calcination**

The change of alumina nanofibre morphologies and diameters during the whole calcination procedure were studied before tensile testing of individual nanofibres due to the important relationship between the fibre strength and diameters.

The morphology changing with the increased calcination time is shown in Figure 4.6. The fibres are made of small grains and have a porous structure when the calcination temperature just reached 1200 °C (see Figure 4.6a). The grains then continued growing and the fibre diameters began to shrink as the calcination time increased. According to the Kelvin equation<sup>[240]</sup>, the driving force for diffusion is inversely proportion to the pore's radius of curvature. The pores between the grains are extremely small, compared with the space between the fibres, thus the driving force to eliminate the small pores is much larger than to fill the gaps between the fibres and the fibre shape can be maintained. The fibre diameters decreased continuously during this stage due to the reduction of the pore size. After calcination for 4 h, the pores have all being eliminated and the fibres

showed single crystal structure as explained in section 4.3.3. After this critical point, the fibre diameters start to increase and the shape of the fibres start to change, driven by the force to reduce the surface area. The end of the fibres become round and coarse and the total length of the fibres also decrease (see Figure 4.6c). The overall trend of the fibre diameter changing during calcination is more clearly showed in Figure 4.6d. The fibres reached the smallest diameters and uniform morphologies only when the calcination time was around 4 h. Therefore, the fibre chosen for tensile testing was limited in the calcination no more than 4 h.

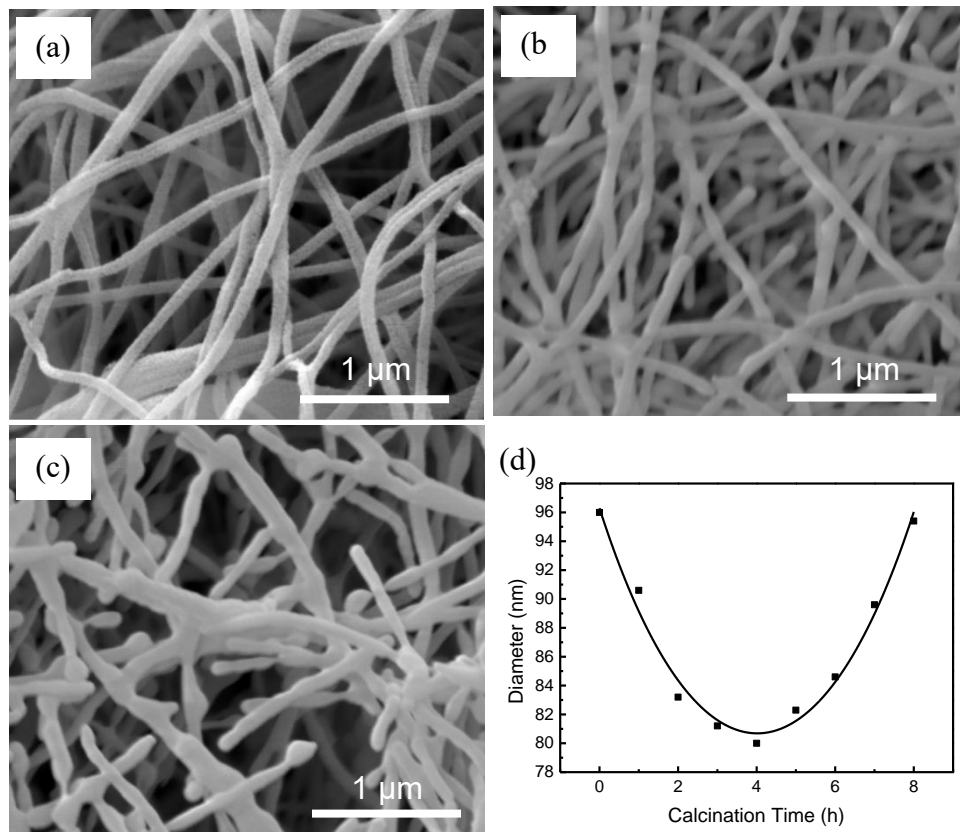


**Figure 4.6. Change of fibre morphologies during calcination at 1200 °C with the increasing calcination time: (a) 0 h, (b) 4h and (c) 7h. (d) Fibre diameters of aluminium oxide nanofibres electrospun from the same solution but calcinated under different time. The black dots are experimental value, while the solid line is the fitted value.**

### 4.3.4 Crystal structures of $\alpha$ -alumina nanofibres changing with calcination time

The transformation of alumina nanofibre from  $\gamma$  phase to  $\alpha$  phase has been studied by some previous researchers, however, the detailed transformation mechanism has never been explained in their work. To have a better understanding of the fibre growth and phase transformation mechanism for fabricating fibres with desired properties, ED was applied on individual nanofibres calcinated for different time to investigate the crystal structure transformation procedures.

Individual fibre transformation has also been confirmed by ED. The fibres were mainly  $\gamma$ -alumina after calcination for 1 h (Figure 4.7a). As calcination continued, the  $\gamma$  grains began to transform into the  $\delta$  phase. Fibres with  $\delta$  grain sizes of around 100-150 nm were found randomly located in  $\gamma$ -alumina fibres (Figure 4.7b). These  $\delta$  grains then quickly transformed into  $\alpha$  phase after continued calcination. Fibres with partial  $\gamma$  phase and partial  $\alpha$  phase were also identified in fibre mats calcinated for 2.5 h (Figure 4.7c). The  $\alpha$ -alumina part was noted as divided into short cylinders and each of the cylinders were of a similar size to the  $\delta$  grains formed in  $\gamma$ -alumina fibres, as shown in the enlarged image in Figure 4.7. The whole edge of the  $\alpha$  phase have been examined with high-resolution TEM and no grain boundary has been found, though the middle of the fibre was too thick for further observation with our equipment. Thus it is likely that the single crystal fibres are formed by grain growth of  $\alpha$  grains transformed from  $\delta$  grains, rather than coalescence of well-elongated  $\alpha$ -alumina colonies suggested by Yu.<sup>[80]</sup>

**Figure 4.7. (a) TEM image showing polycrystalline  $\gamma$ -alumina nanofibres calcinated at 1200 °C for 1 h. (b) TEM and ED images of  $\delta$ -alumina crystals grown in polycrystalline  $\gamma$ -alumina nanofibres. (c) TEM image of alumina nanofibre calcinated under 1200 °C for 2.5 h and ED images taken from areas B, C, D, E, F and G respectively. The fibre consists of both polycrystalline  $\gamma$  phase and single crystal  $\alpha$  phase. The enlarged pictures of position B and the fibre inverted 'T' crossing point show that the fibres are formed by grain growth of  $\alpha$  grains with sizes close the fibre diameter.**

The growth directions of the nanofibers were additionally seen to be inconsistent, which could be caused by mechanisms involving both screw dislocation and epitaxial growth. Specifically, growth direction  $[110]$  has been identified in the fiber containing both  $\gamma$  phase and  $\alpha$  phase (Figure 4.7c), and fiber growth along  $[001]$  has also been observed in  $\gamma/\alpha$  alumina nanofiber (see Figure 4.8). Both the  $[110]$  and  $[001]$  directions are the Burgers vector directions for  $\alpha$ -alumina, and alumina whiskers grown along both directions following the screw dislocation mechanism have been previously reported.<sup>[99-100, 241]</sup> Therefore, screw dislocation could be one of the primary growth mechanisms for  $\alpha$ -alumina nanofiber grown along  $[110]$  and  $[001]$  direction.

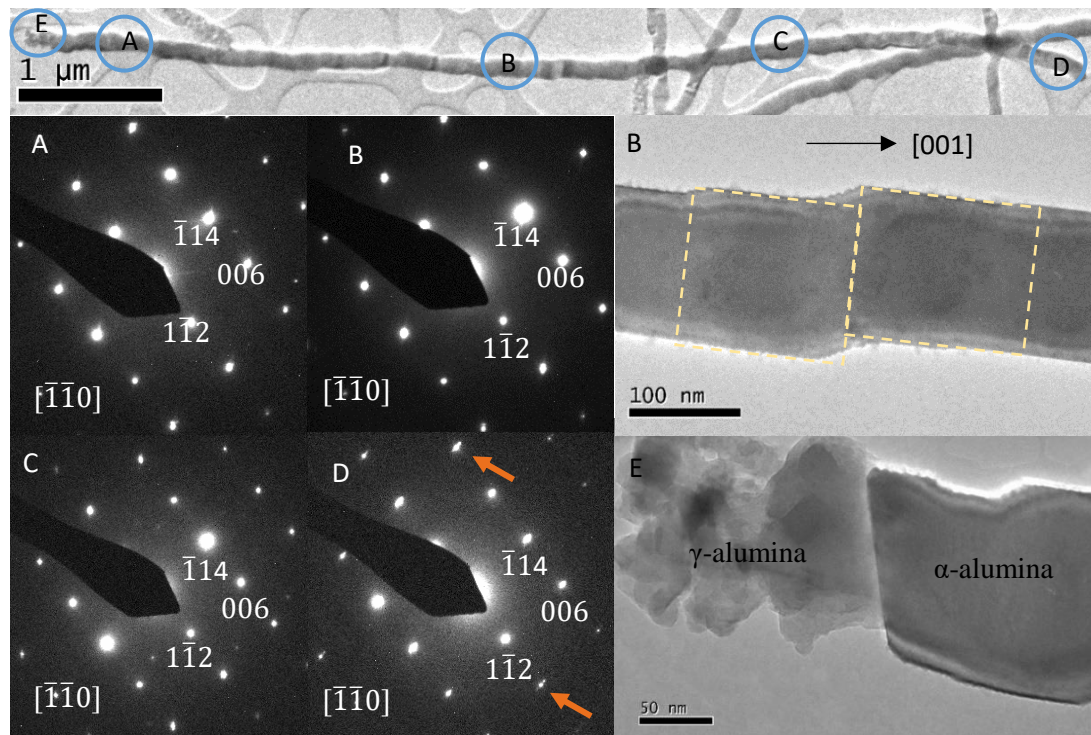


**Figure 4.8.** TEM images showing alumina nanofibres predominantly of  $\alpha$ -alumina (position A, B, C and D) and  $\gamma$ -alumina at the end (position E). ED images taken from different positions additionally indicate single crystal structure. The fibre elongates along the  $[001]$  direction. In the ED image of position D, separate diffraction spots can be observed around the primary spots (as indicated by the orange arrow), indicating low angle grain boundaries.

Chou has studied the transformation mechanism of alumina from  $\gamma$  phase to  $\alpha$  phase, and reported that the nucleation of  $\alpha$ -alumina started from the  $\{220\}$  plane of  $\gamma$ -alumina due to the high propensity of introducing stacking faults in this plane.<sup>[92]</sup> As the  $\{220\}$  plane in  $\gamma$ -alumina matches well with the  $\{220\}$  plane in  $\delta$ -alumina (orthorhombic), the nucleation may therefore start from the  $\{220\}$  plane in  $\delta$ -alumina as well. The relationship between the three crystal structures are displayed in Figure 4.9. After the grains transformed to  $\alpha$  phase, the grain growth would be rapid and follow a template grain growth (TGG) mechanism, leading to single crystal structure. Individual fibres show the same ED pattern along their length, though tilt with small steps was needed and the pattern in some parts do show separate dots in ED images, indicating low angle boundaries (Figure 4.8). The formation and growth the  $\alpha$ -alumina nanofibre therefore involves both interface boundary migration and lattice epitaxy.

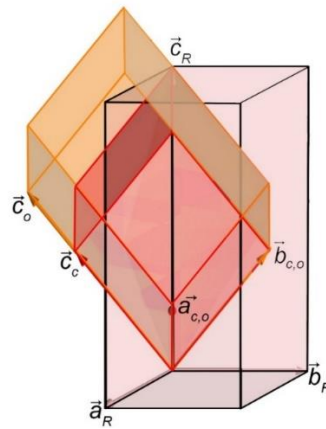


**Figure 4.9. Illustration of the crystal structure relationships between  $\gamma$ -alumina (cubic, red),  $\delta$ -alumina (orthorhombic, orange) and  $\alpha$ -alumina (rhombohedral, fade pink). The unit cell of  $\alpha$ -alumina is drawn as hypothetical ideal hexagonal close packing, so that the parameter  $c$  is equal to the cubic body diagonal.**

When the grain growth in one fibre arrives at the crossing point of two fibres, the growth will continue to the other fibre. The growth direction of the other fibre depends on the



intersection angle following the TGG mechanism, leading to other growth directions as shown in Figure 4.10.

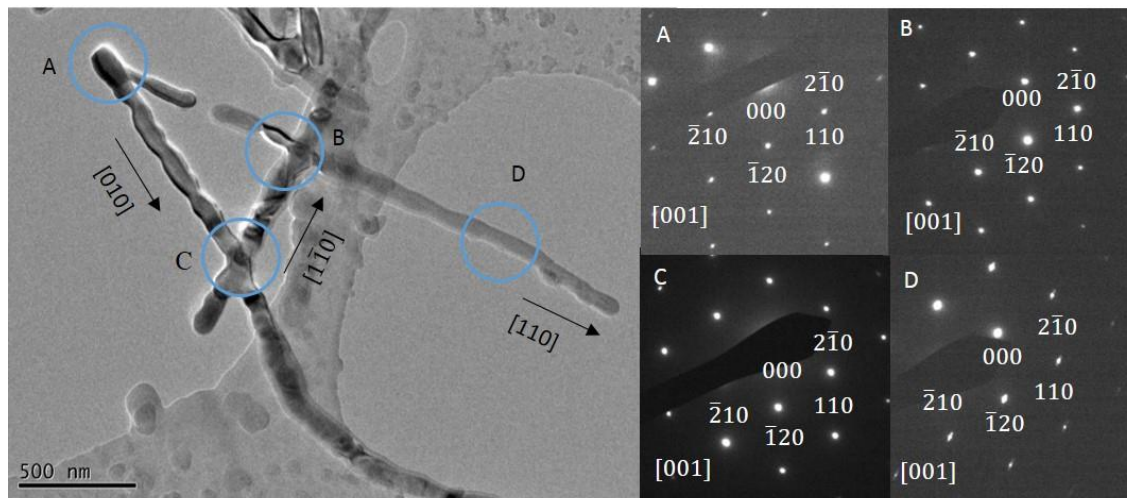


**Figure 4.10. TEM and ED images of  $\alpha$ -alumina nanofibres taken from different positions. The fibres elongate along different directions as indicated in the image.**

## 4.4 Conclusions

In this chapter, the methods to fabricate alumina nanofibres through electrospinning, the transformation between the fibre crystal structures and the fibre growth mechanism have been comprehensively investigated. The influence of the fabrication parameters (including: concentrations of polymer and aluminium precursor, calcination temperature and time) have been studied together with various characterization techniques (including SEM, TEM and XRD) to obtain the desired fibre morphology and crystal structures. The as-spun fibre diameters increase significantly with the increased concentration of both polymer and alumina precursors. Therefore, by controlling the content concentrations, as-spun fibres with different diameters can be achieved, leading to further control of the diameter of the fibre product. The crystal structure of the alumina fibres experienced a transformation procedure from  $\gamma$  (cubic) to  $\delta$  (orthorhombic), and finally  $\alpha$  (rhombohedral)

phase. Alumina fibres grow primarily along the [110] and [001] direction have been identified. Both the directions are the Burgers vector directions for alumina. Though other growth directions have also been identified following template grain growth mechanism when fibre growth arrives at the crossing point of a new fibre. The results provide sufficient information required to manipulate alumina nanofibres morphology and crystal structures by altering the fabrication conditions, leading foundation for further investigation into the dependence of the fibre strength on the morphology and crystal structures.

## 5 Tensile testing of individual nanofibres

### 5.1 Introduction

As explained in section 2.1.3, ceramic nanofibres can have significantly improved mechanical properties compared to their bulk forms due to reduced possibility of introducing critical flaws in the fibres. This scale advantage makes ceramic nanofibres fabricated through electrospinning a reinforcement material with great potential for future application.<sup>[41]</sup> Though many reseachers have already fabricated alumina nanofibres successfully, the strength of these fibres has never been measured. To prepare alumina nanofibre reinforced composite, knowing the accurate value of the fibres and the influencing factors are essential for composite design.

The fibre diameter is one of the determining parameters for the mechanical properties of ceramic nanofibres based on the work done by Inglis<sup>[39]</sup> and Griffith<sup>[37]</sup>. To fabricate alumina nanofibres with tensile strength close to the theoretical value, the relationship between the fibre diameters and the fibre strength should be related. The flexibility of electrospinning allows variation in fibre diameter down to the nano-scale, thus supporting a systematic study on the relationship between fibre diameters that potentially result in microstructural changes that define tensile strength<sup>[151, 242]</sup>. Apart from the fibre diameters, the crystal structure affect the fibre strength greatly as well. Based on the results in

Chapter 4, both polycrystalline  $\gamma$ -alumina and single crystal  $\alpha$ -alumina nanofibres have been fabricated. Single crystal structures are usually considered free from defects associated with grain boundaries, making the strength of nanofibres less dependent on fibre diameters. On the other hand, polycrystalline materials usually contain more defects and experience much poorer mechanical performance, increasing the possibility of dependence of the fibres strength on the diameters. To thoroughly investigate the dependence of tensile strength on fibre dimensions and crystal structures, the strength of both polycrystalline and single crystal alumina nanofibres need to be measured and compared.

However, due to the relatively small material dimensions, mechanical measurement of these nanofibres is challenging.<sup>[135]</sup> Though mechanical properties of ceramic nanofibres such as elastic modulus and bending strength have already been measured with atomic force microscopy or other techniques, currently very few direct measurement of the tensile strength of individual ceramic nanofibres have been reported yet.<sup>[43, 243-245]</sup> Thus, methods to measure the strength of ceramic nanofibres directly need to be explored for further investigation of the diameter-strength relationship and optimization of electrospinning processes required to maximize alumina strength.

Here in this chapter, individual nanofibre tensile strength testing are employed by a special custom-built attocube system on both polycrystalline  $\gamma$ -alumina and single crystal  $\alpha$ -alumina nanofibres with diameters ranging from 50 nm to 150 nm to provide direct mechanical information. Such an approach provides correlation between processing conditions and resultant mechanical performance so that high strength alumina nanofibres are developed.

## 5.2 Methods

### 5.2.1 Electrospun sparsely distributed nanofibres

The key for successful and effective nanotensile testing is that the nanofibres need to exceed fairly long enough from the edge of the mat and isolated with each other for the relatively big AFM probe to easily pick up individual fibre. However, since the fibre mat can be peeled from the collector only after reaching a certain thickness, the conventional collecting method using alumina foil as collector would result in a high density of fibres, which makes the later nanotensile testing very difficult to operate. To avoid this problem, sparsely distributed nanofibre mat need to be prepared.

A new collecting method with two wood pieces in parallel used as collector was introduced into the electrospinning system for collecting sparsely distributed nanofibres, and the schematic is displayed in Figure 5.1.

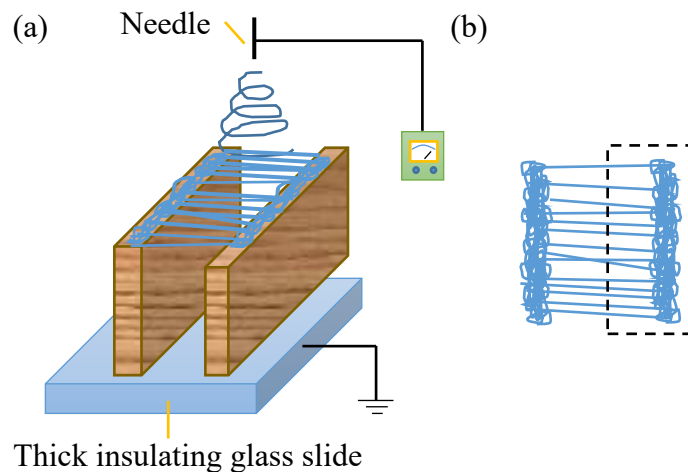


**Figure 5.1.** (a) Schematic illustration of sparse nanofibres collected with two wood pieces in parallel for individual fibre tensile testing; (b) After fibre mat was peeled from the wood and calcinated, the fibre mat was broken to expose more isolated fibres.

This collecting method has been studied by Yan<sup>[132]</sup> for fabricating aligned nanofibres, but it's not suitable for fabricating nanofibres with large quantity. Apart from the collector, the other parameters for electrospinning are all kept the same as explained in section 3.1.2. At the initial stage of electrospinning, the fibres mainly fell randomly on the top of the wood. Then a thin layer of aligned fibres was gradually built between the two wood pieces, as shown in Figure 5.1a. The whole electrospinning procedure only took about 20 minutes until the fibre mat was ready to be removed from the wood. The thicker part of the fibre mat, which was built on the top of the wood pieces, guarantees easy peeling and shape maintenance of the mat. After calcination at 1200 °C for a certain time in an alumina crucible, the mat would be broken from the middle as shown in Figure 5.1b, so that most of fibres at the edge of the mat will be sparsely distributed and stretch out.

## **5.2.2 Tensile testing of individual nanofibres**

The tensile testing of individual nanofibres was operated with a custom-built atomic force microscope (AFM) and scanning electron microscope (SEM) combined system. Details about the fundamental principle of tensile testing of individual nanofibres with AFM-SEM system have been explained in section 3.4.1. What's unique here is that, after the fibre has been picked up from the fibre mat, instead of fixing the fibre directly on the sample stage, the fibre would be fixed on a copper TEM lift-out grid with a special SEM-compatible glue for later structure observation with electron diffraction (ED) in transmission electron microscopy (TEM), as illustrated in Figure 5.2.

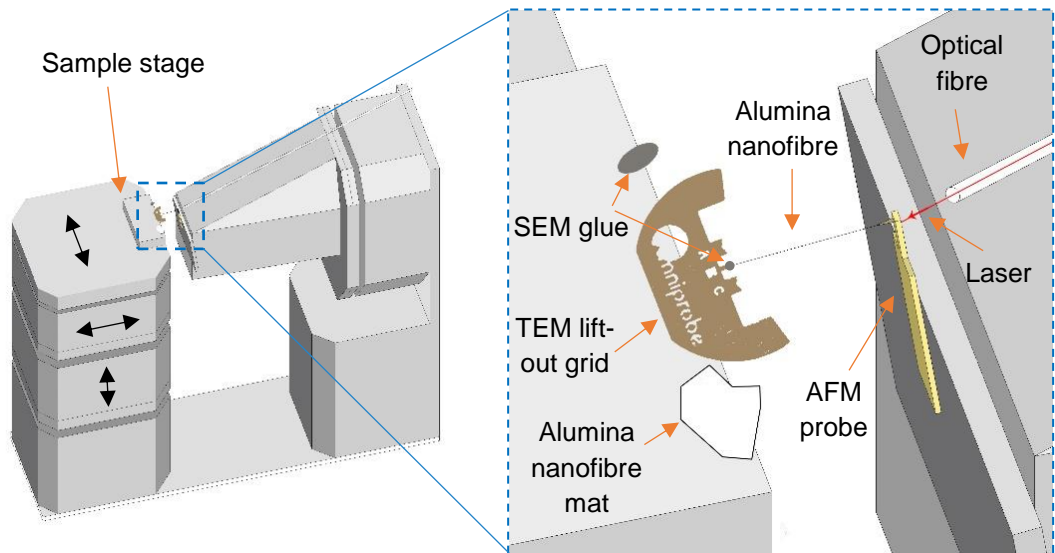


**Figure 5.2. Schematic of the custom-built AFM system used for nanofibre tensile testing. The enlarged region illustrates alumina nanofibres fixed between the TEM lift-out grid and AFM probe.**

Before testing, a small amount of glue, the TEM grid and alumina fibre mat were fixed on the sample stage as shown in Figure 5.2. The stage can be controlled to move along three directions in very small and very precise steps. An AFM probe with single crystal silicon cantilever with a spring constant around  $40 \text{ N}\cdot\text{m}^{-1}$  (Aspire CT300, Nanoscience instruments) was used and the spring constant of the AFM probes were calibrated with a thermal noise method in prior to each tensile testing. The AFM probe sits on the opposite of the sample stage and an optical fibre is used to record the bending of the cantilever.

The whole operation procedure is briefly explained as follows. Firstly, after all materials and equipment are all settled, the sample stage with the glue will move to the AFM probe for wetting the probe with a small amount of glue. The fibre mat was then moved towards the AFM probe and one of the outstretched individual nanofibres was controlled to touch the AFM probe (Figure 5.3a). The glue was cured by exposure under focused electron beam for a certain time to fix the fibre on the probe. Then the sample stage was slowly

moved backwards to break the relatively long fibre and leave the fibre fixed on the AFM probe. The TEM lift-out grid stained with SEM glue was then moved towards the other end of the fibre until the end was immersed into the glue (Figure 5.3b). The test was ready after the glue was completely cured (Figure 5.3c). Then the test was performed by moving the sample stage backwards slowly until the fibre breaks (see Figure 5.3d).

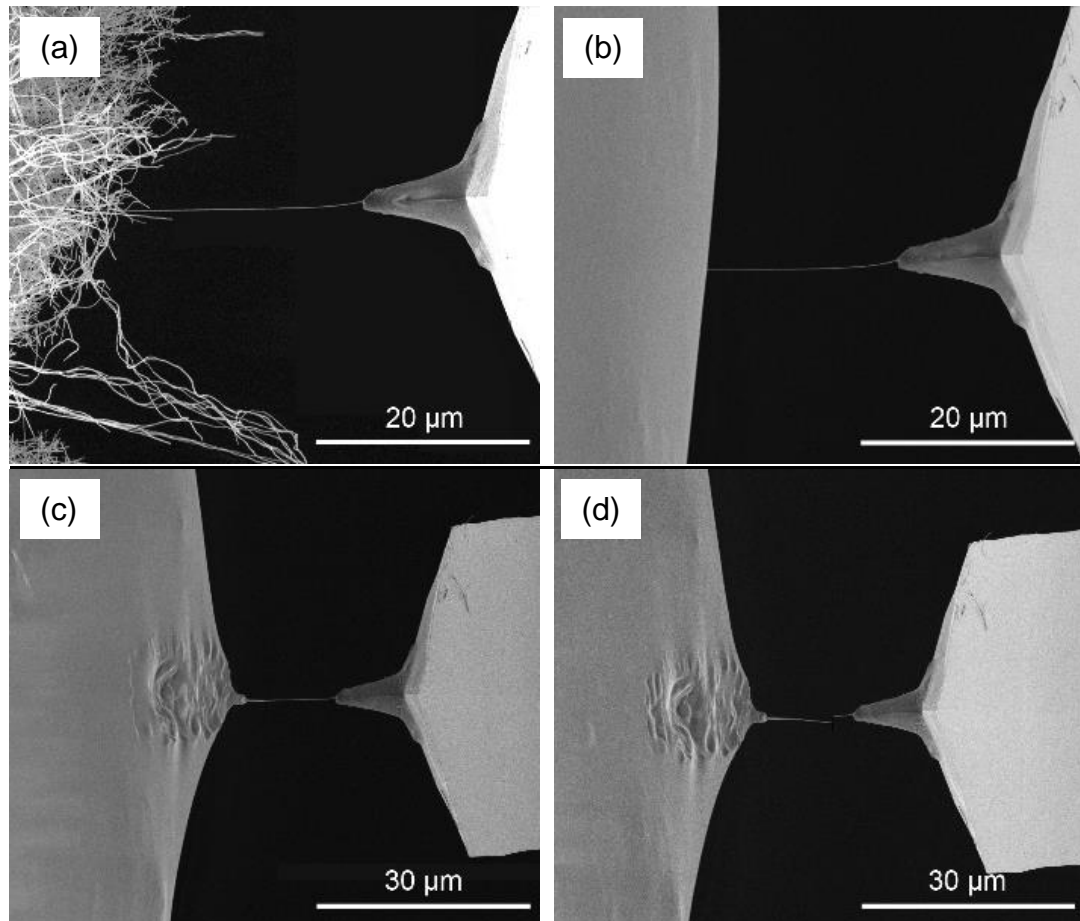


**Figure 5.3.** SEM images showing a typical procedure for tensile test of an individual alumina nanofibre. (a) The AFM probe first contacts an individual alumina nanofibre protruding from the bulk mat; (b) One end of the fibre is fixed to the tip of AFM probe (right) followed by translation of a TEM lift-out grid containing a small amount of SEM glue (left) into contact with the other free end of the fibre and (c) a focused electron beam is used to cure the glue to allow fibre fixation and subsequent tensile testing until (d) the alumina nanofibre fractures towards the middle of the fibre free length.



During the tensile testing, the cantilever of the AFM probe was bent by pulling and the maximum bending of the cantilever occurred when the fibre breaks. A laser beam reached the cantilever through the optical fibre and reflected back into the fibre. The laser reflected back from the cantilever interfered with laser reflected from the end surface of the fibre, forming a sinusoid as the distance between the fibre and the cantilever changes. The maximum moving distance of the probe was recorded by the laser interferometer optical fibre when the fibre broke, the sinusoid disappeared and became straight line as shown in Figure 5.4. The distance will then be used for the calculation of the force applied on the single fibre.

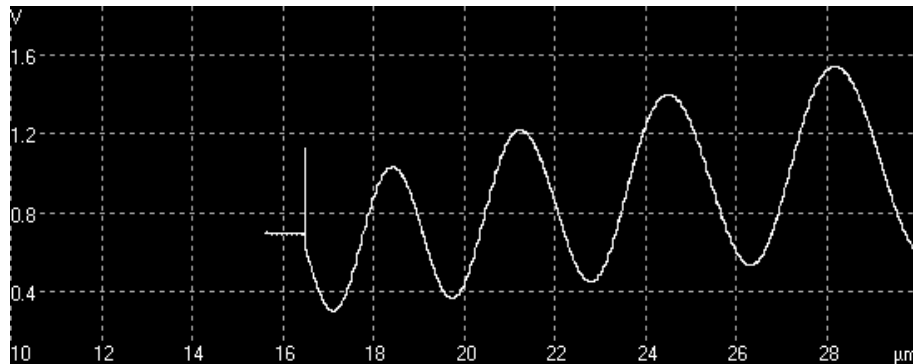


**Figure 5.4. Signal of laser intensity versus cantilever recorded by optical fibre.**

However, this moving distance can't be used directly to calculate the acting force due to the extension of the uncured glue. For fixing the extremely small fibre, only a small amount of SEM glue is required. But it's difficult to control the small amount and normally excessive glue is used. Completely curing such a large amount of glue takes a very long time, therefore quite a large amount of glue will still be uncured and causing extension during the testing, as illustrated in Figure 5.5.

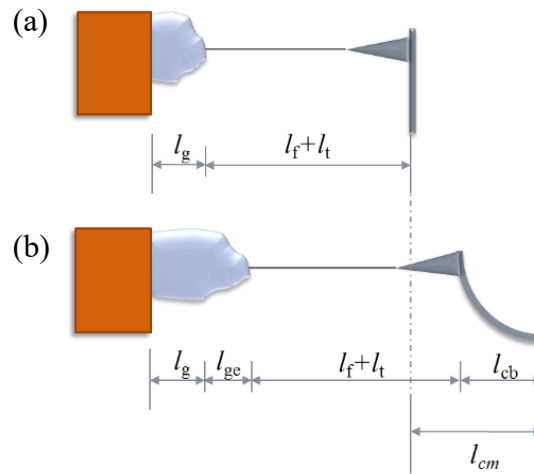


**Figure 5.5. Illustration of bending of AFM probe and stretching of SEM glue (a) before and (b) during tensile testing.**

To obtain the accurate value of acting force, the extension distance of the glue need to be taken into account. By assuming the fibre strain is neglectable, the cantilever bending distance  $l_{cb}$  was calculated with the following equation

$$l_{cb} = l_{cm} - l_{ge} \quad (5-1)$$

Where  $l_{cm}$  is the moving distance of the AFM stage, and  $l_{ge}$  is the stretching distance of the glue.  $l_{cm}$  can be recorded by the system, while  $l_{ge}$  can be measured from the image.

Thus, the stress applied on the fibre  $\sigma_f$  can be calculated as:

$$\sigma_f = l_{cb} \times k / (\pi r^2) \quad (5-2)$$

Where  $k$  is the spring constant of the probe cantilever, and  $r$  is the radius of the nanofibre. The fibre radius can be measured from SEM or TEM image. The spring constant can be calibrated with a conventional AFM equipment. The strength of the each individual nanofibre can then be calculated.

### 5.2.3 Transmission electron microscopy and electron diffraction

After tensile testing, the TEM lift-out grid was carefully removed from the sample stage of the attocube system and mounted on a double-tilt TEM sample holder for further examination. A conventional TEM was used together with electron diffraction (ED) for checking the fibre crystal structures and growth direction. The acceleration voltage for operation is 200 kV.

## 5.3 Results and discussion

The fibre mat calcinated at 1200 °C for 1 h mainly consists polycrystalline  $\gamma$ -alumina, while the fibres in fibre mat calcinated for 4 h are mainly single crystal  $\alpha$ -alumina. The sparsely distributed nanofibres greatly enhanced the possibility of successful picking up of individual alumina nanofibres from the mat. Individual fibres picked from both mats

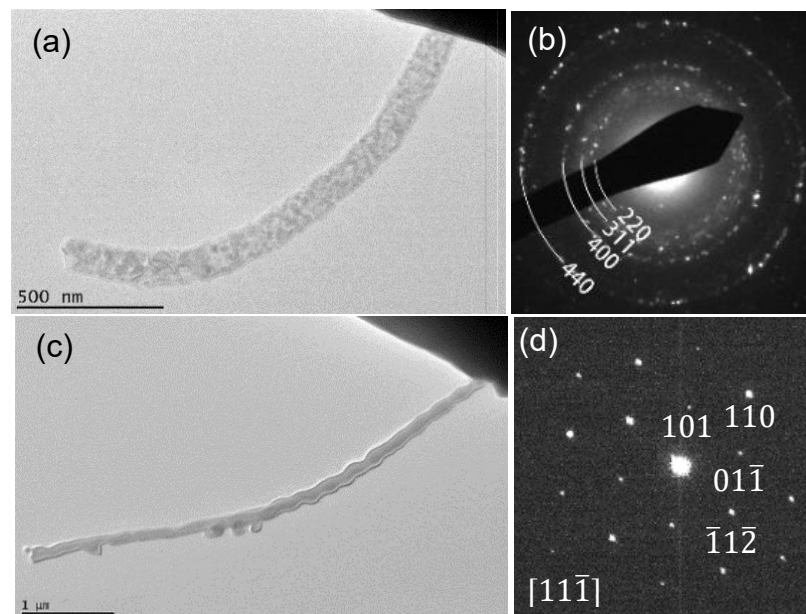


**Figure 5.6.** (a) (b) TEM bright-field image and electron diffraction pattern of single crystal  $\alpha$ -alumina nanofibre; (c) (d) TEM bright-field image and high resolution TEM image of polycrystalline  $\gamma$ -alumina nanofibre.

were carefully selected for tensile strength testing. After the testing, individual nanofibres fixed on the TEM lift-out grid were examined by TEM and ED to confirm the fibre crystal structures. Figure 5.6 shows two individual nanofibres after tensile testing. One is polycrystalline  $\gamma$ -alumina, which is calcinated for 1 h. The other one is  $\alpha$ -alumina nanofibre, which is calcinated for 4 h.

The strength of all the tested alumina nanofibres have been related to their crystal structures and are shown in Figure 5.7. Due to the different fibre diameter ranges for fibres calcinated for different time (as shown in section 4.3.3), the average fibre diameter for  $\alpha$  alumina nanofibres is smaller than that of  $\gamma$  alumina nanofibres selected for tensile testing. For  $\gamma$ -alumina nanofibres, the strength increased steadily from 2.0 GPa to 6.3 GPa as the fibre diameters decrease from 135 nm to 75 nm, showing significant diameter dependence. Smaller fibre diameters limit the possibility of large voids existence and lower stress concentration, thus provide higher tensile strength.

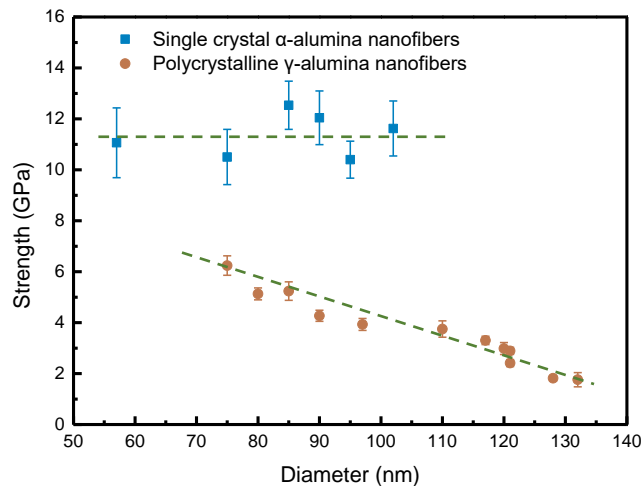


**Figure 5.7. Plot of the variation in tensile strength of individual polycrystalline  $\gamma$ -alumina nanofibres and single crystal  $\alpha$ -alumina nanofibres with fibre diameter.**

During the tensile test, these polycrystalline fibres are observed to be flexible, and the individual fibres with length around 10  $\mu\text{m}$  can be bent at more than  $90^\circ$  (see Figure 5.8).

This increased toughness of polycrystalline fibres may be due to the grain boundaries and pores between the grains, which impede the energy transfer between grains and increase the work needed for material fracture.<sup>[246]</sup>

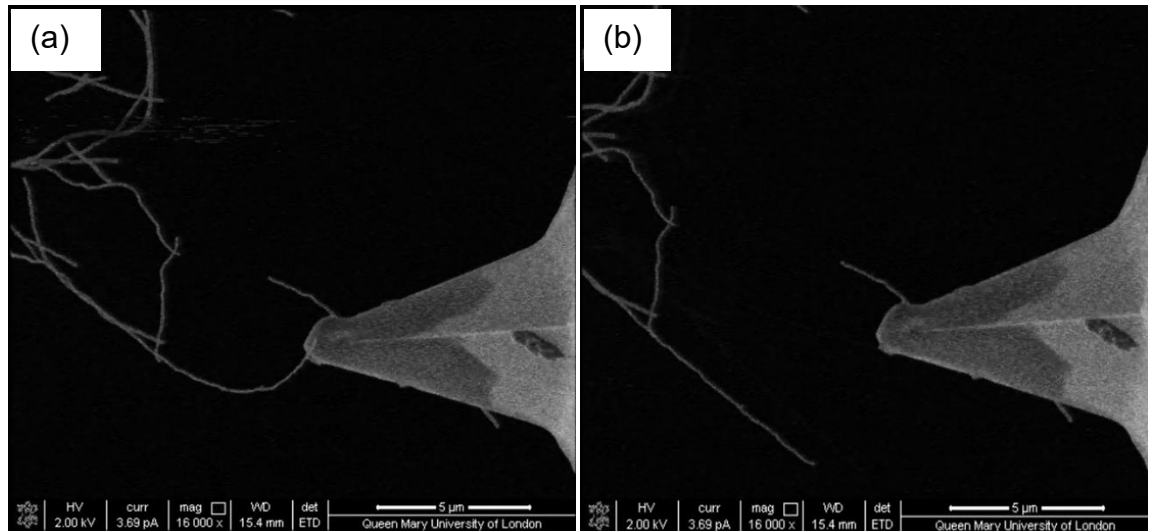


**Figure 5.8. (a) Polycrystalline  $\gamma$ -alumina nanofibre bended under force; (b) After the bending force being released, the fibre restored to straight without apparent damage.**

Currently, most applications of  $\gamma$ -alumina are based on high surface area and large volume of open mesoporosity, and the strength of  $\gamma$ -alumina has rarely been reported before, either in bulk or nano scale. Therefore, the results in our work expand the scope of  $\gamma$ -alumina applications in the future. Conversely, the single crystal fibres show no sign of diameter dependent strength and have an average strength of  $11.4 \pm 1.1$  GPa. The curved nanofibre shape may provide defects or uneven stress distribution during mechanical testing, resulting in a relatively low strength of these  $\alpha$ -alumina nanofibres compared with the alumina whiskers (22.3 GPa along [110] direction<sup>[11]</sup>).

Despite this relatively low strength compared with that of the alumina whiskers, the  $\alpha$ -alumina nanofibres show significantly higher tensile strength than most currently used industrial products (see Table 5.1). Polycrystalline  $\gamma$ -alumina nanofibres present

compatible strength to these products but has a cheaper and easier processing method. The outstanding mechanical properties and relatively low cost of these alumina nanofibres provide enormous potential for future application in various areas.

**Table 5.1. Diameter and tensile strength of strong ceramic fibres used both in industry and in this work.**

	Materials	Diameter ( $\mu\text{m}$ )	Tensile strength (GPa)
Industrial products	Zirconia-toughened alumina fibre (PRD-166 <sup>TM</sup> ) <sup>[247]</sup>	20	2.1
	Alumina fibre (Nextel <sup>TM</sup> 610) <sup>[10]</sup>	11.6	3.3
	Glass fibre (S-2 Glass <sup>®</sup> ) <sup>[248]</sup>	5.0-25	4.9
	Carbon fibre (HexTow <sup>®</sup> IM7) <sup>[249]</sup>	5.4	5.6
	Silicon carbide fibre (SCS-Ultra <sup>TM</sup> ) <sup>[250]</sup>	142	5.9
Current products	Polycrystalline $\gamma$ -alumina nanofibres	0.05-0.15	2~6 (size dependent)
	Single crystal $\alpha$ -alumina nanofibres	0.05-0.15	10~12

## 5.4 Conclusions

In summary, tensile strength of continuous alumina nanofibres fabricated through electrospinning have been measured in this chapter, and their crystal structures have been related. The strength of both individual polycrystalline  $\gamma$ -alumina nanofibres and single crystal  $\alpha$ -alumina fibres with diameters have been measured with a custom-built AFM-

SEM combined system. The strength of  $\gamma$ -alumina nanofibres shows significant diameter dependence and increase steadily from 2.0 GPa to 6.3 GPa as fibre diameters decreased from 135 nm to 75 nm. The strength of  $\alpha$ -alumina fibres is consistent at around  $11.4 \pm 1.1$  GPa across all the fibre diameters considered and exhibits a single crystal structure. The strength of both electrospun  $\gamma$ -alumina and  $\alpha$ -alumina nanofibres using the calcination processes detailed provide increased tensile strength compared with high performance industrial alumina nanofibres currently in use.

# **6 Fabrication and characterization of polycarbonate composite reinforced with alumina nanofibres**

## **6.1 Introduction**

Composites made from cost efficient, lightweight and environmentally resistant polymer matrices as well as strong fibres can give products with extraordinary properties that neither of the constituents can achieve alone.<sup>[251-252]</sup> The previous chapter provided evidence of electrospun alumina fibres with high performance properties. Usage of these fibres in engineering applications requires incorporation of the nanofibres within a larger composite structure. To fabricate such a composite, the parameters affecting the composite properties need to be investigated. Different models such as the rule of mixtures<sup>[24]</sup>, the Halpin-Tsai model<sup>[253]</sup>, the Eshelby model<sup>[254]</sup>, the shear-lag model<sup>[255-256]</sup>, the Mori-Tanaka model<sup>[257-258]</sup>, the Hashin-Shtrikman model<sup>[259-260]</sup>, and the self-consistent model (or the embedding model)<sup>[261-262]</sup> have been developed based on the matrix and reinforcement properties to describe the composite mechanical properties mathematically. Each model chooses the factors that they consider as important and ignore the non-determinants to simplify the calculation. Despite some dispute, the



intrinsic mechanical properties of the fibre itself and the fibre volume fraction are considered as key parameters in all of these models. Therefore, fibres with as high as possible strength and fibre volume fractions are considered to be ideal for high mechanical performance composites. The electrospun alumina nanofibres are promising candidates for reinforcement in polymer matrix composites due to their extremely high tensile strength, as demonstrated in Chapter 5. Hence, in this chapter, these electrospun alumina nanofibres would be fabricated into composites with polycarbonate as a matrix to obtain composites with the best possible mechanical properties.

The strength and Young's modulus of composite are usually experimentally lower than the values calculated based on these theoretical models. The reason for this overestimation is that all theoretical models are developed by assuming that the stress transfer from the matrix to the fibres are efficient<sup>[263]</sup>, while in reality the stress transfer from the matrix to the reinforcement is usually limited by fibre agglomeration<sup>[264-265]</sup> or poor fibre/matrix bonding<sup>[266-267]</sup>. Due to the incompatibility of ceramics and polymers, the bonding between the reinforcement and matrix for ceramic reinforced polymer composite is relatively poor.<sup>[166, 171, 268]</sup> Thus, further investigation into the fibre/matrix interface is required to achieve strong fibre/matrix bond for efficient stress transfer as well as resistance to environmental attack during service.<sup>[15, 173, 267, 269]</sup> Many researchers have devoted significant effort to solve the problem of improving fibre-matrix bonding by using surfactant.<sup>[167, 170-175]</sup> 3-(Trimethoxysilyl)propyl methacrylate (MPS) is a promising candidate among all the different surfactants for improving the bonding between alumina and polycarbonate since this material can form stable chemical bonds with both inorganic and organic materials.<sup>[270]</sup> The functional group ( $-\text{Si}(\text{OCH}_3)_3$ ) in MPS is hydrolysable and can be hydrolyzed and chemically bound to the ceramic surface, while the C=C group can react with polymer monomers to form composite with enhanced stress

transfer efficiency. MPS has been successfully used to improve the dispersion of alumina and silica nanoparticles in composites with vinyl ester resin and polycarbonate as matrix respectively, and both composites showed improved mechanical properties.<sup>[271-272]</sup> The above positive results provide confidence in using MPS as a surfactant to fabricate polycarbonate composites reinforced with alumina nanofibres with improved mechanical properties.

Therefore, in this chapter, polycarbonate composites reinforced with aligned alumina nanofibres are fabricated to explore the potential of producing high performances. The fibre surface of alumina nanofibres modified with MPS is expected to achieve improved interfacial bonding with polycarbonate, with the speculated reaction mechanism between MPS and alumina fibres shown schematically in Figure 6.1. The solution impregnation method used in this work for composite fabrication allows flexible adjustment of the fibres volume fractions in the final composite by adjusting the solution concentrations. The effects of surface modification and different fibre volume fractions on the composite properties are examined by tensile testing of the composite samples. The experimental results are compared with theoretical values calculated based on both Halpin-Tsai model and the shear lag model to investigate the reinforcement efficiency of alumina nanofibres.

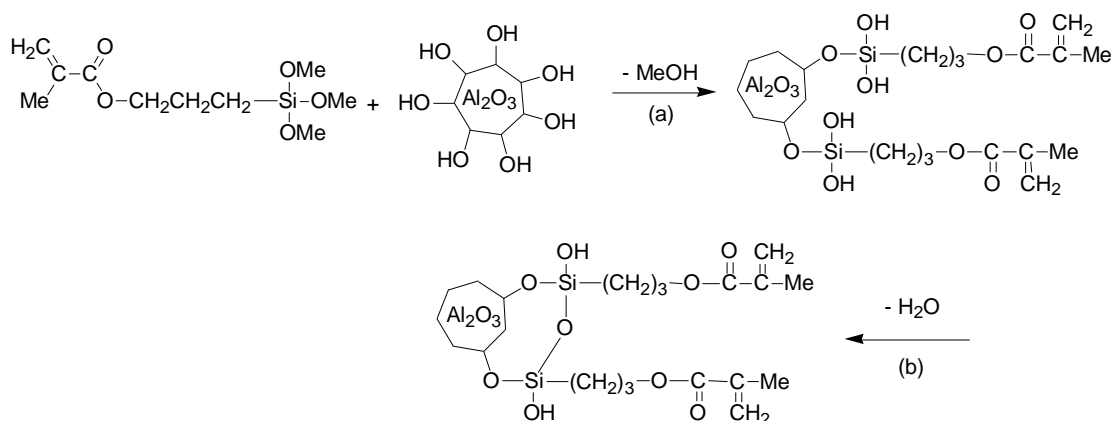


**Figure 6.1. Schematic illustration of (a) alumina reaction with MPS; (b) condensation of hydrolyzed MPS<sup>[271]</sup>.**

## 6.2 Materials and Methods

### 6.2.1 Materials

Polyacrylonitrile (PAN, average  $M_w$  150,000), aluminium 2,4-pentanedionate (AP, 99%), N,N-dimethylformamide (DMF, anhydrous, 99.8%), chloroform (anhydrous,  $\geq 99\%$ ), 3-(trimethoxysilyl)propyl methacrylate (MPS,  $\geq 98\%$ ) and heptane (anhydrous,  $\geq 99\%$ ) were purchased from Sigma Aldrich, UK. Polycarbonate (Lexan® 161R) was purchased from SABIC, Saudi Arabia. All above materials were used as starting materials without any further purification.

### 6.2.2 Fabrication of uniaxially aligned nanofibres with electrospinning

Aligned alumina nanofibre mats were fabricated prior to polycarbonate composite processing. Aligned nanofibres were considered to be beneficial so that the influence of fibre organization, such as in a random electrospun mat, could be removed and material effects determined. The electrospinning equipment and procedures were used following section 3.1.2, except for the collecting method. As illustrated in Figure 6.2a, the aligned PAN/AP nanofibres were collected using a typical roller with aluminium foil covering the surface of the drum. The rotational speed of the roller was controlled by a motor, and kept at  $7 \text{ m}\cdot\text{s}^{-1}$  in this experiment. The distance between the needle and the roller was 15 cm and the applied electric voltage was 22 kV. All the other electrospinning parameters were consistent with fabrication for randomly oriented nanofibres.

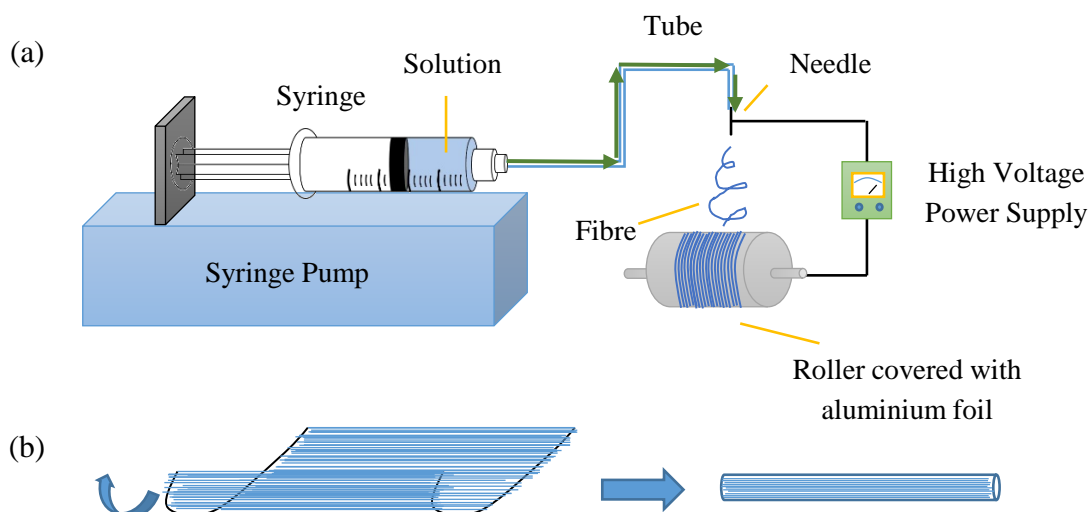


**Figure 6.2.** (a) Schematic showing electrospinning of aligned PAN/AP fibre mat. (b) Schematic illustration of fibre mat formed with aligned fibres rolled to fibre bundle.

The fibre mat of aligned PAN/AP nanofibres was removed from the roller after electrospinning for around 2 h. The fibre mat was then rolled tightly along the direction perpendicular to the fibres, as illustrated in Figure 6.2b. The fibre roll was then heated at 280 °C for 1 h for stabilization following calcination at 1200 °C for another 4 h with a heating rate of 5 °C·min<sup>-1</sup>. Thus, retention of the fibre alignment was the aim.

### 6.2.3 Surface modification

The surface of the calcinated alumina nanofibres was modified with MPS. During the experiment, 5 mg of alumina nanofibres, 5-10 drops of MPS and 5 ml heptane were firstly added into a reaction bottle. The mixture was heated at 70 °C for 120-240 min. Different amount of MPS and heating time were used to study their influence on grafting efficiency. The modified alumina nanofibre roll was then washed with pure heptane for three times to remove excessive MPS after reaction and dried under vacuum at 50 °C overnight before being fabricated into composite with polycarbonate.

## 6.2.4 Composite fabrication with solution impregnation

Polycarbonate composite reinforced with aligned alumina nanofibres were fabricated using a solution impregnation method due to its simplicity of operation and control. This method allows flexible adjustment of the fibres volume fractions in the final composite simply by changing the matrix concentration in the solution.

The procedure of composite fabrication is schematically shown in Figure 6.3. In this experiment, polycarbonate was firstly dissolved in chloroform to prepare polycarbonate solution. Different solution concentrations ranging from 5 wt% to 20 wt% were prepared to fabricate composites with variable volume fractions of reinforcement. Alumina nanofibre rolls after calcination were weighted and then immersed into the solutions with different polycarbonate concentrations overnight to allow sufficient soaking of the solution before being taken out. The polycarbonate solution had a relatively low viscosity, which allowed the solution to fully infiltrate into the roll and cover all the fibres. Extra care during transport was required since the fibres rolls were very brittle and could easily fracture. After being completely dried under vacuum at 80 °C overnight, the fibre roll covered with polycarbonate was weighted again and hot pressed into a flat strip with a regular shape (15 mm × 1.5 mm × 0.07 mm). The fibre volume fraction was then calculated according to the densities of both contents as well as the weights of the fibre roll with and without polycarbonate. The composites reinforced with both the alumina nanofibres before (BSM) and after surface modification (ASM) were named as AF/PC-BSM and AF/PC-ASM, respectively. A total of 40 composite samples with various fibre volume fractions were produced and an average fibre volume fraction from the fabrication method. Discrepancies between the experimental and theoretical fibre volume fractions are expected due to potential porosity within the samples.

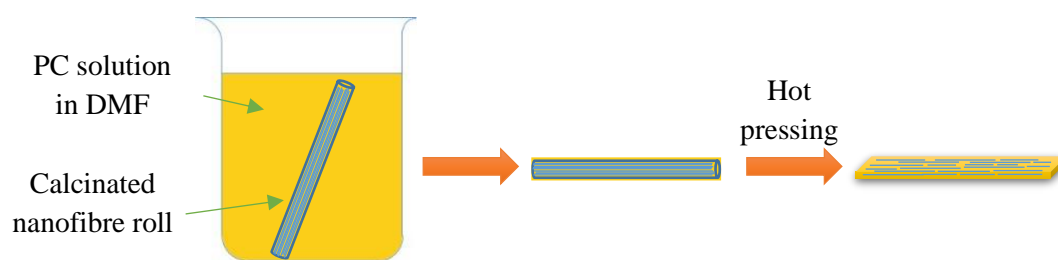


**Figure 6.3. Illustration of fabricating polycarbonate composite reinforced with aligned alumina nanofibres with solution impregnation method.**

### **6.2.5 Characterization of surface modified alumina nanofibres and polycarbonate composites reinforced with alumina nanofibres**

Morphologies of the nanofibres as well as the composites were observed with scanning electron microscopy (SEM, Inspect F, FEI). To prepare the sample for obtaining cross-section images, the composites were quenched in liquid nitrogen firstly and then quickly broken above the surface of liquid nitrogen. Infrared spectra of the nanofibres before and after surface modification with MPS has been obtained with FTIR (Tensor 27, Bruker) to confirm the chemical structures of surface modified alumina nanofibres. The chemical element analysis of the surface modified fibres was also conducted by energy X-ray dispersive spectroscopy (EDS) characterization with SEM equipment. The true composite volume was measured with a typical gas pycnometer (AccuPyc 1330, Micromeritics Instrument Corporation). Apparent sample dimensions were measured with an optical microscope (BX51, Olympus Microscopes) for later calculation of the porosity of the composites. Tensile testing of the composites was performed with a tensile stage (Microtest 200N tensile stage, Deben) at a rate of  $0.2 \text{ mm}\cdot\text{min}^{-1}$  until the composites failed. The force applied to the sample and the resultant sample displacement was recorded and converted to stress-strain curves.

## 6.3 Results and discussion

### 6.3.1 Electrospinning of aligned alumina nanofibres

The fibre alignment plays an important role in defining the mechanical properties of the final composite.<sup>[24]</sup> The composite reinforced with aligned fibres have a much higher strength along the fibre direction than the composite reinforced with the same but randomly orientated fibres. Thus, composites reinforced with aligned fibres were prepared in this study to achieve the highest possible strength.

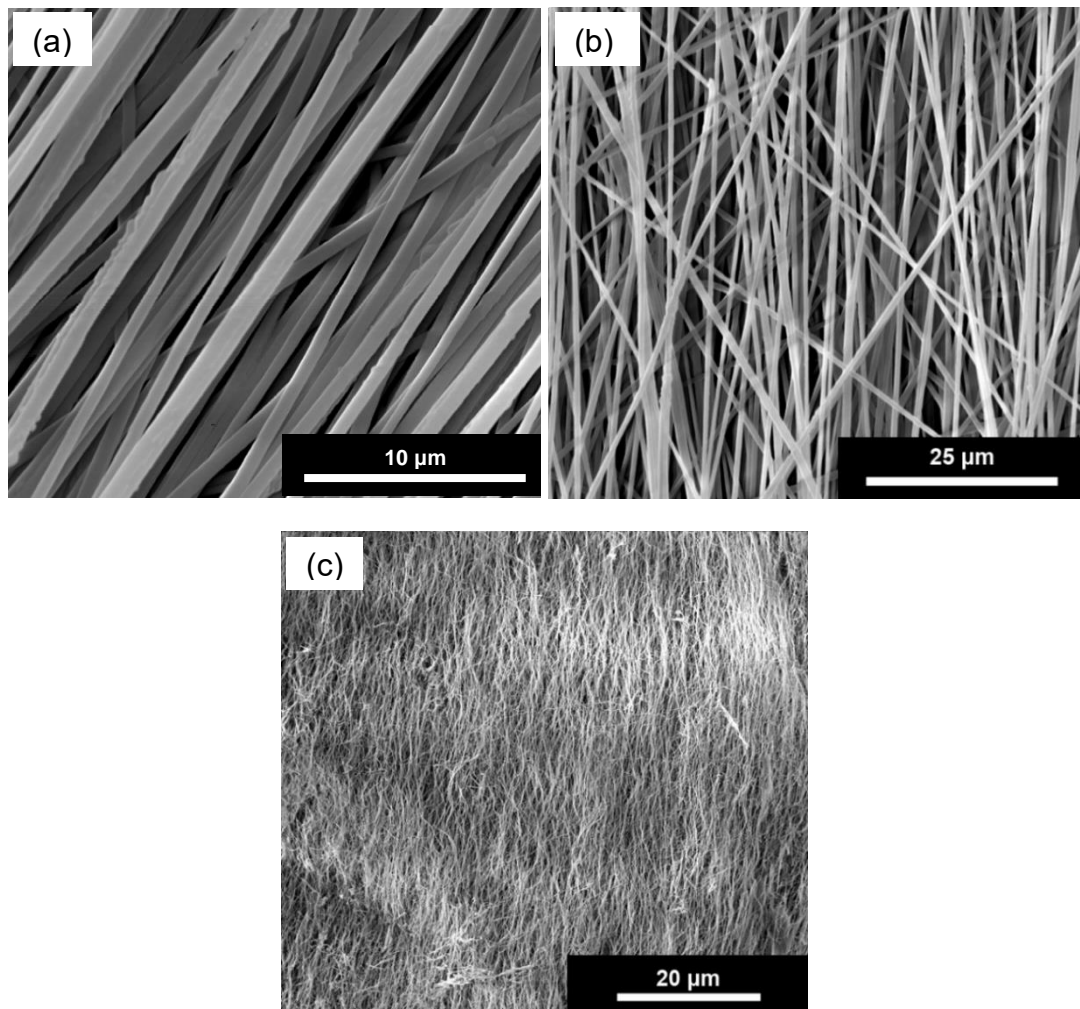


**Figure 6.4.** Scanning electron microscopy images of the aligned nanofibre mat after electrospinning for (a) 10 min; (b) 1.5 h and (c) after calcination.

The aligned nanofibres fabricated through electrospinning with roller are shown in Figure 6.4. The PAN/AP fibres electrospun within a short time of 10 min generally has a good alignment as shown in Figure 6.4a. However, as the electrospinning time increases, the alignment gets progressively worse (Figure 6.4b) due to the changed electric field distribution caused by the accumulated insulated electrospun nanofibres. Therefore, long electrospinning time should be avoided and here the fibre mats were removed from the roller after electrospinning for 1.5 h. Fibres were subsequently calcination for 4 h at 1200 °C and resulted in fibre curvature (see Figure 6.4c).

### **6.3.2 Surface modification of alumina nanofibres**

FTIR was used to characterize the chemical structure of the nanofibre mat before and after surface modification to confirm the success of the surface modification of alumina nanofibre mat with MPS for comparison, and the normalized infrared spectrum of both samples are displayed in Figure 6.5a. After reaction, the newly emerged peaks at 1017  $\text{cm}^{-1}$  and 1169  $\text{cm}^{-1}$  are absorption bonds of stretching vibrations of esteric C–O bond, while the peak at 1465  $\text{cm}^{-1}$  belongs to scissoring bending vibration of  $\text{CH}_2$  group.<sup>[273]</sup> The peaks 1638  $\text{cm}^{-1}$  and 1721  $\text{cm}^{-1}$  are due to the C [double bond, length as m-dash] C vibrations and carbonyl stretching of the ester group, respectively.<sup>[274]</sup> The disappearance of the peak at 818  $\text{cm}^{-1}$ , which is characteristic of  $-\text{Si}-\text{OCH}_3$ <sup>[271]</sup>, and the existence of other peaks characteristic of MPS in post-treated nanoparticles, indicate the complete reaction between MPS and hydrolyzed alumina nanoparticles. However, even with higher MPS concentration in heptane and longer reaction times, the intensities of these newly emerged peaks stay at the same level. The chemical elements have also been detected for further confirmation of the results of surface modification, especially the quantity of MPS attached to the fibre surface by EDS (see Figure 6.5b). No apparent weight ratio increase



of silicon on the fibre surface can be observed. These results show that though MPS has been successfully grafted on the fibre surface, the grafted quantity is limited due to the steric hindrance effect<sup>[171]</sup>.

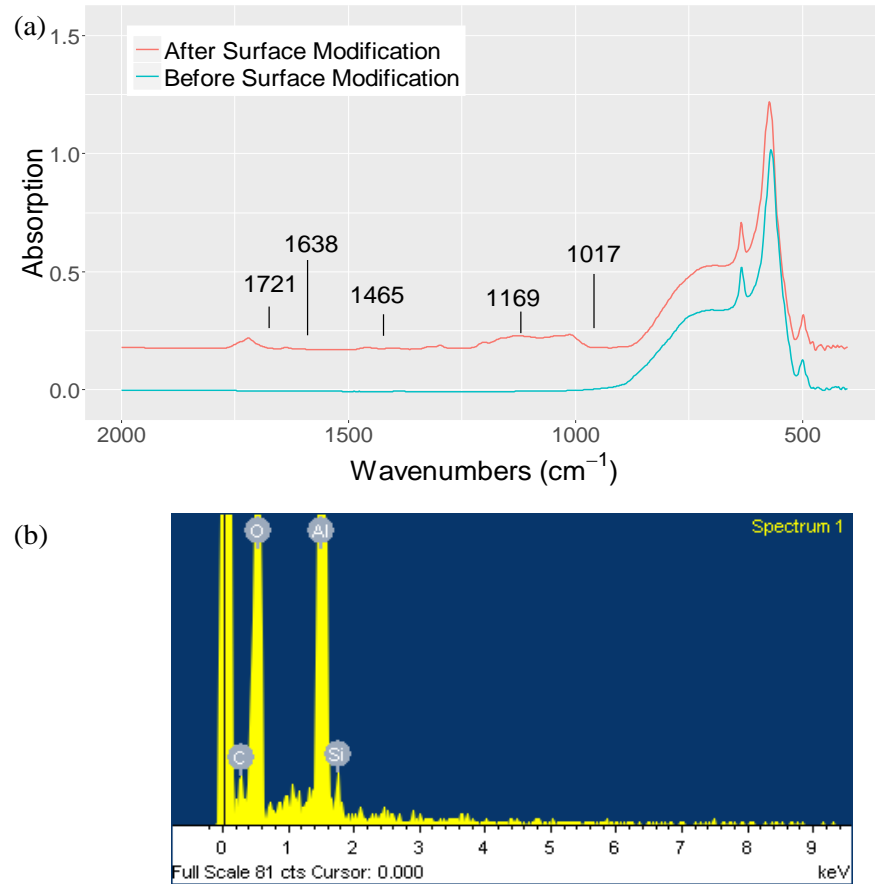


**Figure 6.5. (a) FTIR of alumina nanofibres before and after surface modification; (b) EDS spectrum of alumina nanofibres modified with MPS.**

Direct comparison of the effect of surface modification was made by imaging cross-sections of both composites AF/PC-BSM and AF/PC-ASM, displayed in Figure 6.6. The composite AF/PC-BSM shows obvious gaps between the fibres and the matrix (see Figure 6.6a), while after surface modification, the composite AF/PC-ASM has a significantly improved fibre/matrix interphase with the absence of gaps (see Figure 6.6b). These observations indicate an effective surface modification and improved bonding between the fibres and the polycarbonate matrix.

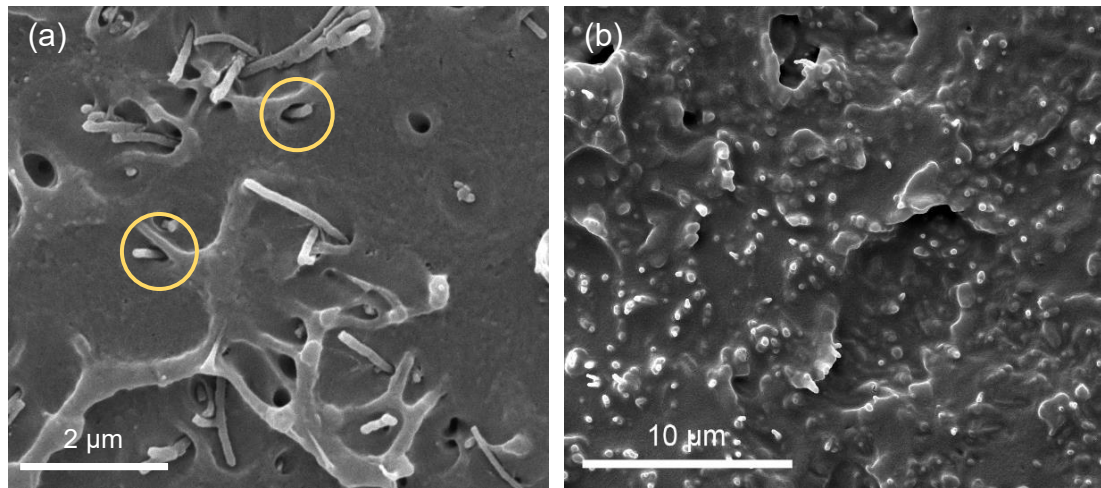


**Figure 6.6.** Scanning electron microscopy images of composite cross-sections of (a) AF/PC-BSM and (b) AF/PC-ASM.

### **6.3.3 Mechanical properties improvement of composite reinforced with surface modified alumina nanofibres**

Tensile testing of both composites AF/PC-BSM and AF/PC-ASM with varied fibre volume fractions is performed here to study the influences of different fibre content on resultant mechanical performance. The representative stress-strain curves for the composites are shown in Figure 6.7 below.

As shown in Figure 6.7, composites AF/PC-ASM with three different fibre volume fractions all present significantly improved strength when comparing with composite AF/PC-BSM. The composite reinforced with 3.9 vol% alumina nanofibres show a necking region, which is similar to the stress-strain curve of the pure polycarbonate.<sup>[275]</sup> With the fibre content increased to 10 vol% and 15 vol%, the necking region disappears, and the breaking strains of the composites reduce significantly with increasing fibre volume fraction.

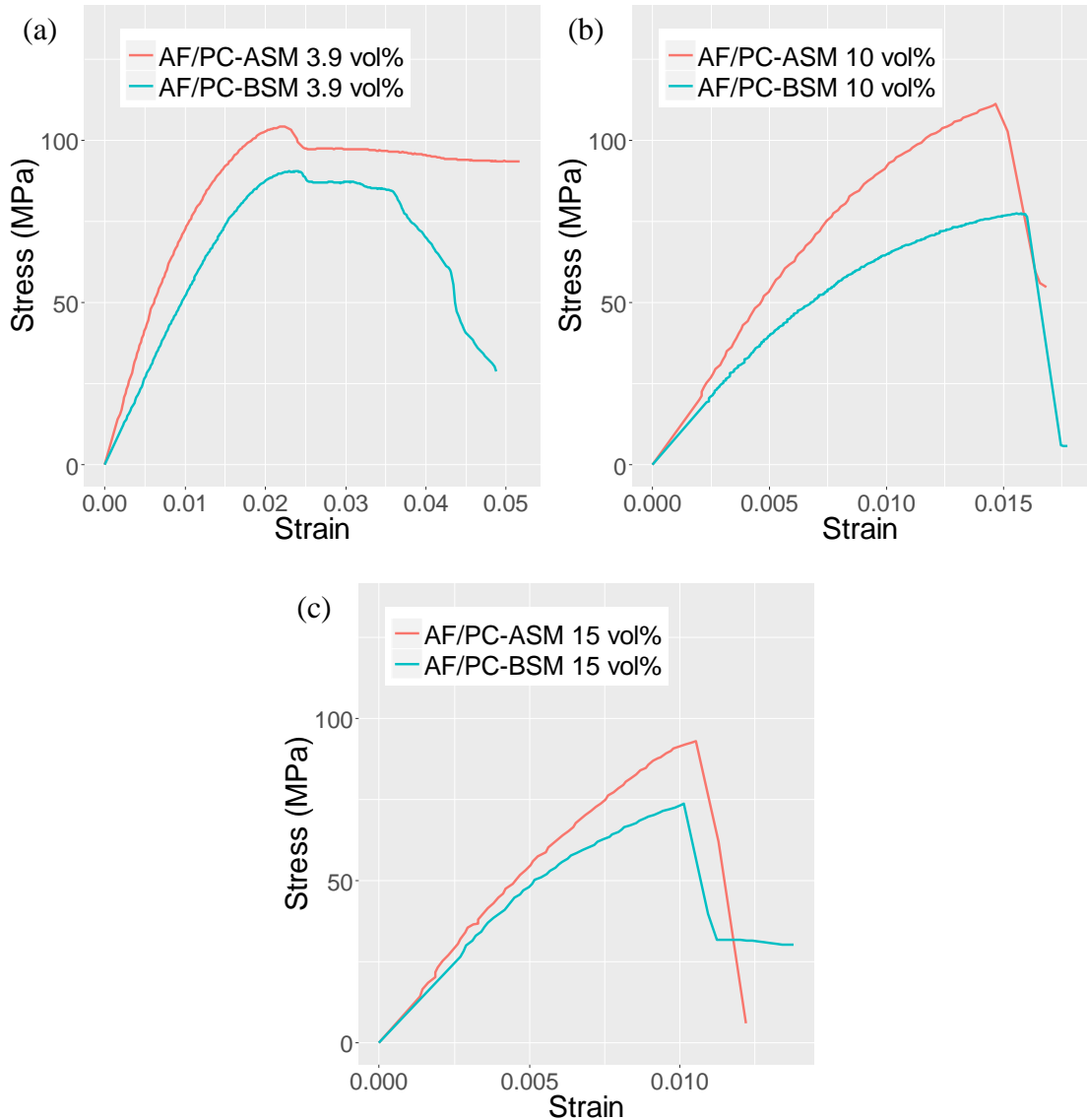


**Figure 6.7. Stress-strain curves of polycarbonate composites reinforced with alumina nanofibres before and after surface modification with a concentration of (a) 3.9 vol%, (b) 10 vol% and (c) 15 vol%, respectively.**

The tensile strength and Young's modulus of all samples were arranged and shown in Figure 6.8 to give a more clear development trend of the composite properties. The tensile strength and Young's modulus of pure polycarbonate has been measured in preliminary experiments and the value is  $58.8 \pm 2.9$  MPa and  $2.35 \pm 0.35$  GPa, respectively. As a comparison, the tensile strengths of both composite AF/PC-BSM and AF/PC-ASM show

significant strength improvement with the presence of alumina nanofibres. The composite strength of both series increase with the growing fibre volume fractions until reaching the volume fraction of around 7.5% for composite AF/PC-ASM, and 6% for composite AF/PC-BSM. After reaching these critical points, the strength of both sample series start to decrease. The reason for this strength decrease may be that the larger amount of alumina nanofibres reduce the mobility of the melt composite. Voids, such as air bubbles, are therefore potentially retained after hot pressing, leading to more defects in the materials. Despite the relatively poor performance of composite with fibre volume fraction more than 10%, the tensile strength of the composite doubled and the Young's modulus increased by a factor of 4 for composite AF/PC-ASM when compared with the composites with a fibre volume fraction of around 7.5%.

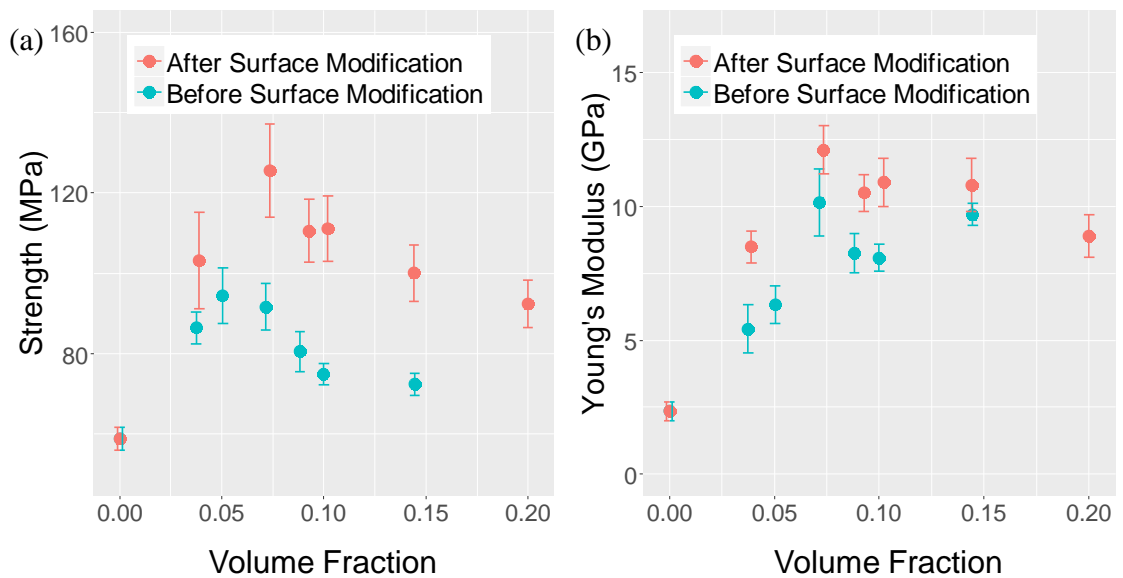


**Figure 6.8. Comparison between tensile strength and Young's modulus of composites reinforced with aligned alumina nanofibres before and after surface modification.**

To test the hypothesis of the strength decrease caused by the increased voids in the composite with increased fibre volume fractions, the dependence of the composite porosities on the fibre volume fraction in the composite was measured by a gas

pycnometer and the results are shown in Figure 6.9. The composite porosity shows a clear rising trend with the increased fibre volume fraction, despite the relatively large error. The composite porosity generally stays constant when the volume fraction is less than 6%, but shows significant increases when the volume fraction goes beyond this region, which provides a reasonable explanation for the strength loss in Figure 6.8.

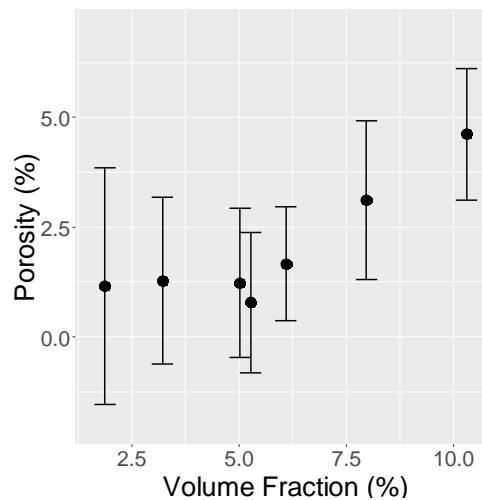


**Figure 6.9. Porosity of the composites reinforced with different volume fractions of alumina nanofibres.**

### 6.3.4 Theoretical Young's modulus calculation

Many theoretical models have been developed to predict the longitudinal Young's modulus of composites reinforced with uniaxially aligned short fibres. Among all these models, the Halpin-Tsai model is one of the widely used models and gives a simple and relatively accurate prediction, while the shear lag model is reported to have a good prediction when the fibre aspect ratio is larger than  $10^{[263]}$ . Therefore, here these two models were chosen to calculate the theoretical Young's modulus of composites reinforced with alumina nanofibres to examine the efficiency of the reinforcement.

### 6.3.4.1 Theory of the Halpin-Tsai's model

The Halpin-Tsai model is an empirical equation, which was designed for composites reinforced with continuous fibres originally, and was developed further with the parameter of fibre aspect ratio to predict mechanical properties of aligned short fibre reinforced composites.<sup>[263, 276]</sup> Compared with the simple rule of mixture, the significant improvement of the Halpin-Tsai's theory is incorporation of fibre geometry, packing geometry and loading conditions, thus providing much more accurate predictive power.<sup>[277]</sup> While fibre alignment in these AF/PC composites is not ideal, here a 100% unidirectional fibre alignment will be assumed to simplify the model. For composite reinforced with continuous aligned fibres, Young's modulus of the composite  $E_c$  can be expressed as:

$$E_c = E_m (1 + \xi \eta v_f) / (1 - \eta v_f) \quad (6-1)$$

$$\xi = l / r \quad (6-2)$$

$$\eta = (E_f / E_m - 1) / (E_f / E_m + \xi) \quad (6-3)$$

where  $E_m$  is the Young's modulus of the matrix,  $E_f$  is the Young's modulus of the fibres,  $v_f$  is volume fraction of the fibres in the composite, while  $r$  and  $l$  are the radius and the length of the nanofibres, respectively. The term  $\xi$  is an empirical factor, which describes measurement of reinforcement of the composite material that depends on the fibre geometry, packing geometry and loading conditions, and it can be expressed as:

$$\xi = 2l / D \quad (6-4)$$

Generally, this model gives accurate mechanical properties prediction with a low volume fraction of fibres. However, for composites with higher volume fraction, it usually

underestimates the stiffness.<sup>[252]</sup> Thus, modifications sometimes are required for more proper predicting.

#### 6.3.4.2 Theory of the shear lag model

The shear lag model is a model designed to predict properties of composite reinforced with short fibres<sup>[24]</sup> and the model focuses mainly on the interfacial shear stress for transferring the stress from the matrix to the fibre. The principle of this model is to simplify the composite into a unit consisting of a single fibre with a radius of  $r$  surrounded by a concentric cylindrical shell of matrix with a radius of  $R$ , as shown in Figure 6.10.

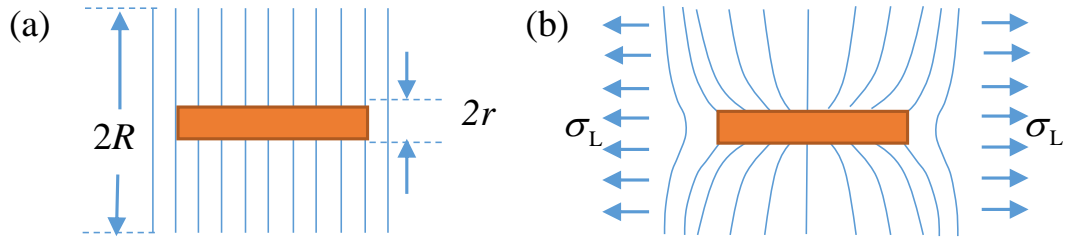


**Figure 6.10. Schematic illustration of shear lag model. (a) Unstressed composite system; (b) stress  $\sigma_L$  applied along the fibre direction.**

The longitudinal Young's modulus of the composite reinforced with aligned fibres can then be expressed as:

$$E_L = \eta_s \cdot v_f \cdot E_f + (1 - v_f) E_m \quad (6-5)$$

$$\eta_s = 1 - \frac{\tanh(\beta l/2)}{\beta l/2} \quad (6-6)$$

$$\beta = \left( \frac{H}{\pi r^2 E_f} \right)^{1/2} \quad (6-7)$$

$$H = \frac{2\pi G_m}{\ln(R/r)} \quad (6-8)$$

$$R = r \sqrt{\frac{K_R}{V_f}} \quad (6-9)$$

Where  $E_L$  is longitudinal Young's modulus of the composite,  $E_f$  and  $E_m$  represents the Young's modulus of the fibre and the matrix, respectively.  $l$  is the fibre length,  $G_m$  is the shear modulus of the matrix and  $\eta_s$  is a length-dependent efficiency factor.  $K_R$  is a constant and can be selected according to different ways that the fibres are arranged. If the fibres

are assumed being arranged hexagonally,  $K_R$  can be expressed as:  $K_R = \frac{2\pi}{\sqrt{3}}$ .<sup>[263]</sup>

#### 6.3.4.3 Calculation and comparison

Most of the parameters used in these two models, including:  $E_m$ ,  $E_f$ ,  $V_f$  and  $G_m$ , can be easily accessed except for the accurate fibre length since the fibres are all broken while hot pressing. The composites after hot pressing were heated to 800 °C for degrading the organic part and only the alumina nanofibres were left. The lengths and diameters of these nanofibres were therefore measured and a histogram of both diameter and length of around 200 fibres were produced, as shown in Figure 6.11. Thus, the average fibre length and diameter were obtained and listed in Table 6.1 for theoretical estimation.



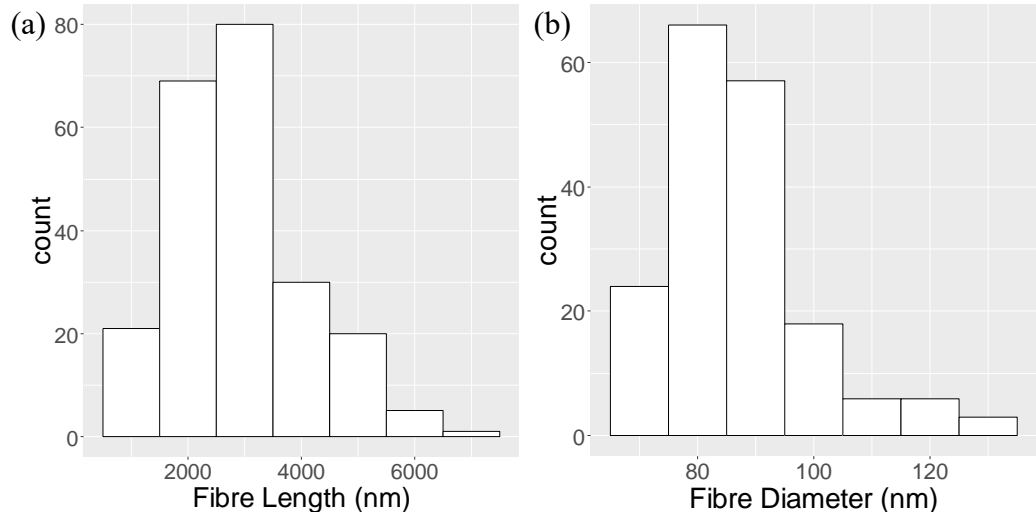


**Figure 6.11. (a) Length and (b) diameter distribution of nanofibres in composites after hot pressing.**

The theoretical Young's modulus of the composite reinforced with varied volume fractions of the fibres were calculated with the parameters listed in Table 6.1 and the calculated results and the experimental values are compared in Figure 6.12.

**Table 6.1. Parameters for calculation of theoretical composite Young's modulus.**

Parameter	$E_f$	$E_m$	$G_m$	$l$	$r$
Value	435 GPa	2.35 GPa	0.914 GPa <sup>[278-279]</sup>	2.9 $\mu\text{m}$	44 nm

As shown in Figure 6.12, the Halpin-Tsai model and the shear lag model give similar predictions for the Young's modulus of composites with fibre volume fractions in the range of 0~20%. The predicted results of both models are close to the experimental value when the fibre volume fraction is less than 7%. However, when the fibre volume fraction exceeds 7%, the deviation between the theoretical and the experimental results increases significantly with increasing fibre content. A deviation of 16.5% between the experimental Young's modulus and the theoretical value calculated with Halpin-Tsai

model can be observed for the composite with a fibre volume fraction of 7.35%, and this deviation grows continuously with increased fibre volume fraction. The predicted Young's moduli of composites with low fibre volume fraction for both models demonstrate that the stress on the composites has been transferred to the fibres effectively and good bonding forms between the fibres and the matrix. The Halpin-Tsai model gives a slightly more accurate prediction. However, as for the composites with higher fibre volume fractions, the model gives an overestimation due to the increased amount of voids in the composite.

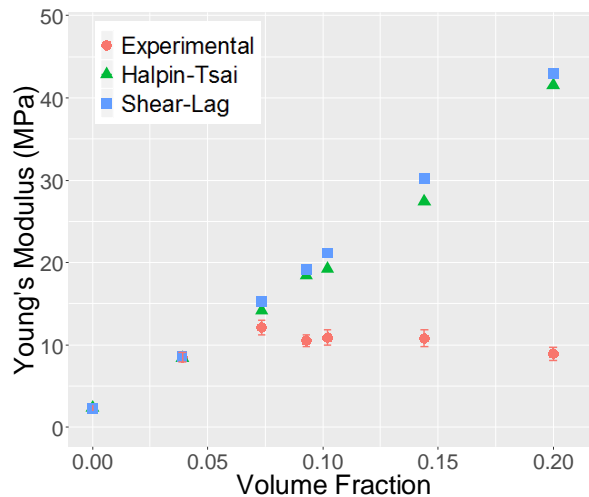


**Figure 6.12. Comparison between theoretical Young's modulus and composite reinforced with aligned alumina nanofibres after surface modification.**

## 6.4 Conclusions

In this chapter, composite of polycarbonate matrix reinforced with aligned alumina nanofibres have been fabricated and different parameters affecting the composite mechanical properties have been investigated. Aligned alumina nanofibres were collected by a spinning roller, and the surface of the fibres were then modified with 3-methacryloxypropyltrimethoxysilane to achieve better fibre/matrix bonding. The tensile

strength and Young's modulus of alumina nanofibres with and without surface modification have been measured and the results prove that the introduction of surfactant successfully improved the composite mechanical properties. When the fibre volume fraction is low (less than 7.5%), composite strength increases progressively with increasing volume fraction. However, the composite containing higher fibre volume fractions exhibits relatively poor mechanical properties. The possible reason for this phenomenon is that the higher fibre volume fraction decrease the permeability of the solution, causing more voids trapped in the composite during hot pressing and impairing the composite mechanical performance. With a fibre volume fraction of around 7.5%, the composite strength doubled and the Young's modulus increased by a factor of 4 when compared with the pure polycarbonate after surface modification. Theoretical estimations based on the Halpin-Tsai equations and the shear lag model have been proposed to evaluate the efficiency of the reinforcement. Both models give fairly good estimations of the composite Young's modulus at low fibres volume fractions, but overestimated the modulus when the fibre volume fraction exceeds around 7%, due to the presence of increasing defects.

# **7 Transcrystallization of polycarbonate induced by alumina nanofibres**

## **7.1 Introduction**

Polymers are usually reinforced with various types of materials such as fibres and particles to form composites with enhanced mechanical properties to meet the increasing demand for strong but light materials. In some fibre reinforced semicrystalline polymer composites, the matrix has been found to be able to crystallize around the fibres under certain thermal conditions.<sup>[186, 188, 280-282]</sup> A number of mechanisms have been proposed as the cause of this crystallization phenomenon<sup>[17, 190]</sup>, with heterogeneous nucleation of the polymer induced by the fibre surface leading to initiation of polymer spherulites more generally accepted<sup>[192-193]</sup>. The growth of the spherulites are constrained and lead to a primary growth axis perpendicular to the fibre surface, resulting in unique transcrystalline morphology of polymer crystals at the interface region between the fibre and the matrix.

Polycarbonate (PC) is a common matrix material used in the composite industry due to light weight and relatively high mechanical performance. The phenyl groups on the main chain and the methyl side of polycarbonate reduce the mobility of individual molecules leading to a relatively high viscosity in the fluid state and an increase in molecular

stiffness. The latter point inhibits crystallization of polycarbonate such that the polymer is known as typically amorphous with a crystallization half-time of 12 days at 190 °C<sup>[197]</sup>. Limited studies on polycarbonate transcrystallization in composites have been carried out using conventional engineering fibres<sup>[193, 200-201]</sup>. However, developments in novel nanofibrous materials are providing opportunities to examine unique polymer-nanofibre combinations that give synergetic approaches where the enhanced mechanical performance of the nanofibre is complimented by additional modification of the polymer matrix. Electrospun alumina nanofibre (AF) is one of the promising candidates to promote transcrystallization of polycarbonate due to the mismatch of thermal conductivity between alumina and polycarbonate as well as the high specific surface area of alumina nanofibre. The thermal conductivity of alumina is two orders of magnitude higher than that of polycarbonate. Therefore, a thermal gradient could be built near the AF/PC interface, and the fibre surface would have a lower temperature leading to a large supercooling.<sup>[283]</sup> This phenomenon may increase the nucleation rate of polycarbonate and eventually give rise to transcrystallinity.<sup>[284]</sup> The large specific surface area and high surface free energy of alumina nanofibre could also promote transcrystallization of polycarbonate, since the nucleation growth is a process of minimizing free energy.<sup>[21]</sup> Thus, polycarbonate matrix reinforced with electrospun alumina nanofibre could be a suitable system for investigating the formation of transcrystallization of polycarbonate as well as the effect on composite properties.

The effect of the transcrystalline layer on the mechanical properties of composites has revealed a number of key requirements for improved performance.<sup>[20-21, 285]</sup> The interaction between the polymer matrix and fibre reinforcement is highlighted as potentially changing significantly due to the onset of a transcrystalline layer. Chen<sup>[21]</sup> has examined various systems and demonstrated that the transcrystalline layer increases the

fibre-matrix interfacial bond strength, though the effect became less obvious as the fibre content increased in a composite. Similar positive results have also been reported in most related works of other researchers<sup>[17-20]</sup>, although several reports indicate a decrease in the fibre-matrix bonding from transcrystallinity<sup>[22-23]</sup>. The transcrystallinity is expected to affect the mechanical properties of the matrix as well due to the high dependence of polymer properties on the degree of crystallinity.<sup>[286-288]</sup> Therefore, the influence of transcrystallinity on the matrix itself has been investigated through AFM nanoindentation prior to the overall composite mechanical properties. The modification of matrix properties due to the effect of transcrystallinity has also been considered. Privako<sup>[206]</sup> examined the mechanical properties of polycarbonate that incorporated microcrystallinity, but the degree of crystallinity in their experiment was too low to present an obvious difference from the amorphous phase. Other available reports on the effects of crystallization on the mechanical properties of pure polycarbonate<sup>[207-208]</sup> have contradictory conclusions, leading to requirements for further investigation into the mechanical properties of crystallized polycarbonate.

In this work, attempts to form polycarbonate transcrystalline layer on the surface of electrospun alumina nanofibres are explored. The influences of both alumina nanofibre content to evaluate the nucleating surface area and annealing time on formation of transcrystallinity are studied through examining the thermal behaviour of the resultant polycarbonate composites. The morphology of the transcrystalline interface is evaluated both by scanning electron microscopy (SEM) and atomic force microscopy (AFM). The relationship between mechanical properties of both the matrix and the overall composite and formation of a transcrystalline layer are investigated by nanoindentation and tensile testing.

## 7.2 Materials and methods

### 7.2.1 AF/PC composite fabrication

The composites of polycarbonate reinforced with alumina nanofibre were prepared using randomly oriented alumina nanofibre mats fabricated through electrospinning following previous work<sup>[69]</sup>. The electrospun alumina nanofibre mats were placed in chloroform and dispersed in a high power ultrasonic bath (USC200T, VWR) for 1 h to form a suspension. Pure polycarbonate particles were added into the suspension and stirred until the polycarbonate was dissolved. The solution was stirred during the whole process to improve dispersion of the fibres in the composites. A range of weight ratios of alumina nanofibre and polycarbonate (ranging from 1:99 to 1:9) were used to obtain composites with different fibre concentrations. The solvent in the suspension was evaporated by heating to produce a solid composite structure. The mixture was further dried in a vacuum oven at 80 °C overnight. Afterwards, the composite was hot pressed at 250 °C with a pressure of 60 MPa to remove voids as well as form regular shapes (0.07 mm × 1.5 mm × 15 mm) with self-made model for subsequent microtensile testing. The samples were then cooled to 190 °C immediately following annealing under the same pressure for maintaining flat surface of the composite. Different annealing time intervals ranging from 4 h to 72 h were applied to investigate the potential to form transcrystallinity within the composite. Two series of polycarbonate composites containing 5 wt% (5W-AF/PC) and 10 wt% (10W-AF/PC) of alumina nanofibres were fabricated for comparing the influence of fibre content on the transcrystallization of polycarbonate.

## 7.2.2 Thermal characterization

Thermal behaviour of the composites after annealing were studied by typical differential scanning calorimetry (DSC, DSC 4000, PerkinElmer) with a heating rate of  $10\text{ }^{\circ}\text{C}\cdot\text{min}^{-1}$ . Nitrogen was used as purge gas with a flow rate of  $20\text{ ml}\cdot\text{min}^{-1}$ .

## 7.2.3 Imaging methods

Scanning electron microscopy (SEM) and atomic force microscopy (AFM) were used for morphology observation of the composite cross-section as well as the surface.

### 7.2.3.1 SEM imaging

For direct observation of the cross-section through SEM (Inspect F, FEI), composites were quenched in liquid nitrogen and then quickly broken above the surface of liquid nitrogen. Fracture surface of composite after being annealed for 24 h was also observed through SEM and the sample was prepared by breaking the composite directly by a small force. The sample was very brittle after annealing for 24 h, and can be broken easily. A thin layer of gold was coated on each sample before observing in SEM by a sputter coating equipment (Automatic sputter coater, Agar Scientific) to avoid charging effect.

### 7.2.3.2 AFM phase imaging

An atomic force microscopy (AFM, NT-MDT NTEGRA) with single crystal silicon cantilevers (Aspire CT300, Nanoscience instruments) were used for surface structure scanning as well as later nanoindentation. The surface of the AF/PC nanocomposites used for AFM investigations needs to be relatively flat to ensure effective imaging and later accurate measurement of Young's modulus of matrix.<sup>[289]</sup> AF/PC composite surfaces



were therefore prepared by spin coating a solution of polycarbonate and alumina nanofibre dispersed in chloroform (AF:PC =1:99 in weight ratio) onto a glass slide. The low concentration of alumina nanofibre in solution was used in this experiment to give a clear observation of the influence of individual nanofibres without interfering each other. The glass slides were then annealed at 190 °C for 12 h and 24 h respectively for observing the developing process of the crystallization. Phase imaging was performed on both samples surfaces using semi-contact model.

## **7.2.4 Mechanical testing**

### 7.2.4.1 AFM nanoindentation

Measurement of the Young's modulus of crystallized polycarbonate was conducted by nanoindentation with contact model on the AF/PC composite spin coated on the glass slide and annealed for 24 h. The spring constant of the probes used for nanoindentation are approximately 40 N·m<sup>-1</sup> but were calibrated with the thermal noise method<sup>[228]</sup> before each nanoindentation testing for later force calculation. After surface scanning, the nanoindentation was performed by moving the AFM probe into the sample surface using the piezo-positioners of the AFM. The AFM cantilever deflected during the translation of the AFM probe into the sample, with the cantilever displacement recorded by a position sensitive photo-diode<sup>[229]</sup> together with the z-piezo positioner displacement. After indentation, the conversion from photodiode current (nA) to cantilever deflection (nm) was calibrated and determined using a sapphire sheet, assuming that the sheet only displays a purely elastic response. The unloading curves representing retracing of the probe were used to calculate the elastic properties. Hooke's law was applied to calculate the force with the equation:  $F=k \cdot d$  ( $k$ , calibrated cantilever spring constant;  $d$ , the cantilever deflection). The AFM probe used in this study has a cone shape, and the contact

between the probe and the composite film then can be regarded as axisymmetric. By assuming the crystallized polycarbonate is isotropic and the AFM probe is non-deformable, all the above information was then translated to force-displacement curve using Hertzian model<sup>[230-231]</sup> developed by Sneddon<sup>[290]</sup> to calculate the Young's modulus of the sample using:

$$F = (2E^* / \pi) \cdot \tan \alpha \cdot h^2 \quad (7-1)$$

$$1/E^* = (1 - \nu_r^2)/E_r + (1 - \nu_s^2)/E_s \quad (7-2)$$

Where  $F$  is the loading force,  $h$  is the penetration depth of the indenter into the sample and  $\alpha$  is the semi-opening angle of the AFM probe tip,  $E^*$  is the reduced Young's modulus of the indenter-sample system,  $E$  is the Young's modulus,  $\nu$  is the Poisson's ratio, and the subscript  $r$  and  $s$  represent the indenter and the sample, respectively. A glass slide covered with a thin film of pure polycarbonate with known Young's modulus (value provided by the company and verified by conventional tensile testing) has also been prepared as a reference sample through spin coating of pure polycarbonate solution dissolved in chloroform. After nanoindentation on the amorphous polycarbonate, the equation (7-1) and (7-2) were fitted to the unloading curve of indentation performed on amorphous polycarbonate to calculate the accurate probe cone angle  $\alpha$ . Young's modulus of crystallized polycarbonate can then be calculated by fitting both equations with the calibrated probe cone angle to the unloading curve obtained from nanoindentation on the sample annealed for 24 h.

#### 7.2.4.2 Microtensile testing of composites

Microtensile test of AF/PC composites were conducted with a tensile stage (Microtest 200N tensile stage, Deben UK). Composite samples with a dimension of 0.07 mm  $\times$  1.5 mm  $\times$  15 mm were fixed between the two grips of the tensile stage before testing. The

samples were then tensile tested at a rate of  $0.2 \text{ mm}\cdot\text{min}^{-1}$  until the composites failed. The force applied to the sample and the resultant sample displacement were recorded and converted to stress-strain curves.

## **7.3 Results and discussion**

### **7.3.1 Thermal behaviour of polycarbonate reinforced with alumina nanofibres after annealing**

The composite of polycarbonate reinforced with randomly oriented alumina nanofibres were annealed at  $190 \text{ }^\circ\text{C}$  for successively increasing time intervals to study the influence of alumina nanofibres on crystallinity behaviour of polycarbonate. Two series of composites (composites 5W-AF/PC and 10W-AF/PC) were used to evaluate the influence of different amount of fibres.  $190 \text{ }^\circ\text{C}$  was chosen as the annealing temperature because polycarbonate has the fastest crystallization rate under this circumstance<sup>[291-292]</sup>, and thus the impact of nanofibres can be maximized.

The endothermic curves of composites 5W-AF/PC and 10W-AF/PC annealed for different times are shown Figure 7.1a and Figure 7.1b, respectively. For both series of composites, the endothermic peaks grow gradually with increased annealing time and two peaks can be identified for each sample. The higher endothermic peaks that appeared around  $229 \text{ }^\circ\text{C}$  are linked to the melting of primary crystallization, which is associated to the growth of spherulites, and these peaks are fixed at the same temperature regardless of the annealing time. While the lower endothermic peaks at around  $210 \text{ }^\circ\text{C}$  are attributed to the second isothermal crystallization during annealing<sup>[199]</sup> rather than the common mechanism of chain folding lamellar growth, these peaks are noticed to shift towards

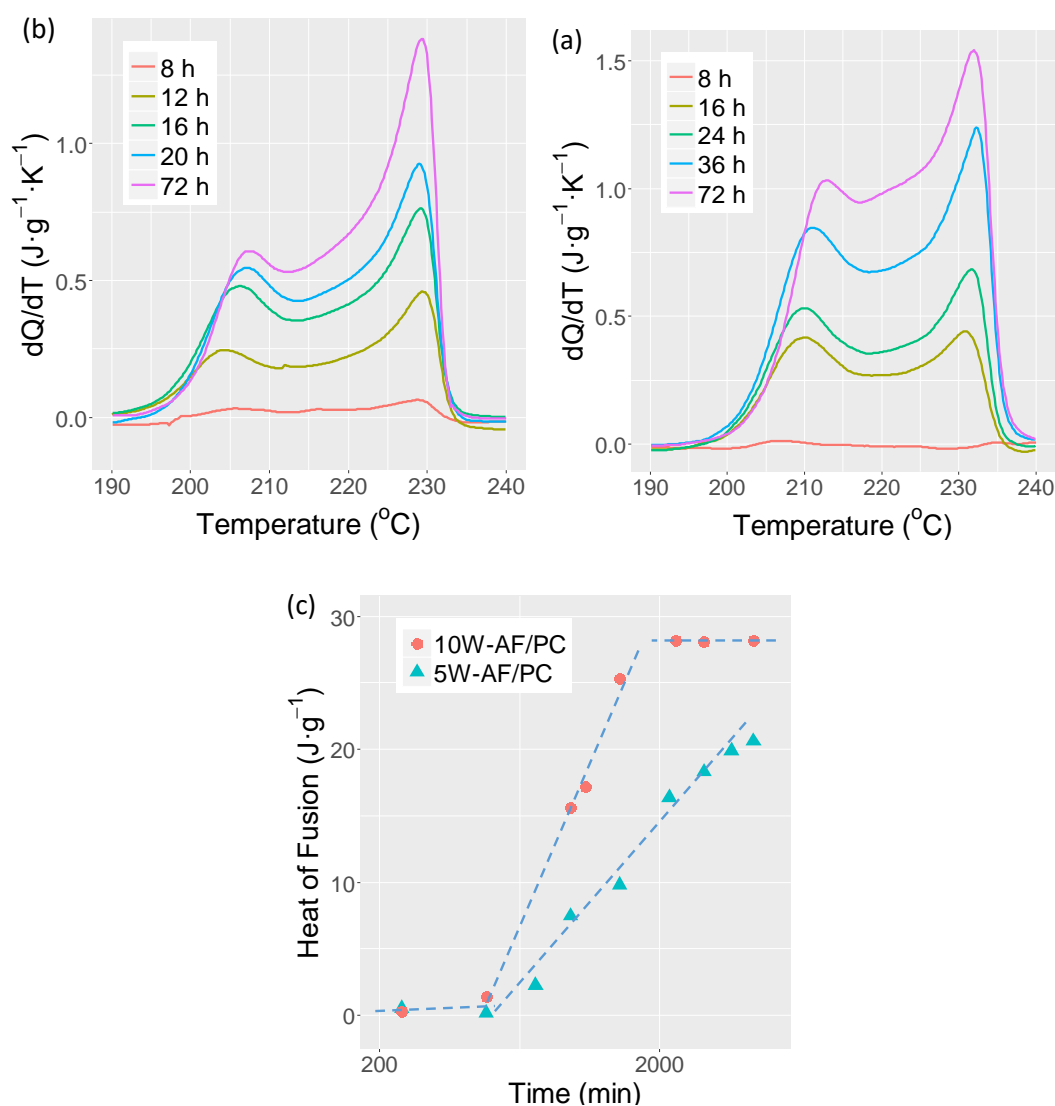


**Figure 7.1.** The endothermic curves of (a) 5W-AF/PC composites and (b) 10W-AF/PC composites after annealing at 190 °C for different time; (c) Heat of fusion change of both composites 5W-AF/PC and 10W-AF/PC after annealing at 190 °C.

higher temperature when the annealing time increases. The main cause for this shift is the decrease of the free energy of secondary crystals with increased annealing time, particularly the increase in the lateral dimensions of the crystals during secondary crystallization.<sup>[293]</sup> The endothermic peaks of these samples are similar to the pure polycarbonate annealed under 185 °C for 680 h (heat of fusion = 26  $J \cdot g^{-1}$ , peaks = 229 (strong), 210 (weak) °C).<sup>[198]</sup> Though both composite series have similar endothermic curves shapes, differences can be observed. Specifically, composite 10W-AF/PC has a

larger peak area difference between the higher and the lower endothermic peaks than that of composite 5W-AF/PC, which indicates that in composite with higher fibre content, higher percentage of polycarbonate crystallinity come from primary crystallization. The position of the lower peaks for composite 10W-AF/PC are also shifted to left compared to composites 5W-AF/PC because of lateral dimensions of the crystals formed in secondary crystallization are restricted by the larger amount of spherulites formed during primary crystallization, resulting in increased free energy. These differences confirm that the nanofibres mainly promote the primary crystallization, thus less secondary crystallization process occurs due to the limited polycarbonate crystallinity, leading to a smaller peak area for the lower endothermic peak.

The intensities of the endothermic peaks for both composite series grow with the increase of the annealing time, and the growth experiences three phases as reflected in Figure 7.1c. For example, the increase of heat of fusion for 10W-AF/PC depending on annealing time can be divided into three stages: as the annealing time increases, the heat of fusion firstly experiences a slow climb between 0 h to 8 h, then a sharp upward increase from 8 h to 24 h, and finally an almost horizontal line after 24 h. This phenomenon indicates that the crystallization rate of polycarbonate varies during different annealing period. In the first stage, the crystallization of polycarbonate experiences a relatively long induction time before the speed accelerates, which indicates nucleation of polycarbonate on the fibre surface. A small heat of fusion can be identified after annealing for 8 h for both composites 10W-AF/PC and 5W-AF/PC, representing a low degree of crystallinity for polycarbonate. As annealing continues, the heat of fusion starts to grow with a much faster speed. The larger slope of the line for composite 10W-AF/PC in Figure 7.1c demonstrates that the more fibre content, the faster crystallization speed. For composite 10W-AF/PC, the increase of heat of fusion reaches an upper limit of  $28.1 \text{ J}\cdot\text{g}^{-1}$  after being

annealed for more than 24 h, and the heat of fusion then stays at constant even if the annealing continues. The final crystallinity degree of polycarbonate in composite 10W-AF/PC was calculated by dividing the heat of fusion of fully crystallized polycarbonate by the measured value using a heat of fusion of  $109.7 \text{ J}\cdot\text{g}^{-1}$  for 100% crystallized polycarbonate<sup>[294]</sup>, is 25.7%. The composite 5W-AF/PC exhibits a similar induction time as composite 10W-AF/PC, as indicated by the dash line in Figure 1c. This is reasonable, since the nucleation time depends mainly on the surface properties of the matrix and the fibre rather than the fibre content. After the induction period, the difference between these two composites series starts to appear. As the 10W-AF/PC composite has nearly doubled nucleation sites, thus it shows a much faster crystallization speed and reaches the crystallization limit much quicker as well, confirming the promotion effect of alumina nanofibres on polycarbonate crystallization.

### **7.3.2 Morphology of crystallized polycarbonate**

Direct observation of the morphological changes of the polycarbonate before and after development of the transcrystalline layer, both the cross-section and the surface of the composites are provided using SEM and AFM.

The cross-section of the composite without annealing is presented in Figure 7.2a, and obvious gaps between the fibres and the matrix can be observed, demonstrating a poor interfacial bonding. In contrast, after annealing for only 0.5 h, the morphology of the fibre/matrix interface has changed significantly (see Figure 7.2b). The matrix is observed to crystallize around the fibres with a diameter around  $0.8\text{-}1.4 \mu\text{m}$  and no gap between the fibres and the matrix can be observed, demonstrating improved fibre/matrix bonding. The cone shape of the crystallized polycarbonate around the fibres indicates radial growth of the polycarbonate lamellar crystals. The polycarbonate spherulites grow independently

until impinging with each other when the annealing time raised to 24 h (see Figure 7.2c), forming thick boundaries as well as voids, which may be caused by the internal stress formed during crystallization. The fracture surface of showing fibres covered by a thick layer of matrix after the composite fractured is displayed in Figure 7.2d. The covered thick matrix phase demonstrates that either the fibre/matrix bonding strength is higher than strength of the matrix itself or the strength of the matrix has been reduced significantly by the voids formed during polycarbonate crystallization. Therefore, the effect of transcrystalline layer on mechanical properties of the composite need to be investigated further.

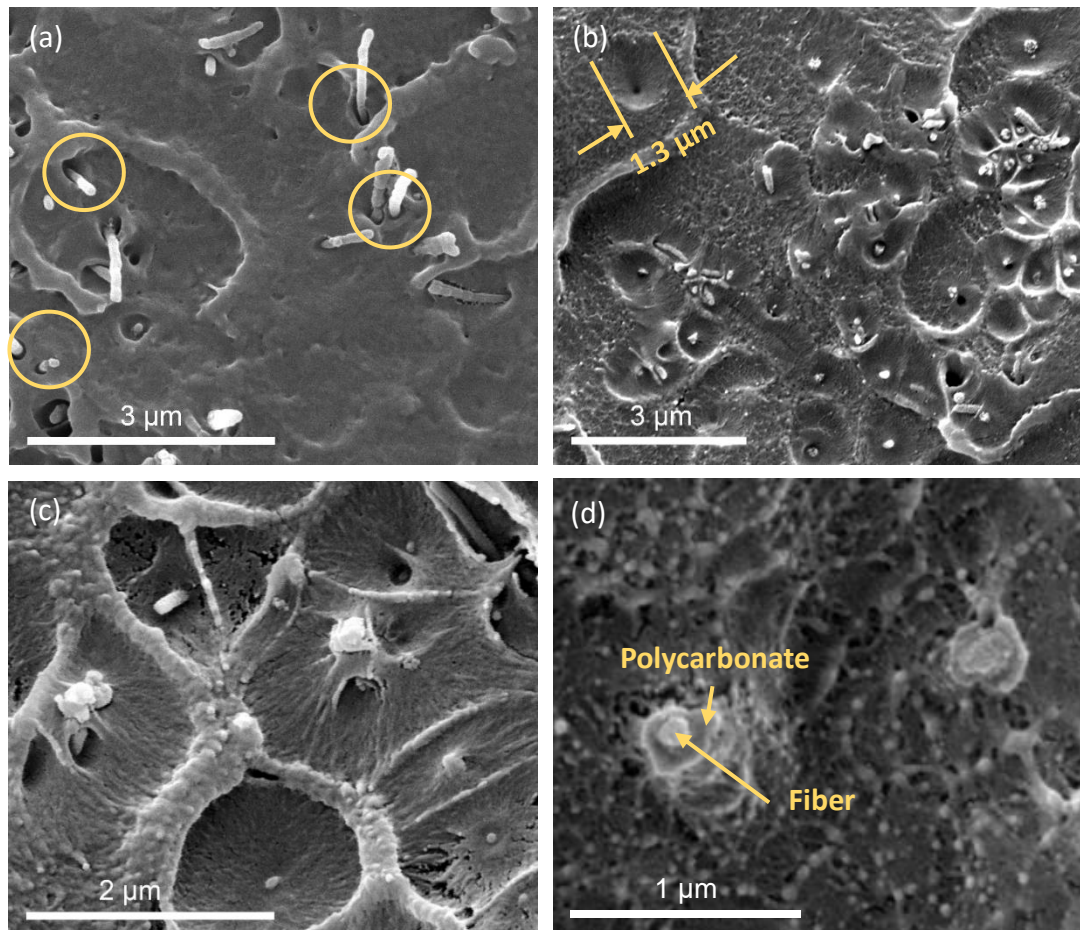


**Figure 7.2.** Scanning electron microscopy images show cross-section of AF/PC composites (a) without annealing, after annealing at 190 °C for (b) 0.5 h, (c) 24 h and (d) 24 h, respectively. Sample shown in (a) (b) (c) were prepared by broken in liquid nitrogen, while sample shown in (d) was broken by hand at room temperature.

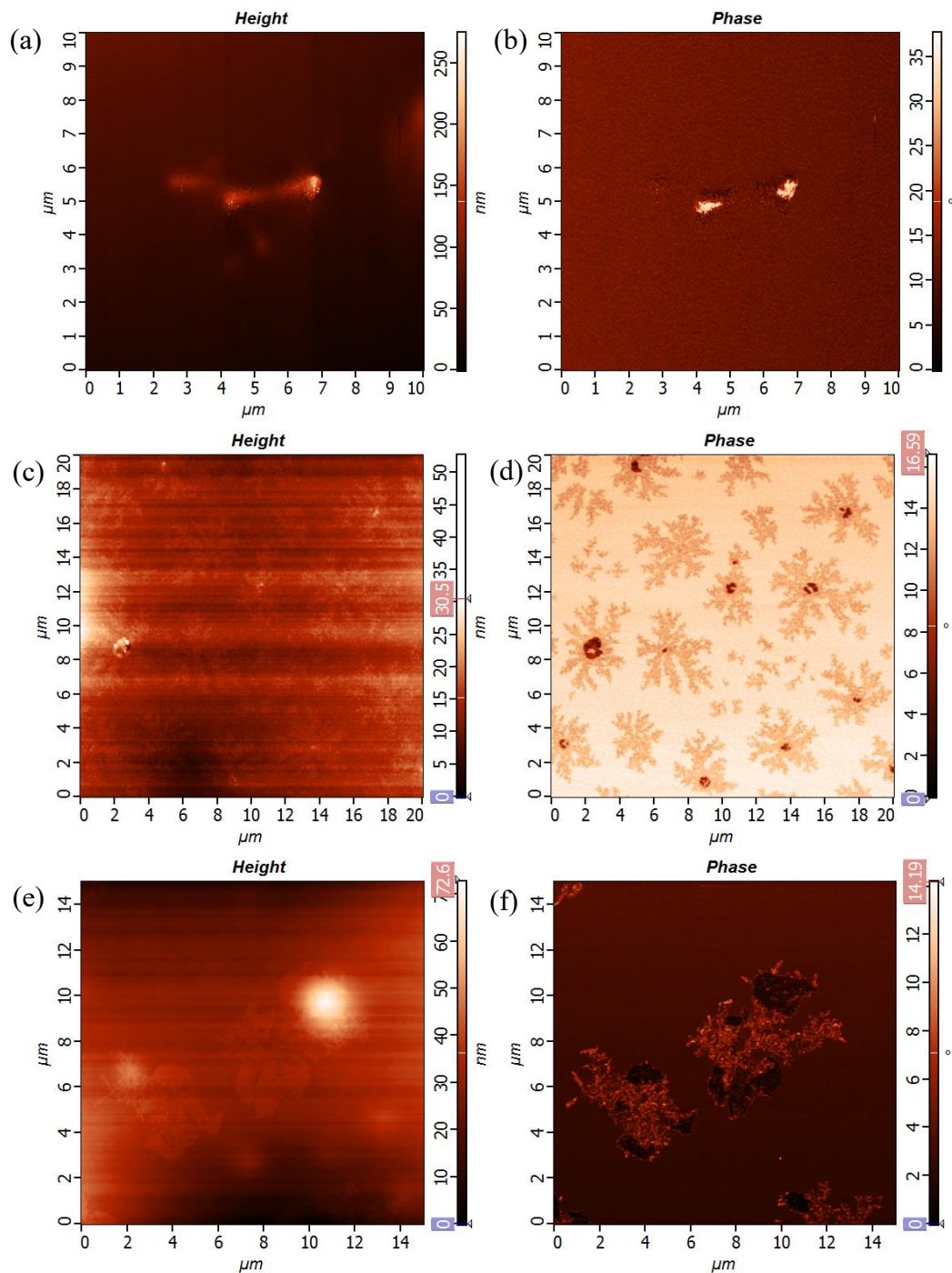


**Figure 7.3.** AFM topographic image (a) and phase image (b) of polycarbonate composite reinforced with 1 wt% alumina nanofibres before annealing. AFM topographic image (c) (e) and phase image (d) (f) of the same composite annealed at 190 °C for 12 h and 24 h, respectively.

Phase contrast imaging of AF/PC composites annealed at 190 °C for 0 h, 12 h and 24 h are obtained to give a clear growth process of polycarbonate crystalline lamellar and



prepare for measurement of Young's modulus of crystallized polycarbonate through AFM nanoindentation. Observations of the transcrystallinity of polycarbonate developed around the fibres are shown in Figure 7.3. For the sample without annealing, the matrix around the fibres are uniform without apparent phase difference. After annealing for 12 h, the phase image clearly shows polycarbonate crystallized around the alumina fibres, forming snowflake patterns (see Figure 7.3c and 7.3d). This pattern demonstrates that the crystallization behaviour of polycarbonate started from the fibre surface and then grew gradually and branched out. The average thickness for the polycarbonate crystalline lamellar is around 2  $\mu\text{m}$ . When the annealing time was doubled to 24 h, the dimension of the crystallites did not change greatly, but the snowflake like texture disappeared and branching grew into denser structures. This densification process is corresponding to the secondary crystallization process, which occurs between the materials trapped between the spherulites developed from the primary crystallization.<sup>[295]</sup>

### **7.3.3 Mechanical properties**

#### **7.3.3.1 Young's modulus of crystallized polycarbonate**

Young's modulus of crystallized polycarbonate has been measured through AFM nanoindentation on the sample annealed at 190 °C for 24 h. During the nanoindentation, the bending of the probe and displacement of the cantilever were then recorded and interpreted into the force-displacement curves as displayed in Figure 7.4. The unloading curves of indentation performed on both amorphous polycarbonate with known Young's modulus and crystallized polycarbonate were fitted with equation (7-1) and (7-2) to calculate the Young's modulus of crystallized polycarbonate. The nanoindentation testing has been repeated several times at different areas on each sample. Overall, the Young's modulus of the crystallized polycarbonate measured on composites annealed for 24 h is

7.07±0.46 GPa. Direct measurement of crystallized polycarbonate has rarely been reported previously. Conix<sup>[204]</sup> has calculated the Young's modulus of crystallized polycarbonate following Dulmage's theory<sup>[209]</sup>, and the result is in the range of 9.80-19.6 GPa. The calculation is based on the assumption that the polymer chains crystalline regions are fully extended, while in reality the polymer is a mixture of crystallized and amorphous phase, which may be the reason for the relatively low modulus for the experimental value.

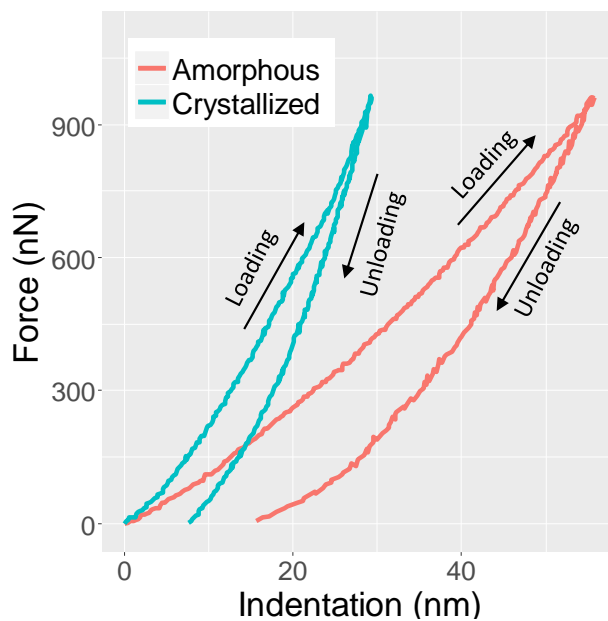


**Figure 7.4. Force-displacement curves of amorphous and crystallized polycarbonate.**

### 7.3.3.2 Influence of transcrystallinity of the composite mechanical properties

The effect of transcrystallinity on the overall composite properties is evaluated through tensile testing of composite 5W-AF/PC annealed at 190 °C for successively increasing time intervals and the results are summarized in Figure 7.5. Representative stress-strain curves for the composites are displayed in Figure 7.5a. The sample without annealing has relatively low tensile strength and Young's modulus but a large breaking strain, which is similar with pure polycarbonate. After being annealed for 8 h, both the tensile strength

and Young's modulus increased significantly. However, both the strength and the Young's modulus decreased slightly when the annealing time doubled to 16 h. The strength loss is much more severe for sample annealed for 24 h and the Young's modulus dropped to almost the same value as before annealing. The breaking strain of the composite decreases consistently with increased annealing time, due to the continuously raising polycarbonate crystallinity.

The dependence of the composite strength and Young's modulus on annealing time is more clearly revealed in Figure 7.5b and Figure 7.5c. The tensile strength and Young's modulus of the composite annealed for 8 h has increased by 20% and 43% respectively, compared with the sample without annealing. According to Figure 7.1, the polycarbonate crystallinity is still at a low level after annealing for such a short time, thus the increase of Young's modulus of polycarbonate is negligible and the main reason for this mechanical properties elevation is attributed to the improved fibre/matrix bonding. As the annealing time continued to increase, the mechanical performance started to deteriorate and the sample also became more and more brittle. The Young's modulus of the composite decreased significantly despite of the increased Young's modulus of the matrix. The optimal annealing time for enhancing mechanical properties of AF/PC composite is around 8 h, which is very close to the induction time for polycarbonate crystallization, as shown in Figure 1c. Therefore, transcrystallization shows a positive effect for enhancing the mechanical properties of AF/PC composite. However, the improvement is limited by the negative effect of the crystallization of polycarbonate.

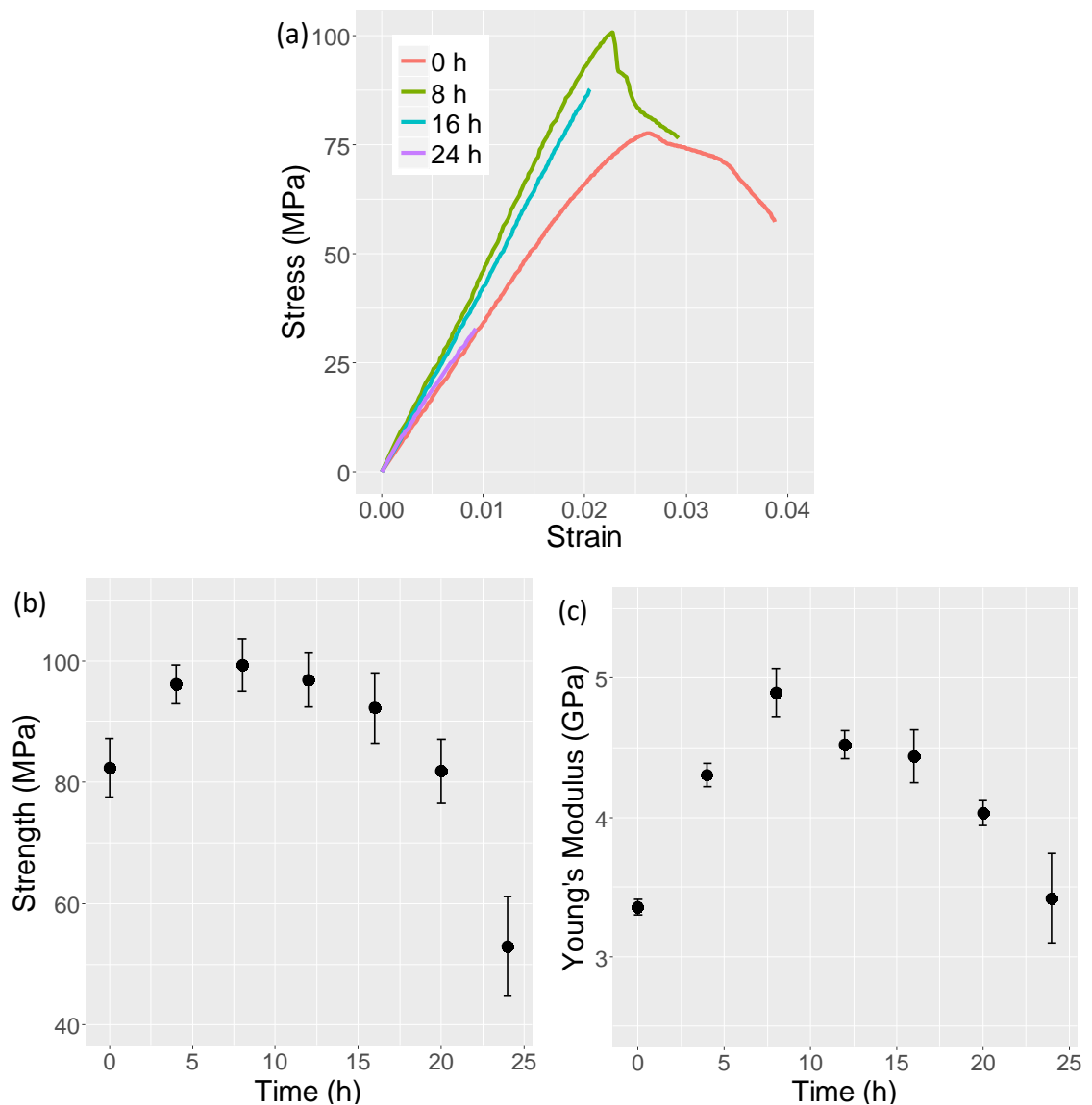


**Figure 7.5.** (a) Stress-strain curves, (b) tensile strength and (c) Young's modulus of 5W-AF/PC composites after annealing at 190 °C for different time.

## 7.4 Conclusions

In this chapter, polycarbonate composites reinforced with randomly oriented alumina nanofibre have been annealed at 190 °C for successively increasing time intervals to explore the influence of transcrystallization on the composite mechanical properties. Both the SEM images of the composite cross-section and the AFM phase contrast images of the composite surface confirmed the formation of the transcrystalline layer of

polycarbonate around the nanofibres after annealing. After an induction time of around 8 h, the polycarbonate crystallinity grew gradually with increased annealing time until reaching the limitation around 26%. Two endothermic peaks can be identified from the DSC curves of each sample. One is related to the primary crystallization while the other one is for secondary crystallization. Significant enhancement of the Young's modulus of the crystallized polycarbonate by a factor of 3 compared to the amorphous phase was measured directly using AFM based nanoindentation. Both the SEM images and the tensile testing of the composites confirmed that the transcrystalline layer can enhance the fibre/matrix bonding, thus has a positive effect for improving the composite properties. However, the improvement is limited by the voids developed in the matrix during polycarbonate crystallization. As a result of the combined effect of the transcrystalline layer, the optimal annealing time for AF/PC composite with improved mechanical properties is 8 h, the same as the induction time of polycarbonate crystallization.

## 8 Conclusions and future work

### 8.1 Conclusions

This dissertation examines the fabrication and characterization of both electrospun alumina nanofibres and their mechanical function as a reinforcement in polycarbonate composites. Various fabrication and characterization methods have been involved in this work and the primary results are summarized as following:

1. Both polycrystalline  $\gamma$ -alumina nanofibres and single crystal  $\alpha$ -alumina fibres have been successfully fabricated and three different crystal structures:  $\gamma$  (cubic),  $\delta$  (orthorhombic), and  $\alpha$  (rhombohedral) were found to be involved in the process of fibre growth and mechanisms including the epitaxial growth, the screw dislocation growth and the template grain growth were applied to explain the inconsistent fibre growth directions. The strength of  $\gamma$ -alumina nanofibres shows significant diameter dependence and increase steadily from 2.0 GPa to 6.3 GPa as fibre diameters decreased from 135 nm to 75 nm. The strength of  $\alpha$ -alumina fibres is consistent at around  $11.4 \pm 1.1$  GPa across all the fibre diameters considered and exhibits a single crystal structure. The strength of both electrospun nanofibres using the calcination processes detailed provide increased tensile strength compared with high performance industrial alumina nanofibres currently in use, showing significant potential for further application in industry.

2. Polycarbonate composites reinforced with aligned alumina nanofibres were fabricated and a range parameters affecting the composite mechanical properties were investigated. The results prove that the introduction of surfactant has successfully improved the composite mechanical properties. However, despite composite strength increasing with increasing volume fractions when the fibre volume fraction is low, the composite containing higher fibre volume fractions exhibits a degradation in mechanical performance. The possible reason for this phenomenon was proposed as due to resistance of the higher fibre volume fraction to spreading of the PC melt, causing void formation in the composite during hot pressing and impairing the composite's mechanical performance. The two theoretical models based on the Halpin-Tsai equation and shear lag model provide a reasonable estimation of the composite Young's modulus at low fibres volume fractions, but overestimated the modulus when the fibre volume fraction exceeded around 7% due to the increased amount of defects not considered in the models.

3. Formation of transcrystalline layers in polycarbonate nanocomposites reinforced with electrospun alumina nanofibres using annealing methods was studied. The typically amorphous polycarbonate produced transcrystalline regions occupying volumes of up to 26% around the fibre surfaces as confirmed with differential scanning calorimetry and AFM phase contrast imaging. Significant enhancement of the Young's modulus of the crystallized polycarbonate by a factor of 3 compared to the amorphous phase was measured directly using AFM based nanoindentation. Optimization of the Young's modulus is suggested as a balance between extending the annealing time to grow the transcrystalline layer and reducing the processing time to suppress void development in the polycarbonate matrix.

## 8.2 Future work

The high mechanical performance of the alumina nanofibres and the significant potential of these fibres as reinforcements in the composite market has been demonstrated in this work. These positive results lead to a motivation to maximize the advantage of extraordinary products by further exploration into the following aspects:

1. Direct observation of crystal structure transformation from  $\delta$ -alumina to  $\alpha$ -alumina:

In chapter 4, alumina nanofibres containing both  $\gamma$  phase and  $\delta$  phase has been observed. The  $\delta$  grains quickly transformed to  $\alpha$  phase as calcination continued, leading to fibres containing both  $\gamma$  phase and  $\alpha$  phase instead of fibres containing both  $\delta$  phase and  $\alpha$  phase. Therefore, no direct evidence to support the speculated crystal structure transformation mechanism from  $\delta$  phase to  $\alpha$  phase (as explained in section 4.3.4) has been observed. *In situ* transmission electron microscopy with high temperature heating holder provides the opportunity to directly observe the transformational mechanism. This promising observation would strengthen the current theory of alumina crystal structure transformation mechanism and help to have a better understanding of the fibre growth directions.

2. Tensile testing of polycrystalline  $\gamma$ -alumina nanofibres with smaller diameters:

The strength of the polycrystalline nanofibres increases with the decreasing fibre diameters according to results in chapter 5. A straight line is fitted to the strength of polycrystalline alumina nanofibres versus the fibre diameters (see Figure 8.1), showing the polycrystalline fibre strength tends towards the strength of single crystal fibres if the fibre diameter is small enough. Additionally, according to Gao<sup>[296]</sup>, when the material size



is smaller than a critical value, the sample would be insensitive to the flaws and behave as ideal materials. Therefore, tensile testing of polycrystalline nanofibres with much smaller fibre diameters would be an interesting area to explore the dependence of the polycrystalline fibre strength on diameters further. Fabricating the polycrystalline  $\gamma$ -alumina nanofibres with diameters below 75 nm is possible by manipulating the concentrations of the polymer and alumina precursor in the electrospinning solution. If the above assumption can be proved, the shortened calcination time for fabricating polycrystalline nanofibres is likely to save more energy compared to fabrication of single crystal nanofibres.

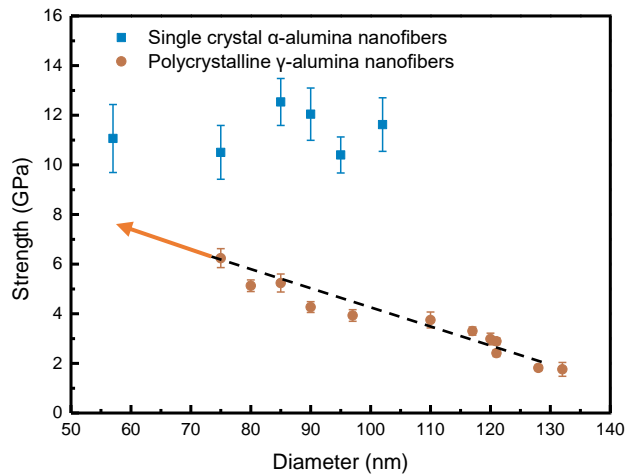


**Figure 8.1. Dependence between alumina nanofibre strength and fibre diameter with linear fitting.**

### 3. Fabricating composites with increased fibre volume fraction and less voids:

Increased fibre volume fraction would enhance the composite mechanical properties significantly in ideal conditions according to the Halpin-Tsai's theory. However, the composite fabrication method used in this work introduces more voids as the fibre volume fraction increased. To avoid this problem, new techniques to fabricate polymer matrix composites with aligned alumina nanofibres could be introduced, such as using hot

pressing assisted by vacuum system. Another possible way is to try to fabricate tight alumina fibre bundle with less spacing between individual fibres. Such an outcome would produce a composite with mechanical properties that rival current high performance composite materials but exploit cheaper materials and milder processing conditions used for the alumina nanofibres.

## Reference

- [1] Herakovich, C. T., *Mechanics Research Communications* **2012**, *41*, 1-20.
- [2] Mitchell, B. S., *An introduction to materials engineering and science for chemical and materials engineers*. John Wiley & Sons: 2004.
- [3] La Mantia, F. P.; Morreale, M., *Composites Part A: Applied Science and Manufacturing* **2011**, *42* (6), 579-588.
- [4] Jain, R.; Vaidya, U. K.; Haque, A., *Adv. Compos. Mater* **2006**, *15* (2), 211-241.
- [5] Xu, X.; Xu, H. H., *Dental Composites Reinforced with Ceramic Whiskers and Nanofibers*. In *Handbook of Nanomaterials Properties*, Springer: 2014; pp 1299-1320.
- [6] Donnet, J.-B., *Carbon fibers*. CRC Press: 1998.
- [7] Iijima, S., *nature* **1991**, *354* (6348), 56-58.
- [8] Salvétat, J.-P.; Bonard, J.-M.; Thomson, N.; Kulik, A.; Forro, L.; Benoit, W.; Zuppiroli, L., *Appl. Phys. A* **1999**, *69* (3), 255-260.
- [9] Pokluda, J.; Černý, M.; Šandera, P.; Šob, M., *J. Comput. Aided Mater. Des.* **2005**, *11* (1), 1-28.
- [10] Wilson, D.; Visser, L., *Compos. Part A: Appl. Sci. Manuf.* **2001**, *32* (8), 1143-1153.
- [11] Soltis, P. J. *Anisotropic Mechanical Behavior in Sapphire (Al2O3) Whiskers*; Naval Air Engineering Center: 1964.
- [12] McColm, I., *Ceramic science for materials technologists*. Chapman & Hall UK, 1983.
- [13] Sharma, M.; Gao, S.; Mäder, E.; Sharma, H.; Wei, L. Y.; Bijwe, J., *Compos. Sci. Technol.* **2014**, *102*, 35-50.
- [14] Karger-Kocsis, J.; Mahmood, H.; Pegoretti, A., *Prog. Mater Sci.* **2015**, *73*, 1-43.
- [15] Plueddemann, E. P., *Interfaces in Polymer Matrix Composites: Composite Materials*. Elsevier: 2016; Vol. 6.
- [16] Kulshreshtha, A. K., *Handbook of polymer blends and composites*. iSmithers Rapra Publishing: 2002; Vol. 1.

- [17] Quan, H.; Li, Z.; Yang, M.; Huang, R., *Compos. Sci. Technol.* **2005**, *65* (7), 999-1021.
- [18] Nagae, S.; Otsuka, Y.; Nishida, M.; Shimizu, T.; Takeda, T.; Yumitori, S., *J. Mater. Sci. Lett.* **1995**, *14* (17), 1234-1236.
- [19] Jeng, C.; Chen, M., *Compos. Sci. Technol.* **2000**, *60* (9), 1863-1872.
- [20] Felix, J.; Gatenholm, P., *J. Mater. Sci.* **1994**, *29* (11), 3043-3049.
- [21] Chen, E. J. H.; Hsiao, B. S., *Polym. Eng. Sci.* **1992**, *32* (4), 280-286.
- [22] Hagenson, R.; Register, D.; Soules, D. In Progress in Polyarylene Sulfide Resin/Fiber Interface, 34th International SAMPE Symposium and Exhibition, Nevada, USA, Zakrzewski, G., Ed. Nevada, USA, 1989; pp 2255-2265.
- [23] Garkhail, S.; Wieland, B.; George, J.; Soykeabkaew, N.; Peijs, T., *J. Mater. Sci.* **2009**, *44* (2), 510-519.
- [24] Hull, D.; Clyne, T., An introduction to composite materials. Cambridge university press: 1996.
- [25] Hu, H.; Onyebueke, L.; Abatan, A., *Journal of Minerals and Materials Characterization and Engineering* **2010**, *9*, 275.
- [26] Mallick, P. K., Fiber-reinforced composites: materials, manufacturing, and design. CRC press: 2007.
- [27] Kelly, A.; Tyson, a. W., *Journal of the Mechanics and Physics of Solids* **1965**, *13* (6), 329-350.
- [28] Manocha, L. M., *Sadhana* **2003**, *28* (1-2), 349-358.
- [29] Huang, Z.-M.; Zhang, Y. Z.; Kotaki, M.; Ramakrishna, S., *Compos. Sci. Technol.* **2003**, *63* (15), 2223-2253.
- [30] Dai, Y.; Liu, W.; Formo, E.; Sun, Y.; Xia, Y., *Polym. Adv. Technol.* **2011**, *22* (3), 326-338.
- [31] Bunsell, A. R.; Berger, M. H., *J. Eur. Ceram. Soc.* **2000**, *20* (13), 2249-2260.
- [32] Shi, D.; Lian, J.; He, P.; Wang, L. M.; Xiao, F.; Yang, L.; Schulz, M. J.; Mast, D. B., *Appl. Phys. Lett.* **2003**, *83* (25), 5301-5303.
- [33] Vaz, C. M.; Reis, R.; Cunha, A., *Biomaterials* **2002**, *23* (2), 629-635.
- [34] Sharma, Y. N.; Patel, R. D.; Dhimmarr, I. H.; Bhardwaj, I. S., *J. Appl. Polym. Sci.* **1982**, *27* (1), 97-104.
- [35] Gleich, K.; Grassl, T.; Wang, L. Gypsum boards with glass fiber reinforcements having a titanate or zirconate coupling coating. US 20060029785 A1, 2004.

- [36] Matinlinna, J. P.; Özcan, M.; Lassila, L. V.; Vallittu, P. K., *Dent. Mater.* **2004**, *20* (9), 804-813.
- [37] Griffith, A., *Phil. Trans. R. Soc. A* **1921**, *221*, 163-198.
- [38] Eckel, Z. C.; Zhou, C.; Martin, J. H.; Jacobsen, A. J.; Carter, W. B.; Schaedler, T. A., *Science* **2016**, *351* (6268), 58-62.
- [39] Inglis, C. E., *Spie Milestone series MS* **1997**, *137*, 3-17.
- [40] Li, D.; Xia, Y., *Nano Lett.* **2003**, *3* (4), 555-560.
- [41] Chen, C. Q.; Shi, Y.; Zhang, Y. S.; Zhu, J.; Yan, Y. J., *Phys. Rev. Lett.* **2006**, *96* (7), 075505.
- [42] Ramakrishna, S., An introduction to electrospinning and nanofibers. World Scientific: 2005.
- [43] Lee, S.-H.; Tekmen, C.; Sigmund, W. M., *Mater. Sci. Eng. A* **2005**, *398* (1-2), 77-81.
- [44] Ávila, H. A.; Ramajo, L. A.; Góes, M. S.; Reboredo, M. M.; Castro, M. S.; Parra, R., *ACS Applied Materials & Interfaces* **2013**, *5* (3), 505-510.
- [45] Guo, G.; Fan, Y.; Zhang, J.-F.; Hagan, J. L.; Xu, X., *Dent. Mater.* **2012**, *28* (4), 360-368.
- [46] Brunelle, D. J.; Smigelski Jr, P. M.; Boden, E. P., Evolution of polycarbonate process technologies. ACS Publications: 2005.
- [47] Skiens, W., *Radiation Physics and Chemistry (1977)* **1980**, *15* (1), 47-57.
- [48] Dhakate, S.; Singla, B.; Uppal, M.; Mathur, R., *Advanced Materials Letters* **2010**, *1* (3), 200-204.
- [49] Wouters, M.; Wolfs, D.; Van der Linde, M.; Hovens, J.; Tinnemans, A., *Prog. Org. Coat.* **2004**, *51* (4), 312-319.
- [50] Luyt, A. S.; Messori, M.; Fabbri, P.; Mofokeng, J. P.; Taurino, R.; Zanasi, T.; Pilati, F., *Polym. Bull.* **2010**, *66* (7), 991-1004.
- [51] Pandey, I.; Jain, A.
- [52] Chang, S.-H.; Hwang, J.-R.; Doong, J.-L., *J. Mater. Process. Technol.* **2000**, *97* (1), 186-193.
- [53] Tanimoto, Y.; Inami, T.; Yamaguchi, M.; Nishiyama, N.; Kasai, K., *Journal of Biomedical Materials Research Part B: Applied Biomaterials* **2015**, *103* (4), 743-750.
- [54] Ozkan, C.; Karsli, N. G.; Aytac, A.; Deniz, V., *Composites Part B: Engineering* **2014**, *62*, 230-235.

- [55] Fisher, F. T. Nanomechanics and the viscoelastic behavior of carbon nanotube-reinforced polymers. Northwestern University, 2002.
- [56] Pötschke, P.; Brünig, H.; Janke, A.; Fischer, D.; Jehnichen, D., *Polymer* **2005**, *46* (23), 10355-10363.
- [57] Threepopnatkul, P.; Kaerkitcha, N.; Athipongarporn, N., *Composites Part B: Engineering* **2009**, *40* (7), 628-632.
- [58] Park, J. M.; Chong, E. M.; Yoon, D. J.; Lee, J. H., *Polym. Compos.* **1998**, *19* (6), 747-758.
- [59] Carneiro, O. S.; Covas, J. A.; Bernardo, C. A.; Caldeira, G.; Van Hattum, F. W. J.; Ting, J. M.; Alig, R. L.; Lake, M. L., *Compos. Sci. Technol.* **1998**, *58* (3), 401-407.
- [60] Eitan, A.; Fisher, F. T.; Andrews, R.; Brinson, L. C.; Schadler, L. S., *Compos. Sci. Technol.* **2006**, *66* (9), 1162-1173.
- [61] Kumar, A., Nanofibers. InTech: 2010.
- [62] Ryshkewitch, E., *J. Am. Ceram. Soc.* **1953**, *36* (2), 65-68.
- [63] Shimazaki, Y.; Hojo, F.; Takezawa, Y., *Appl. Phys. Lett.* **2008**, *92* (13), 133309.
- [64] Zhu, H. Y.; Riches, J. D.; Barry, J. C., *Chem. Mater.* **2002**, *14* (5), 2086-2093.
- [65] Zhao, Y.; Frost, R. L.; Martens, W. N.; Zhu, H. Y., *Langmuir* **2007**, *23* (19), 9850-9859.
- [66] Wang, J.; Wang, Y.; Qiao, M.; Xie, S.; Fan, K., *Mater. Lett.* **2007**, *61* (28), 5074-5077.
- [67] Azad, A. M., *Mater. Sci. Eng. A* **2006**, *435-436*, 468-473.
- [68] Dai, H.; Gong, J.; Kim, H.; Lee, D., *Nanotechnology* **2002**, *13* (5), 674.
- [69] Yu, H.; Guo, J.; Zhu, S.; Li, Y.; Zhang, Q.; Zhu, M., *Mater. Lett.* **2012**, *74* (0), 247-249.
- [70] Larsen, G.; Velarde-Ortiz, R.; Minchow, K.; Barrero, A.; Loscertales, I. G., *J. Am. Chem. Soc.* **2003**, *125* (5), 1154-1155.
- [71] Panda, P. K.; Ramakrishna, S., *J. Mater. Sci.* **2007**, *42* (6), 2189-2193.
- [72] Kang, W.; Cheng, B.; Li, Q.; Zhuang, X.; Ren, Y., *Text. Res. J.* **2011**, *81* (2), 148-155.
- [73] Nakane, K.; Seto, M.; Irie, S.; Ogihara, T.; Ogata, N., *J. Appl. Polym. Sci.* **2011**, *121* (3), 1774-1779.
- [74] Liu, P.; Zhu, Y.; Ma, J.; Yang, S.; Gong, J.; Xu, J., *Colloids and Surfaces A: Physicochemical and Engineering Aspects* **2013**, *436* (0), 489-494.

- [75] Gupta, A.; Sharma, S.; Joshi, M. R.; Agarwal, P.; Balani, K. In Grain growth behavior of Al<sub>2</sub>O<sub>3</sub> nanomaterials: a review, *Mater. Sci. Forum*, Trans Tech Publ: 2010; pp 87-130.
- [76] Levin, I.; Brandon, D., *J. Am. Ceram. Soc.* **1998**, *81* (8), 1995-2012.
- [77] Santos, P. S.; Santos, H. S.; Toledo, S. P., *Materials Research* **2000**, *3*, 104-114.
- [78] Wefers, K.; Misra, C., *Oxides and Hydroxides of Aluminum*. Alcoa Research Laboratories: Pittsburgh, USA, 1987.
- [79] Teoh, G. L.; Liew, K. Y.; Mahmood, W. A. K., *J. Sol-Gel Sci. Technol.* **2007**, *44* (3), 177-186.
- [80] Yu, P. C.; Yang, R. J.; Tsai, Y. Y.; Sigmund, W.; Yen, F. S., *J. Eur. Ceram. Soc.* **2011**, *31* (5), 723-731.
- [81] Streitz, F. H.; Mintmire, J. W., *Physical Review B* **1999**, *60* (2), 773-777.
- [82] Lee, M. H.; Cheng, C.-F.; Heine, V.; Klinowski, J., *Chem. Phys. Lett.* **1997**, *265* (6), 673-676.
- [83] Antonaia, A.; Castaldo, A.; Addonizio, M.; Esposito, S., *Sol. Energy Mater. Sol. Cells* **2010**, *94* (10), 1604-1611.
- [84] Levin, I.; Bendersky, L.; Brandon, D.; Rühle, M., *Acta Mater.* **1997**, *45* (9), 3659-3669.
- [85] Lippens, B.; De Boer, J., *Acta Crystallographica* **1964**, *17* (10), 1312-1321.
- [86] Repelin, Y.; Husson, E., *Mater. Res. Bull.* **1990**, *25* (5), 611-621.
- [87] Jayaram, V.; Levi, C., *Acta Metall.* **1989**, *37* (2), 569-578.
- [88] Fargeot, D.; Mercurio, D.; Dauger, A., *Mater. Chem. Phys.* **1990**, *24* (3), 299-314.
- [89] Cai, S.-H.; Rashkeev, S. N.; Pantelides, S. T.; Sohlberg, K., *Phys. Rev. Lett.* **2002**, *89* (23), 235501.
- [90] Zhou, R.-S.; Snyder, R. L., *Acta Crystallogr. Sect. B: Struct. Sci.* **1991**, *47* (5), 617-630.
- [91] Dobrovinskaya, E. R.; Lytvynov, L. A.; Pishchik, V., *Sapphire: material, manufacturing, applications*. Springer Science & Business Media: 2009.
- [92] Chou, T. C.; Nieh, T. G., *J. Am. Ceram. Soc.* **1991**, *74* (9), 2270-2279.
- [93] Li, J. G.; Sun, X., *Acta Mater.* **2000**, *48* (12), 3103-3112.
- [94] Dragoo, A.; Diamond, J., *J. Am. Ceram. Soc.* **1967**, *50* (11), 568-574.
- [95] Shelleman, R. A.; Messing, G. L.; Kumagai, M., *J. Non-Cryst. Solids* **1986**, *82* (1), 277-285.
- [96] Wen, H.-L.; Yen, F.-S., *J. Cryst. Growth* **2000**, *208* (1-4), 696-708.

- [97] Gangwar, J.; Gupta, B. K.; Kumar, P.; Tripathi, S. K.; Srivastava, A. K., *Dalton Transactions* **2014**, 43 (45), 17034-17043.
- [98] Tsybulya, S. V.; Kryukova, G. N., *Powder Diffr.* **2003**, 18 (04), 309-311.
- [99] Webb, W. W.; Forgeng, W. D., *J. Appl. Phys.* **1957**, 28 (12), 1449.
- [100] Edwards, P. L.; Happel, R. J., *J. Appl. Phys.* **1962**, 33 (3), 826.
- [101] Song, K.; Wu, S.; Chen, X.; Qin, N., *J. Electroceram.* **2008**, 21 (1-4), 805-809.
- [102] Levi, C.; Abbaschian, G.; Mehrabian, R., *Metall. Trans. A* **1978**, 9 (5), 697-711.
- [103] Ramamurty, U.; Zok, F. W.; Leckie, F. A.; Dève, H. E., *Acta Mater.* **1997**, 45 (11), 4603-4613.
- [104] Michalske, T. A.; Hellmann, J. R., *J. Am. Ceram. Soc.* **1988**, 71 (9), 725-731.
- [105] Keller, K. A.; Mah, T.-I.; Parthasarathy, T. A.; Boakye, E. E.; Mogilevsky, P.; Cinibulk, M. K., *J. Am. Ceram. Soc.* **2003**, 86 (2), 325-332.
- [106] Bolt, J. D.; Button, D. P.; Yost, B. A., *Mater. Sci. Eng. A* **1989**, 109, 207-211.
- [107] Kim, B.-J.; Bae, K.-M.; An, K.-H.; Park, S.-J., *Bull. Korean Chem. Soc.* **2012**, 33 (10), 3258-3264.
- [108] Fu, J. F.; Shi, L. Y.; Zhong, Q. D.; Chen, Y.; Chen, L. Y., *Polym. Adv. Technol.* **2011**, 22 (6), 1032-1041.
- [109] Dudkin, B. N.; Zainullin, G. G.; Krivoshapkin, P. V.; Krivoshapkina, E. F.; Ryazanov, M. A., *Glass Phys. Chem* **2008**, 34 (2), 187-191.
- [110] Wu, H.; Pan, W.; Lin, D.; Li, H., *Journal of Advanced Ceramics* **2012**, 1 (1), 2-23.
- [111] Taylor, G., *Proceedings of the Royal Society of London. Series A. Mathematical and Physical Sciences* **1964**, 280 (1382), 383-397.
- [112] Li, D.; Xia, Y., *Adv. Mater.* **2004**, 16 (14), 1151-1170.
- [113] Zhang, C.; Yuan, X.; Wu, L.; Han, Y.; Sheng, J., *Eur. Polym. J.* **2005**, 41 (3), 423-432.
- [114] Koski, A.; Yim, K.; Shivkumar, S., *Mater. Lett.* **2004**, 58 (3), 493-497.
- [115] Sun, B.; Duan, B.; Yuan, X., *J. Appl. Polym. Sci.* **2006**, 102 (1), 39-45.
- [116] Wang, J.; Gao, Q.; He, H.; Li, X.; Ren, Z.; Liu, Y.; Shen, G.; Xu, G.; Zhang, X.; Han, G., *J. Alloys Compd.* **2013**, 579, 617-621.
- [117] Gupta, P.; Elkins, C.; Long, T. E.; Wilkes, G. L., *Polymer* **2005**, 46 (13), 4799-4810.
- [118] He, J.-H.; Wan, Y.-Q.; Yu, J.-Y., *Fibers and Polymers* **2008**, 9 (2), 140-142.
- [119] Pham, Q. P.; Sharma, U.; Mikos, A. G., *Tissue Eng.* **2006**, 12 (5), 1197-1211.



- [120] Zong, X.; Kim, K.; Fang, D.; Ran, S.; Hsiao, B. S.; Chu, B., *Polymer* **2002**, *43* (16), 4403-4412.
- [121] Hancock, W. S., *High Resolution Separation and Analysis of Biological Macromolecules: Fundamentals*. Elsevier: 1996.
- [122] Lee, J. S.; Choi, K. H.; Ghim, H. D.; Kim, S. S.; Chun, D. H.; Kim, H. Y.; Lyoo, W. S., *J. Appl. Polym. Sci.* **2004**, *93* (4), 1638-1646.
- [123] Yuan, X.; Zhang, Y.; Dong, C.; Sheng, J., *Polym. Int.* **2004**, *53* (11), 1704-1710.
- [124] Rutledge, G. C.; Li, Y.; Fridrikh, S.; Warner, S.; Kalayci, V.; Patra, P., *Annual Report (M98-D01)* **2001**, 1-10.
- [125] Li, Z.; Wang, C., *Effects of Working Parameters on Electrospinning*. In *One-Dimensional nanostructures*, Springer: 2013; pp 15-28.
- [126] Kakade, M. V.; Givens, S.; Gardner, K.; Lee, K. H.; Chase, D. B.; Rabolt, J. F., *J. Am. Chem. Soc.* **2007**, *129* (10), 2777-2782.
- [127] Fennessey, S. F.; Farris, R. J., *Polymer* **2004**, *45* (12), 4217-4225.
- [128] Xu, C.; Inai, R.; Kotaki, M.; Ramakrishna, S., *Biomaterials* **2004**, *25* (5), 877-886.
- [129] Zhou, Z.; Liu, K.; Lai, C.; Zhang, L.; Li, J.; Hou, H.; Reneker, D. H.; Fong, H., *Polymer* **2010**, *51* (11), 2360-2367.
- [130] Teo, W. E.; Ramakrishna, S., *Nanotechnology* **2006**, *17* (14), R89.
- [131] Li, D.; Wang, Y.; Xia, Y., *Nano Lett.* **2003**, *3* (8), 1167-1171.
- [132] Yan, H.; Liu, L.; Zhang, Z., *Appl. Phys. Lett.* **2009**, *95* (14), 143114.
- [133] Katta, P.; Alessandro, M.; Ramsier, R. D.; Chase, G. G., *Nano Lett.* **2004**, *4* (11), 2215-2218.
- [134] Teo, W.; Kotaki, M.; Mo, X.; Ramakrishna, S., *Nanotechnology* **2005**, *16* (6), 918.
- [135] Tan, E.; Lim, C., *Compos. Sci. Technol.* **2006**, *66* (9), 1102-1111.
- [136] Tan, E. P. S.; Goh, C. N.; Sow, C. H.; Lim, C. T., *Appl. Phys. Lett.* **2005**, *86* (7).
- [137] Tan, E. P. S.; Ng, S. Y.; Lim, C. T., *Biomaterials* **2005**, *26* (13), 1453-1456.
- [138] Chen, Z.; Wei, B.; Mo, X.; Lim, C.; Ramakrishna, S.; Cui, F., *Mater. Sci. Eng., C* **2009**, *29* (8), 2428-2435.
- [139] Hang, F.; Lu, D.; Barber, A. H. In *Combined AFM-SEM for mechanical testing of fibrous biological materials*, MRS Proceedings, Cambridge Univ Press: 2009; pp 1187-KK06-06.
- [140] Yu, M.-F.; Lourie, O.; Dyer, M. J.; Moloni, K.; Kelly, T. F.; Ruoff, R. S., *Science* **2000**, *287* (5453), 637-640.

- [141] Hang, F.; Lu, D.; Bailey, R. J.; Jimenez-Palomar, I.; Stachewicz, U.; Cortes-Ballesteros, B.; Davies, M.; Zech, M.; Bödefeld, C.; Barber, A. H., *Nanotechnology* **2011**, 22 (36), 365708.
- [142] Zussman, E.; Burman, M.; Yarin, A.; Khalfin, R.; Cohen, Y., *J. Polym. Sci., Part B: Polym. Phys.* **2006**, 44 (10), 1482-1489.
- [143] Liu, L. Q.; Tasis, D.; Prato, M.; Wagner, H. D., *Adv. Mater.* **2007**, 19 (9), 1228-1233.
- [144] Hang, F.; Barber, A. H., *Journal of the Royal Society Interface* **2011**, 8 (57), 500-505.
- [145] Wong, E. W.; Sheehan, P. E.; Lieber, C. M., *Science* **1997**, 277 (5334), 1971-1975.
- [146] Almecija, D.; Blond, D.; Sader, J. E.; Coleman, J. N.; Boland, J. J., *Carbon* **2009**, 47 (9), 2253-2258.
- [147] Babu, J. S. S.; Kang, C. G., *Mater. Des.* **2010**, 31 (10), 4881-4885.
- [148] Tranchida, D.; Piccarolo, S.; Soliman, M., *Macromolecules* **2006**, 39 (13), 4547-4556.
- [149] Bhushan, B.; Koinkar, V. N., *Appl. Phys. Lett.* **1994**, 64 (13), 1653-1655.
- [150] Hertz, H., *J. Reine. Angew. Math.* **1881**, 92, 156-171.
- [151] Ko, F.; Gogotsi, Y.; Ali, A.; Naguib, N.; Ye, H.; Yang, G.; Li, C.; Willis, P., *Adv. Mater.* **2003**, 15 (14), 1161-1165.
- [152] Tan, E. P. S.; Lim, C. T., *Compos. Sci. Technol.* **2006**, 66 (9), 1102-1111.
- [153] Chen, X.; Xu, Z.-H.; Li, X.; Shaibat, M. A.; Ishii, Y.; Ruoff, R. S., *Carbon* **2007**, 45 (2), 416-423.
- [154] Ahn, B. W.; Kang, T. J., *J. Appl. Polym. Sci.* **2012**, 125 (2), 1567-1575.
- [155] Wang, M.; Jin, H.-J.; Kaplan, D. L.; Rutledge, G. C., *Macromolecules* **2004**, 37 (18), 6856-6864.
- [156] Feng, G.; Nix, W. D.; Yoon, Y.; Lee, C. J., *J. Appl. Phys.* **2006**, 99 (7), 074304.
- [157] Yuya, P. A.; Wen, Y.; Turner, J. A.; Dzenis, Y. A.; Li, Z., *Appl. Phys. Lett.* **2007**, 90 (11), 111909.
- [158] Treacy, M.; Ebbesen, T.; Gibson, J., *Nature* **1996**, 381, 678 - 680.
- [159] Luo, S.; Van Ooij, W. J., *J. Adhes. Sci. Technol.* **2002**, 16 (13), 1715-1735.
- [160] Dang, Z.-M.; Wang, H.-Y.; Xu, H.-P., *Appl. Phys. Lett.* **2006**, 89 (11), 112902.
- [161] Wang, M.; Bonfield, W., *Biomaterials* **2001**, 22 (11), 1311-1320.
- [162] Demjén, Z.; Pukánszky, B.; Nagy, J., *Composites Part A: Applied Science and Manufacturing* **1998**, 29 (3), 323-329.

- [163] Monte, S. J.; Sugerman, G., *Polymer Engineering & Science* **1984**, 24 (18), 1369-1382.
- [164] Maiti, S. N.; Sharma, K. K., *J. Mater. Sci.* **1992**, 27 (17), 4605-4613.
- [165] Tjong, S.; Meng, Y., *J. Appl. Polym. Sci.* **1998**, 70 (3), 431-439.
- [166] Khaled, S.; Sui, R.; Charpentier, P. A.; Rizkalla, A. S., *Langmuir* **2007**, 23 (7), 3988-3995.
- [167] Sonoda, K.; Juuti, J.; Moriya, Y.; Jantunen, H., *Compos. Struct.* **2010**, 92 (5), 1052-1058.
- [168] Griffete, N.; Herbst, F.; Pinson, J.; Ammar, S.; Mangeney, C., *J. Am. Chem. Soc.* **2011**, 133 (6), 1646-1649.
- [169] Kamal, M.; Sharma, C. S.; Upadhyaya, P.; Verma, V.; Pandey, K. N.; Kumar, V.; Agrawal, D. D., *J. Appl. Polym. Sci.* **2012**, 124 (4), 2649-2656.
- [170] Pope, E.; Asami, M.; Mackenzie, J., *J. Mater. Res.* **1989**, 4 (04), 1018-1026.
- [171] Abboud, M.; Turner, M.; Duguet, E.; Fontanille, M., *J. Mater. Chem.* **1997**, 7 (8), 1527-1532.
- [172] Guo, Z.; Liang, X.; Pereira, T.; Scaffaro, R.; Thomas Hahn, H., *Compos. Sci. Technol.* **2007**, 67 (10), 2036-2044.
- [173] Zhao, S.; Zhang, J.; Zhao, S.; Li, W.; Li, H., *Compos. Sci. Technol.* **2003**, 63 (7), 1009-1014.
- [174] Szabó, J. S.; Karger-Kocsis, J.; Gryshchuk, O.; Czigány, T., *Compos. Sci. Technol.* **2004**, 64 (10–11), 1717-1723.
- [175] Shang, X.-y.; Zhu, Z.-k.; Yin, J.; Ma, X.-d., *Chem. Mater.* **2002**, 14 (1), 71-77.
- [176] Yeh, J. M.; Weng, C. J.; Huang, K. Y.; Huang, H. Y.; Yu, Y. H.; Yin, C. H., *J. Appl. Polym. Sci.* **2004**, 94 (1), 400-405.
- [177] Tripathi, G.; Basu, B., *J. Appl. Polym. Sci.* **2012**, 124 (3), 2133-2143.
- [178] Tripathi, G.; Dubey, A. K.; Basu, B., *J. Appl. Polym. Sci.* **2012**, 124 (4), 3051-3063.
- [179] Li, R.; Ye, L.; Mai, Y.-W., *Composites Part A: Applied Science and Manufacturing* **1997**, 28 (1), 73-86.
- [180] Yuan, X.; Jayaraman, K.; Bhattacharyya, D., *Composites Part A: Applied Science and Manufacturing* **2004**, 35 (12), 1363-1374.
- [181] Liu, D.; Chen, P.; Mu, J.; Yu, Q.; Lu, C., *Appl. Surf. Sci.* **2011**, 257 (15), 6935-6940.
- [182] Selcuk, M.; Oksuz, L.; Basaran, P., *Bioresour. Technol.* **2008**, 99 (11), 5104-5109.

- [183] Cioffi, M.; Voorwald, H.; Hein, L.; Ambrosio, L., *Composites Part A: Applied Science and Manufacturing* **2005**, *36* (5), 615-623.
- [184] Derand, T.; Molin, M.; Kvam, K., *Dent. Mater.* **2005**, *21* (12), 1158-1162.
- [185] Breton, Y.; Delpeux, S.; Benoit, R.; Salvetat, J.; Sinturel, C.; Beguin, F.; Bonnamy, S.; Desarmot, G.; Boufendi, L., *Molecular Crystals and Liquid Crystals* **2002**, *387* (1), 135-140.
- [186] Zhang, S.; Minus, M. L.; Zhu, L.; Wong, C.-P.; Kumar, S., *Polymer* **2008**, *49* (5), 1356-1364.
- [187] Wang, C.; Hwang, L., *J. Polym. Sci., Polym. Phys.* **1996**, *34* (8), 1435-1442.
- [188] Peron, B.; Lowe, A.; Baillie, C., *Compos. Part A: Appl. Sci. Manuf.* **1996**, *27* (9), 839-845.
- [189] Wagner, H. D.; Lustiger, A.; Marzinsky, C. N.; Mueller, R. R., *Compos. Sci. Technol.* **1993**, *48* (1), 181-184.
- [190] Thomason, J.; Van Rooyen, A., *J. Mater. Sci.* **1992**, *27* (4), 897-907.
- [191] Gao, Y.; Ren, K.; Ning, N.; Fu, Q.; Wang, K.; Zhang, Q., *Polymer* **2012**, *53* (13), 2792-2801.
- [192] Chatterjee, A.; Price, F.; Newman, S., *J. Polym. Sci., Part B: Polym. Phys.* **1975**, *13* (12), 2369-2383.
- [193] Wood, J.; Wagner, H.; Marom, G., *J. Mater. Sci. letters* **1995**, *14* (22), 1613-1615.
- [194] Wu, C.-M.; Chen, M.; Karger-Kocsis, J., *Polym. Bull.* **1998**, *41* (2), 239-245.
- [195] Wood, J. R.; Marom, G., *Appl. Compos. Mater.* **1997**, *4* (4), 197-207.
- [196] Zafeiropoulos, N.; Baillie, C.; Matthews, F., *Composites Part A: Applied Science and Manufacturing* **2001**, *32* (3), 525-543.
- [197] Sundararajan, P.; Singh, S.; Moniruzzaman, M., *Macromolecules* **2004**, *37* (26), 10208-10211.
- [198] Alizadeh, A.; Sohn, S.; Quinn, J.; Marand, H.; Shank, L. C.; Iler, H. D., *Macromolecules* **2001**, *34* (12), 4066-4078.
- [199] Sohn, S.; Alizadeh, A.; Marand, H., *Polymer* **2000**, *41* (25), 8879-8886.
- [200] Takahashi, T.; Yonetake, K.; Koyama, K.; Kikuchi, T., *Macromol. Rapid Commun.* **2003**, *24* (13), 763-767.
- [201] Brady, R. L.; Porter, R. S., *J. Appl. Polym. Sci.* **1990**, *39* (9), 1873-1885.
- [202] Pötschke, P.; Fornes, T.; Paul, D., *Polymer* **2002**, *43* (11), 3247-3255.
- [203] Cheng, F.; Kardos, J.; Tolbert, T., *SPE Journal* **1970**, *26*, 62-64.

- [204] Conix, A.; Jeurissen, L., Plasticization of Bisphenol A Polycarbonate. In *Plasticization and Plasticizer Processes*, American Chemical Society: 1965; Vol. 48, pp 172-184.
- [205] Legras, R.; Mercier, J.; Nield, E., *Nature* **1983**, (304), 432 - 434.
- [206] Privalko, V. P.; Sukhorukov, D. I.; Karger-kocsis, J.; Calleja, F. J. B., *J. Macromol. Sci. Phy.* **2006**, 38 (1-2), 27-35.
- [207] Kobayashi, T.; Broutman, L. J., *Polym. Eng. Sci.* **1974**, 14 (4), 260-263.
- [208] Harron, H., *Int. J. Electron.* **1996**, 81 (4), 485-489.
- [209] Dulmage, W.; Contois, L., *J. Polym. Sci.* **1958**, 28 (117), 275-284.
- [210] Robertson, R. E.; Buenker, R. J., *Journal of Polymer Science Part A: General Papers* **1964**, 2 (11), 4889-4901.
- [211] Ward, I.; Pinnock, P., *British Journal of Applied Physics* **1966**, 17 (1), 3.
- [212] Chung, D. D., *Composite materials: science and applications*. Springer Science & Business Media: 2010.
- [213] Qian, D.; Dickey, E. C.; Andrews, R.; Rantell, T., *Appl. Phys. Lett.* **2000**, 76 (20), 2868-2870.
- [214] Bogner, A.; Jouneau, P.-H.; Thollet, G.; Basset, D.; Gauthier, C., *Micron* **2007**, 38 (4), 390-401.
- [215] Goldstein, J.; Newbury, D. E.; Echlin, P.; Joy, D. C.; Romig Jr, A. D.; Lyman, C. E.; Fiori, C.; Lifshin, E., *Scanning electron microscopy and X-ray microanalysis: a text for biologists, materials scientists, and geologists*. Springer Science & Business Media: 2012.
- [216] Shi, X.; Nguyen, T. A.; Suo, Z.; Liu, Y.; Avci, R., *Surf. Coat. Technol.* **2009**, 204 (3), 237-245.
- [217] Heo, Y.; Varadarajan, V.; Kaufman, M.; Kim, K.; Norton, D.; Ren, F.; Fleming, P., *Appl. Phys. Lett.* **2002**, 81 (16), 3046-3048.
- [218] Echlin, P.; Fiori, C.; Goldstein, J.; Joy, D. C.; Newbury, D. E., *Advanced scanning electron microscopy and X-ray microanalysis*. Springer Science & Business Media: 2013.
- [219] De Graef, M., *Introduction to conventional transmission electron microscopy*. Cambridge University Press: 2003.
- [220] Williams, D. B.; Carter, C. B., *The transmission electron microscope*. In *Transmission electron microscopy*, Springer: 1996; pp 3-17.
- [221] Schawe, J., *Thermochim. Acta* **1995**, 261, 183-194.
- [222] Stuart, B., *Infrared spectroscopy*. Wiley Online Library: 2005.

- [223] Kelly, A. A.; Knowles, K. M., *Crystallography and crystal defects*. John Wiley & Sons: 2012.
- [224] Fultz, B.; Howe, J. M., *Transmission electron microscopy and diffractometry of materials*. Springer Science & Business Media: 2012.
- [225] Davisson, C.; Germer, L. H., *Phys. Rev.* **1927**, *30* (6), 705.
- [226] Pérez - Rigueiro, J.; Viney, C.; Llorca, J.; Elices, M., *J. Appl. Polym. Sci.* **1998**, *70* (12), 2439-2447.
- [227] Pai, C.-L. *Morphology and mechanical properties of electrospun polymeric fibers and their nonwoven fabrics*. Massachusetts Institute of Technology, 2011.
- [228] Butt, H. J.; Jaschke, M., *Nanotechnology* **1995**, *6* (1), 1.
- [229] Monclus, M.; Young, T.; Di Maio, D., *J. Mater. Sci.* **2010**, *45* (12), 3190-3197.
- [230] Domke, J.; Radmacher, M., *Langmuir* **1998**, *14* (12), 3320-3325.
- [231] Hertz, H., *J. reine angew. Math.* **1882**, *92*, 156-171.
- [232] Kovarik, L.; Bowden, M.; Genc, A.; Szanyi, J.; Peden, C. H. F.; Kwak, J. H., *J. Phys. Chem. C* **2014**, *118* (31), 18051-18058.
- [233] Gu, S.; Ren, J.; Vancso, G., *Eur. Polym. J.* **2005**, *41* (11), 2559-2568.
- [234] Wang, T.; Kumar, S., *J. Appl. Polym. Sci.* **2006**, *102* (2), 1023-1029.
- [235] Li, W. J.; Shi, E. W.; Yin, Z. W., *J. Cryst. Growth* **2000**, *208* (1), 546-554.
- [236] Kitayama, M.; Glaeser, A. M., *J. Am. Ceram. Soc.* **2005**, *88* (12), 3492-3500.
- [237] German, R. M.; Munir, Z. A., *J. Am. Ceram. Soc.* **1976**, *59* (9-10), 379-383.
- [238] Gibbs, J. W., *American Journal of Science* **1878**, (96), 441-458.
- [239] Bowen, P.; Carry, C., *Powder Technol.* **2002**, *128* (2), 248-255.
- [240] Adamson, A. W.; Gast, A. P., **1967**.
- [241] Sears, G. W.; DeVries, R. C., *The Journal of Chemical Physics* **1963**, *39* (11), 2837.
- [242] Ramaseshan, R.; Sundarrajan, S.; Jose, R.; Ramakrishna, S., *J. Appl. Phys.* **2007**, *102* (11), 111101.
- [243] Shackelford, J. F.; Alexander, W., *CRC materials science and engineering handbook*. CRC press: 2010.
- [244] Vahtrus, M.; Umalas, M.; Polyakov, B.; Dorogin, L.; Saar, R.; Tamme, M.; Saal, K.; Lõhmus, R.; Vlassov, S., *Mater. Charact.* **2015**, *107*, 119-124.
- [245] Demczyk, B. G.; Wang, Y. M.; Cumings, J.; Hetman, M.; Han, W.; Zettl, A.; Ritchie, R. O., *Mater. Sci. Eng. A* **2002**, *334* (1-2), 173-178.
- [246] Lee, W. E.; Rainforth, M., *Ceramic microstructures: property control by processing*. Springer: Netherlands, 1994.

- [247] Romine, J. C., *Ceram. Eng. and Sci. Proc.* **1987**, 8 (7-8), 755-765.
- [248] Hartman, D.; Greenwood, M. E.; Miller, D. M., High strength glass fibers. Society for the Advancement of Material and Process Engineering: California, USA, 1994; Vol. 39, p 521-533.
- [249] Vautard, F.; Ozcan, S.; Poland, L.; Nardin, M.; Meyer, H., *Compos. Part A: Appl. Sci. Manuf.* **2013**, 45, 162-172.
- [250] Flores, O.; Bordia, R. K.; Nestler, D.; Krenkel, W.; Motz, G., *Adv. Eng. Mater* **2014**, 16 (6), 621-636.
- [251] Bakis, C. E.; Bank, L. C.; Brown, V.; Cosenza, E.; Davalos, J.; Lesko, J.; Machida, A.; Rizkalla, S.; Triantafillou, T., *Journal of composites for construction* **2002**, 6 (2), 73-87.
- [252] Coleman, J. N.; Khan, U.; Blau, W. J.; Gun'ko, Y. K., *Carbon* **2006**, 44 (9), 1624-1652.
- [253] Halpin, J. C., Primer on Composite Materials Analysis, (Revised). CRC Press: 1992.
- [254] Eshelby, J. D. In The determination of the elastic field of an ellipsoidal inclusion, and related problems, Proceedings of the Royal Society of London A: Mathematical, Physical and Engineering Sciences, The Royal Society: 1957; pp 376-396.
- [255] Cox, H., *British journal of applied physics* **1952**, 3 (3), 72.
- [256] Taya, M.; Arsenault, R., *Scripta Metallurgica* **1987**, 21 (3), 349-354.
- [257] Mori, T.; Tanaka, K., *Acta Metall.* **1973**, 21 (5), 571-574.
- [258] Tandon, G.; Weng, G., *Polym. Compos.* **1984**, 5 (4), 327-333.
- [259] Hashin, Z.; Shtrikman, S., *Journal of the Mechanics and Physics of Solids* **1962**, 10 (4), 335-342.
- [260] Hashin, Z.; Shtrikman, S., *Journal of the Mechanics and Physics of Solids* **1963**, 11 (2), 127-140.
- [261] Chou, T.-W.; Nomura, S.; Taya, M., *J. Compos. Mater.* **1980**, 14 (3), 178-188.
- [262] Laws, N.; McLaughlin, R., *Journal of the Mechanics and Physics of Solids* **1979**, 27 (1), 1-13.
- [263] Tucker III, C. L.; Liang, E., *Compos. Sci. Technol.* **1999**, 59 (5), 655-671.
- [264] Kalaprasad, G.; Joseph, K.; Thomas, S., *J. Compos. Mater.* **1997**, 31 (5), 509-527.
- [265] Kim, J. A.; Seong, D. G.; Kang, T. J.; Youn, J. R., *Carbon* **2006**, 44 (10), 1898-1905.
- [266] Brahmakumar, M.; Pavithran, C.; Pillai, R., *Compos. Sci. Technol.* **2005**, 65 (3), 563-569.

- [267] Hughes, J., *Compos. Sci. Technol.* **1991**, *41* (1), 13-45.
- [268] Blatz, M. B.; Sadan, A.; Kern, M., *The Journal of prosthetic dentistry* **2003**, *89* (3), 268-274.
- [269] Kim, J.-K.; Mai, Y.-W., *Engineered interfaces in fiber reinforced composites*. Elsevier: 1998.
- [270] Posthumus, W.; Magusin, P. C. M. M.; Brokken-Zijp, J. C. M.; Tinnemans, A. H. A.; van der Linde, R., *J. Colloid Interface Sci.* **2004**, *269* (1), 109-116.
- [271] Guo, Z.; Pereira, T.; Choi, O.; Wang, Y.; Hahn, H. T., *J. Mater. Chem.* **2006**, *16* (27), 2800.
- [272] Chau, J. L. H.; Hsu, S. L.-C.; Chen, Y.-M.; Yang, C.-C.; Hsu, P. C., *Adv. Powder Technol.* **2010**, *21* (3), 341-343.
- [273] Arsalani, N.; Fattahi, H.; Nazarpour, M., *Express Polym Lett* **2010**, *4* (6), 329-38.
- [274] Paunikallio, T.; Suvanto, M.; Pakkanen, T., *React. Funct. Polym.* **2008**, *68* (3), 797-808.
- [275] Nie, M.; Kalyon, D. M.; Fisher, F. T., *ACS applied materials & interfaces* **2014**, *6* (17), 14886-14893.
- [276] Halpin, J., *J. Compos. Mater.* **1969**, *3* (4), 732-734.
- [277] Affdl, J.; Kardos, J., *Polymer Engineering & Science* **1976**, *16* (5), 344-352.
- [278] Davis, W.; Macosko, C., *J. Rheol.* **1978**, *22* (1), 53-71.
- [279] G'sell, C., *Strength of metals and alloys* **1986**, 1943-1982.
- [280] Ishida, H.; Bussi, P., *Macromolecules* **1991**, *24* (12), 3569-3577.
- [281] Feldman, A. Y.; Gonzalez, M. F.; Wachtel, E.; Moret, M. P.; Marom, G., *Polymer* **2004**, *45* (21), 7239-7245.
- [282] Gassan, J.; Mildner, I.; Bledzki, A. K., *Compos. Interfaces* **2001**, *8* (6), 443-452.
- [283] Hsiao, B. S.; Eric, J. In *Study of transcrystallization in polymer composites*, MRS Proceedings, Cambridge Univ Press: 1989; p 117.
- [284] Wunderlich, B., *Macromolecular physics*. Elsevier: 2012; Vol. 2.
- [285] Hata, T.; Ohsaka, K.; Yamada, T.; Nakamae, K.; Shibata, N.; Matsumoto, T., *J. Adhes.* **1994**, *45* (1-4), 125-135.
- [286] Starkweather, H. W.; Moore, G. E.; Hansen, J. E.; Roder, T. M.; Brooks, R. E., *J. Polym. Sci.* **1956**, *21* (98), 189-204.
- [287] Nielsen, L. E.; Stockton, F. D., *J. Polym. Sci. A Polym. Chem.* **1963**, *1* (6), 1995-2002.
- [288] Doyle, M. J., *Polym. Eng. Sci.* **2000**, *40* (2), 330-335.



- [289] Fischer-Cripps, A. C., *Factors Affecting Nanoindentation Test Data*. Springer: 2000.
- [290] Sneddon, I. N., *Int. J. Eng. Sci.* **1965**, 3 (1), 47-57.
- [291] Schnell, H., *Chemistry and physics of polycarbonates*. Interscience Publishers: New York, 1964; p 225.
- [292] Gallez, F.; Legras, R.; Mercier, J., *Polym. Eng. Sci.* **1976**, 16 (4), 276-283.
- [293] Marand, H.; Alizadeh, A.; Farmer, R.; Desai, R.; Velikov, V., *Macromolecules* **2000**, 33 (9), 3392-3403.
- [294] Mercier, J.; Legras, R., *J. Polym. Sci., Polym. Lett.* **1970**, 8 (9), 645-650.
- [295] Li, J.; Cheung, W., *Polymer* **1999**, 40 (8), 2085-2088.
- [296] Gao, H.; Ji, B.; Jäger, I. L.; Arzt, E.; Fratzl, P., *Proceedings of the National Academy of Sciences* **2003**, 100 (10), 5597-5600.